Electrochemical Redox-Cycling Devices

Von der Fakultät für Mathematik, Informatik und Naturwissenschaften der RWTH Aachen University zur Erlangung des akademischen Grades eines Doktors der Naturwissenschaften genehmigte Dissertation

vorgelegt von
Diplom-Physiker
Friedrich Enno Kätelhön
aus
Essen

Berichter:
Universitätsprofessor Jun.-Prof. Dr. Bernhard Wolfrum
Universitätsprofessor Prof. Dr. Jörg Fitter

Tag der mündlichen Prüfung: 9. Mai 2014

Abstract

Nanoelectrochemistry is a fascinating research discipline at the interface between nanotechnology and electrochemistry. Alongside proceeding technological advances in micro- and nanofabrication, the miniaturization of classic electrochemical setups was enabled during the last two decades. By this means, new effects were observed, which allowed the development of novel concepts for nanoelectrochemical sensors.

The presented work investigates the comparably young concept of nanofluidic redox-cycling sensors in regard to their fabrication, application, and theoretical description. These sensors have been first introduced by the group of Serge Lemay in 2007 and usually comprise two parallel electrodes that are incorporated underneath and above a nanofluidic channel, while electrodes can be biased individually. Redox-active molecules can then participate in fast, repeated reactions at the electrodes. By this means, a current is formed across the gap, which is significantly amplified in comparison to conventional electrochemical sensors. Therefore, the sensitivity of such devices often exceeds the sensitivity of classic sensors by orders of magnitude and even enables sensing at molecular resolution.

Both presented devices are highly-integrated on-chip sensors for the spatiotemporal detection of redox-active molecules. The first chip features an array of nanofluidic sensors, while individual sensors can be operated in parallel. The chip is characterized in detail and is used for the spatiotemporal detection of concentration gradients inside a microfluidic system. The second chip is developed particularly for high spatial resolutions and can be employed for electrochemical imaging. By utilizing a crossbar-architecture, the degree of integration is drastically increased and the overall number of sensors on the chip as well as the sensor density is significantly improved.

The small size and the high sensitivity of nanofluidic sensors further lead to a variety of mesoscopic effects that can partly be observed in the sensor's current noise. In order to investigate these effects, a comprehensive simulation framework for the modeling of the sensor's noise is described, which already was employed in various studies. The model is based on the description of the redox-active molecules' Brownian movement through random walks, which allows simulations of noise phenomena that cannot be modeled by finite elements approaches. By this means, experimental data can be closely reproduced and predicted. Based on these results, new sensor concepts are suggested for the detection of biological macromolecules in nano- and micro pores and for the measurement of the average adsorption times of redox-active molecules in common electrochemical measurement setups.

Kurzfassung

Nanoelektrochemie ist faszinierendes Forschungsfeld im Grenzbereich zwischen Nanotechnologie und Elektrochemie. Mit den fortschreitenden technischen Möglichkeiten im Bereich der Mikro- und Nanofabrikation konnten in den letzten zwei Jahrzehnten viele klassische elektrochemische Messaufbauten deutlich miniaturisiert werden. So wurden völlig neue Effekte sichtbar, auf deren Basis Konzepte für nanoelektrochemische Sensoren entwickelt werden konnten.

Die vorliegende Arbeit untersucht hierbei das noch relativ junge Konzept nanofluidischer redox-cycling Sensoren hinsichtlich ihrer Fabrikation, Anwendung und theoretischen Beschreibung. Diese Sensoren, die erstmalig 2007 durch die Gruppe von Serge Lemay vorgestellt wurden, bestehen meist aus zwei parallelen Elektroden, die sich innerhalb eines nanofluidischen Kanals dicht gegenüberliegen und deren Potentiale individuell eingestellt werden können. Redox-aktive Moleküle können dann an schnellen, wiederholten Reaktionen mit den Elektroden teilnehmen und so einen Strom über den Kanal erzeugen. Im Vergleich zu konventionellen elektrochemischen Sensoren ist dieser Strom deutlich verstärkt, wodurch die Sensitivität solcher Sensoren oft um Größenordnungen höher liegt und sogar die Detektion mit molekularer Auflösung ermöglicht.

Die zwei hier vorgestellten Aufbauten sind hochintegrierte on-chip Lösungen für die zeit- und ortsaufgelöste Detektion von redox-aktiven Molekülen. Auf dem ersten Chip befindet sich ein enges Gitter aus nanofluidischen Sensoren, die parallel ausgelesen werden können. Der Chip wird detailliert charakterisiert für die zeit- und ortsaufgelöste Detektion von Molekülen in einem mikrofluidischen System verwendet. Der zweite Chip ist speziell für hohe Ortsauflösungen konzipiert worden und kann zur elektrochemischen Bildgebung genutzt werden. Unter Verwendung einer Crossbar-Struktur kann weiter der Grad der Integration drastisch verbessert und sowohl die Anzahl der einzelnen Sensoren pro Chip als auch die Dichte der Sensoren deutlich erhöht werden.

Die geringe Größe und die hohe Sensitivität nanofluidischer Sensoren führen zu einer Vielzahl mesoskopischer Prozesse, die sich zu einem großen Teil im Stromrauschen der Sensoren widerspiegeln. Um diese Effekte zu untersuchen, wird hier eine umfangreiche Softwareumgebung zur Modellierung von Rauschphänomenen beschrieben, die bereits in verschiedenen Studien Anwendung finden konnte. Das Model basiert auf der Darstellung der Brownschen Bewegung aller redox-aktiven Moleküle eines Systems durch Random-Walks und kann im Gegensatz zu Finite-Elemente Simulationen so das Rauschverhalten der Sensoren simulieren. Experimentelle Daten können gut reproduziert und vorhergesagt werden. Auf Basis dieser Ergebnisse werden zwei neue Sensorkonzepte vorgeschlagen, eines zur Detektion von biologischen Makromolekülen in Nano- und Mikroporen und eines zur direkten Messung der mittleren Adsorptionsdauer von redox-aktiven Molekülen mit Hilfe gängiger elektrochemicher Messaufbauten.

Contents

Chapter 1

Introduction

The discipline of nanoelectrochemistry is a fascinating field of research. Driven by questions of fundamental research as well as by upcoming applications, a growing international community has brought forward nanoelectrochemistry since the late eighties. Due to rapid scientific and technological progress that was enabled by parallel advances in micro-fabrication and -actuation, nano-electrochemical approaches are today used in a variety of different applications including sensors, energy storages, fuel cells and many others.

The term nanoelectrochemistry, which can be understood as a fusion of the terms nanotechnology and electrochemistry, already underlines the inter-disciplinary nature of this discipline. In the context of today's major fields of research, it can be best classified as the interface between nanotechnology and electrochemistry. By common definitions, nanotechnology refers to the science of structures that feature sizes below few hundreds of nanometers. While it is not limited to certain types of effects that are for instance electrical, chemical, or biological, it rather focuses on all novel properties that arise with proceeding miniaturization. Even though the term itself was coined later, this definition is based on Richard Feynman's visionary speech "There's plenty of room on the bottom" in 1959 [1], in which he suggests a variety of applications for nanotechnology and which is often noticed to be the foundation of nanotechnology. Indeed, many of his visions became reality today and, unlike many other fields of research, nanotechnology had an enormous impact on today's life: the rise of the internet, computers, and mobile communication devices significantly changed daily life all over the world. Electrochemistry, on the other hand, has a long history dating back to Luigi Galvani and Alessandro Volta and originated many

technologies that are well established today. Applications include batteries, fuel cells and sensors, while particularly batteries are ubiquitous nowadays. Generally speaking, it aims for a general description of all processes that link chemical reactions to electrical currents and has been an active field of research for more than two hundred years.

What benefits arise from the combination of nano-scaled structures and electrochemical methods? While diffusion hardly plays a role in our perception of the macroscopic world, it well does on the micro- and nano-scale. Since the average diffusive displacement of a particle is proportional to the square root of the time that passed since its release, diffusive movement on the nano-scale is rapid in comparison to other transport phenomena like convection. Hence, relative mass transport towards or inside a sensor can be significantly increased with increasing miniaturization. Furthermore, the small number of molecules that is involved in electrode processes at nanoelectrodes may lead to mesoscopic effects that allow new insights into molecular processes. These effects lead to a wide number of novel applications that cannot be implemented through methods of classical electrochemistry.

In my dissertation, I focus on the development and characterization of nanoelectrochemical sensors that resolve chemical concentration gradients at a high spatiotemporal resolution. I further investigate the fundamental working principles of nano-scaled redox-cycling sensors by means of computational and theoretical physics. Two new approaches to spectroscopic sensing are introduced and described in detail.

The upcoming chapters of this work are arranged as follows:

- **Chapter 2:** The second chapter provides an overview on the fundamental concepts of nanoelectrochemistry. It describes diffusive processes and electrochemical reactions at electrode-electrolyte interfaces on an introductory level.

- **Chapter 3:** The third chapter addresses the current state of research in on-chip implementations of nanoelectrochemical sensors. It provides a wide overview on different approaches and critically elucidates advantages and drawbacks of various methods.

- **Chapter 4:** The fourth chapter describes the development and characterization of a nanofluidic redox-cycling sensor that is solely fabricated

through methods of optical lithography. It is further characterized in-depth in a microfluidic environment.

- **Chapter 5:** The fifth chapter introduces a sensor that is optimized for electrochemical imaging at a significantly improved spatial resolution in regard to the previously described sensor. Its fabrication as well as different modes of operation are demonstrated.

- **Chapter 6:** The sixth chapter presents a simulation framework for the modeling of noise characteristics of nanoelectrochemical devices. Based on a random walk approach, design-dependent noise features are discussed in detail and new sensing concepts are suggested. The efficiency of the simulation concept is further verified by comparison to experimental data.

- **Chapter 7:** The last chapter describes an advanced version of the formerly introduced simulation framework. Based on an additionally implemented adsorption model, adsorption-dependent noise characteristics of electrochemical sensors are described. By this means, a novel approach for the determination of average adsorption- and desorption-times of individual molecules is developed. Upper limits for average adsorption times of ferrocene dimethanol molecules are found through a comparison between experimental and simulated data.

Chapter 2

Fundamentals of nanoelectrochemistry

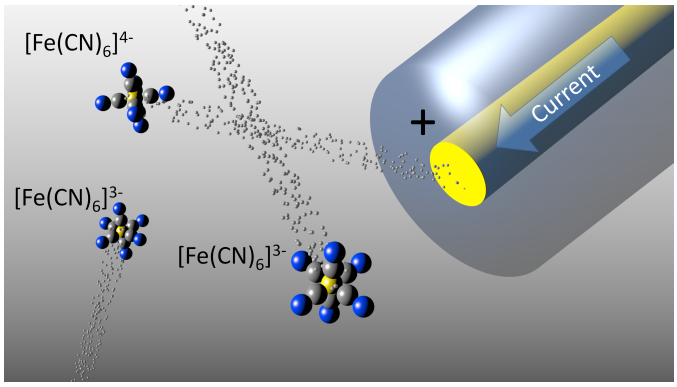

2.1 Preamble

The research field of nanoelectrochemistry focuses on new effects that may occur when electrochemical setups are miniaturized to the nano scale. Hence, it aims for elucidating the nature of chemical reactions involving electrical currents at nanoelectrodes or electrodes placed into a nano-scaled arrangement. Observed effects are then mostly governed by three factors that are discussed in the following: The thermal motion of analyte in an aqueous or gaseous fluid, the electrode electrolyte interface, and the nature of the electron transfer at the electrode.

2.2 Brownian movement and diffusion

While thermal motion can be observed as a relatively slow effect on the macro scale, it is increasingly important on smaller scales due to the non-linear relation between the average displacement of a molecule and the time since its release. For example, a molecule requires about a second to travel 5 mm along one dimension in air, while it requires about a day to travel 1 m [2]. Hence, thermal motion is one of the key influences in nano-scaled electrochemical sensors.

The thermal energy that is stored in a fluid at temperatures above zero Kelvin is distributed over all molecules within the fluid according to Boltzmann's equation [3]. During collisions with other molecules, molecules continuously change their direction, hence, performing a random movement that does not feature any distinguished direction. However, even though the average spatial displacement of a molecule over time remains zero, its mean square displacement increases with time. We now follow a derivation, which is adapted from [2]. The effect can be mathematically treated starting from Fick's equation, which describes the measurable net mass transport along a concentration gradient. It relates the flux $\vec{j}$ to the concentration c as follows:

$$\vec{j} = -D\vec{\nabla}c(x, y, z). \tag{2.1}$$

Hereby, D defines the diffusion constant, which represents a measure for speed of a molecule's Brownian movement and which is given in units of m^2/s. Since mass cannot be destroyed or generated in this system, this formula can now be combined with the continuity equation:

$$\frac{\partial c}{\partial t} = -div\vec{j}. \tag{2.2}$$

This provides the general form of the diffusion equation,

$$\frac{\partial c}{\partial t} = D\Delta c. \tag{2.3}$$

In the one-dimensional case, this equation can be solved through the following general solution,

$$c(t,x) = \frac{A}{\sqrt{4\pi Dt}} exp\left(-\frac{x^2}{4Dt}\right), \tag{2.4}$$

where *A* represents a constant. If one now calculates the root mean square displacement of the molecules as a function of time, one obtains:

$$dx^2 = 2Ddt \tag{2.5}$$

for the one-dimensional case. For the three-dimensional case, one can analogically calculate the root mean square displacement from the three-dimensional general solution of 2.3:

$$d\vec{x}^2 = 6Ddt. \tag{2.6}$$

2.3 Electrode-electrolyte interfaces

Electrode-electrolyte interfaces play a crucial role in electrochemistry. Their nature may determine the electric fields at the interface and impact the chemical reactions significantly. Since the electrodes are usually good conductors, excess charges are located on their surfaces while all electric fields inside the conductor cancel out [4]. Therefore, one can limit the analysis to processes inside the electrolyte. In the following, the most common three models for the electric field are introduced.

2.3.1 Helmholtz-double-layer model

Helmholtz approximated the electrolyte to be an ideal conductor. All excess charges are then located at the interface, thus forming a parallel-plate like capacitor featuring a plate-to-plate distance that equals half of the free ion's

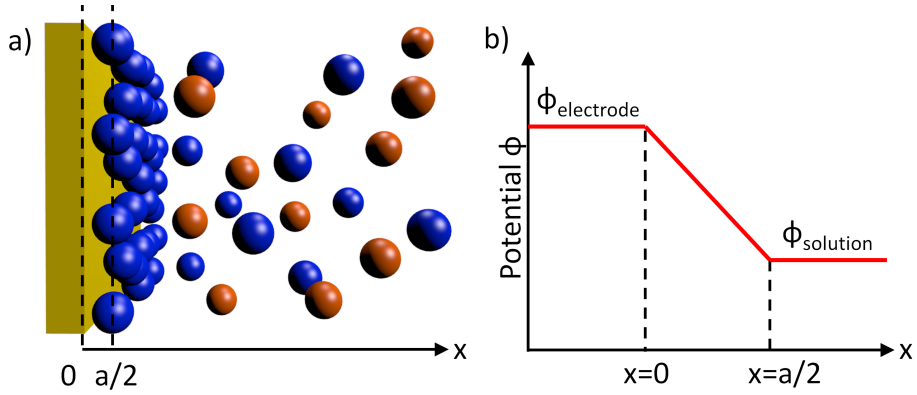

Figure 2.1: Helmholtz double layer: a) Schematic illustration of the interface. Differently colored spheres indicate positively and negatively charged ions. b) Schematic drawing of the potential at the interface.

radius *a*. Accordingly, the electric field is limited to the space in between the electrode at $x = 0$ and the ion's center $x = a/2$, and is given by

$$E = \frac{1}{\epsilon_0 \epsilon_r}\sigma = \frac{2\Delta\phi}{a} \tag{2.7}$$

With σ representing the surface charge of the electrode, $\epsilon_0\epsilon_r$ is the absolute permittivity of the electrolyte, and $U = \Delta\phi$ the applied voltage between the solution and the electrode. An illustration of the interface and a sketch of the resulting potential ϕ can be found in Figure 2.1. The interface capacity density C_h is then given by

$$C_h = \frac{\partial\sigma}{\partial U} = \frac{2\epsilon_0\epsilon_r}{a} \tag{2.8}$$

[4]. Even though values obtained through this formula often match the order of magnitude of experimentally observed values, it does not consider any influence of ion concentration, voltage, and thermal motion, which all can be found in real systems.

2.3.2 Gouy-Chapman model

In the early 20^{th} century, Gouy and Chapman independently developed a competing model based on statistical physics approach in France and England. They assumed the ions in solution to feature point-like dimensions and to represent a canonical ensemble of freely diffusing molecules in the electric field of the

biased electrode. This includes that the number of free ions in solution remains constant and no adsorption takes place at the electrode surface. The system further has a defined temperature and its volume remains constant. Hence, Maxwell-Boltzmann statistics can be applied to calculate the ions positions in solution and to derive the potential distribution nearby the electrode.

In the following, we will pursue an adaptation from Bard's derivation and explanation of the electrostatic potential profile inside the diffusive layer [4]. Accordingly, the diffusive layer can be subdivided into infinitesimally thin laminae that are arranged in parallel to the electrode surface. The concentration of the ion i inside the of each lamina can then be written as a function of the corresponding electrolyte potential ϕ measured with regard to the potential of the bulk solution,

$$c_i = c_i^0 exp\left(-\frac{z_i e_0 \phi}{k_B T}\right), \tag{2.9}$$

where c_i^0 represents the bulk concentration of the ion *i*, z_i the ions signed charge in the number of elementary charges e_0, k_B the Boltzmann constant, and T the absolte Temperature. The overall charge density ρ is then given by

$$\rho = \sum_i c_i^0 z_i e_0 exp\left(-\frac{z_i e_0 \phi}{k_B T}\right), \tag{2.10}$$

with *i* including all ion species that are present in solution. This result can now be combined with Poission's equation

$$\frac{d^2\phi}{dx^2} = -\frac{\rho}{\epsilon}. \tag{2.11}$$

Then, we obtain the Poission-Boltzmann equation:

$$\frac{d^2\phi}{dx^2} = -\frac{e_0}{\epsilon}\sum_i c_i^0 z_i exp\left(-\frac{z_i e_0 \phi}{k_B T}\right). \tag{2.12}$$

This equation can be solved for the simple case of two contrarily charged ions. The potential profile of the diffusive layer as a function of the electrode potential ϕ_0 is then given by the following equation

$$\frac{tanh\frac{ze_0\phi}{4k_bT}}{tanh\frac{ze_0\phi_0}{4k_bT}} = e^{-\kappa x}, \tag{2.13}$$

where

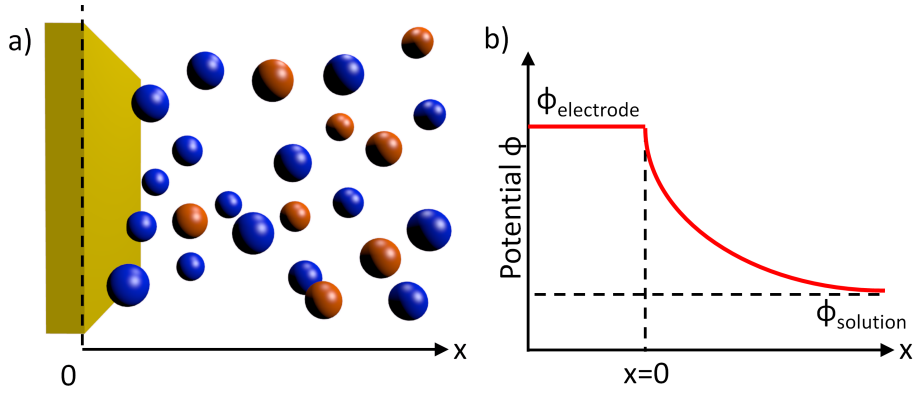

Figure 2.2: Gouy-Chapman layer: a) Schematic illustration of the interface. Differently colored spheres indicate positively and negatively charged ions. The concentration of the negatively charged (blue) molecules decreases with while concentration of the positively charged red molecules increases. In the bulk solution both concentrations are equal. b) Schematic drawing of the exponential potential profile at the interface.

$$\kappa = \sqrt{\frac{2c^0 z^2 e_0^2}{\epsilon k_B T}}. \tag{2.14}$$

For $\phi << k_B T$ one can use the approximation $tanh(x) = x$. Then equation 2.13 simplifies to a simple exponential decay

$$\phi = \phi_0 e^{-\kappa x}, \tag{2.15}$$

which represents a good approximation for $\phi_0 \leq 50/z$ mV at room temperature [4]. A schematic illustration of the potential can be found in Figure 2.2. The capacitance C_{gc} of the interface can now be calculated to

$$C_{gc} = \sqrt{\frac{2z^2 e_0^2 \epsilon c^0}{k_B T}} cosh\left(\frac{z e_0 \phi_0}{k_B T}\right). \tag{2.16}$$

This equation matches values that can be found in real systems at low concentrations and at low over overpotentials. However, there are two central drawbacks of this theory. First, capacitance values obtained are often two high and, second, the calculated capacitance exhibits an unlimited increase at high electrode potentials, which cannot be observed in real systems. This result can be understood through the model's underlying assumptions: Ions feature point-

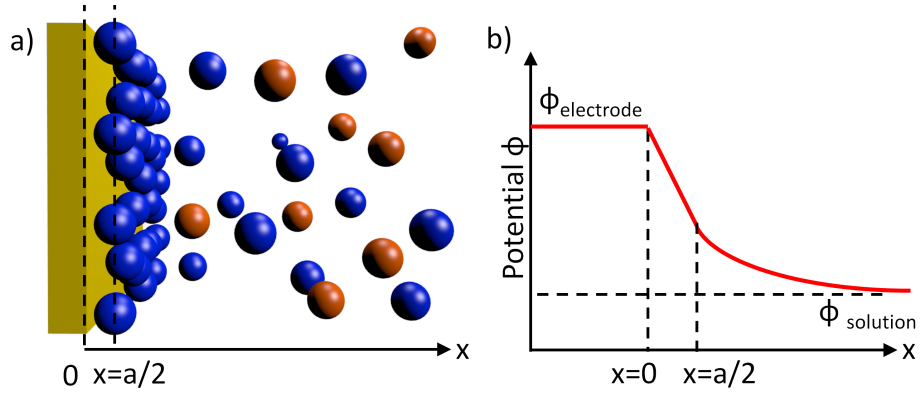

Figure 2.3: Gouy-Chapman-Stern layer: a) Schematic illustration of the interface. Differently colored spheres indicate positively and negatively charged ions. The concentration of the negatively charged (blue) molecules decreases with while concentration of the positively charged red molecules increases. In the bulk solution both concentrations are equal. b) Schematic drawing of the exponential potential profile at the interface.

like dimensions and, hence, can approach the electrode surface infinitely close resulting in huge capacitances at high potentials.

2.3.3 Gouy-Chapman-Stern model

In 1924, Stern attacked this issue by combining the model of Helmholtz and the model developed by Gouy and Chapman. Ions then cannot approach the electrode surface any closer than half of there radius, which results in a homogeneous electric field and a linear potential drop in between $x = 0$ and $x = a/2$. At distances larger than $a/2$, however, the Gouy-Chapman model can be applied using the potential at the outer Helmholtz plane, $\phi_2 = \phi(x = a/2)$ as the electrode potential [4]. This results in the following requirement for ϕ_2:

$$\phi_2 = \phi_0 + \left(\frac{d\phi}{dx}\right)_{x=a/2} \frac{a}{2} \tag{2.17}$$

[4]. The overall capacitance C_{gcs} is then given by a combination of the Helmholtz capacitance C_h and the Gouy-Chapman capacitance C_{gc}

$$\frac{1}{C_{gcs}} = \frac{1}{C_h} + \frac{1}{C_{gc}} \tag{2.18}$$

[4]. An illustration of this model can be found in Figure 2.3.

2.4 Butler-Volmer-Equation

Butler-Volmer equation relates the Faradaic currents at an electrode to the voltage that is applied at the electrode in regard to the solution's potential. It is based on thermodynamic concepts that describe chemical reactions. In this section, we will follow a derivation adapted from Schmicklers derivation [5]. The total reaction rate *v* at an electrode can be understood as the sum of oxidizing and reducing reaction rates, k_{ox} and k_{red}. Hence, it can be written as

$$v = k_{ox} c_{ox}^{int} - k_{red} c_{red}^{int}, \tag{2.19}$$

where $c_{ox/red}^{int}$ represents the concentration of the oxidized or reduced molecule species at the interface. If we now employ Eyring's transition state theory, we can express the reaction rates through the Gibbs potentials ΔG

$$k_{ox} = A * exp\left(-\frac{\Delta G_{ox}(\phi)}{RT}\right) \tag{2.20}$$

and

$$k_{red} = B * exp\left(-\frac{\Delta G_{red}(\phi)}{RT}\right), \tag{2.21}$$

with A and B denoting constants and R representing the universal gas constant. For reasons of simplicity, we expand the Gibbs potential in a first-order Taylor series about the species redox potential ϕ_0

$$\Delta G_{ox}(\phi) = \Delta G_{ox}(\phi_0) + \alpha F(\phi - \phi_0), \tag{2.22}$$

with

$$\alpha = \frac{1}{F} \left.\frac{\partial \Delta G_{ox}}{\partial \phi}\right|_{\phi=\phi_0} \tag{2.23}$$

and

$$\Delta G_{red}(\phi) = \Delta G_{red}(\phi_0) + \beta F(\phi - \phi_0), \tag{2.24}$$

with

$$\beta = \frac{1}{F} \left.\frac{\partial \Delta G_{red}}{\partial \phi}\right|_{\phi=\phi_0}. \tag{2.25}$$

The Faraday constant F was added for illustrational reasons, since $F\phi$ describes the electrostatic contribution to the Gibbs energy.

If we now assume

$$\left.\frac{\partial \Delta G_{ox}}{\partial \phi}\right|_{\phi=\phi_0} = -\left.\frac{\partial \Delta G_{red}}{\partial \phi}\right|_{\phi=\phi_0}, \tag{2.26}$$

we can conclude that

$$\alpha + \beta = 1. \tag{2.27}$$

If we now combine the equations 2.19, 2.20, 2.21, 2.22, 2.24, 2.27, and the Nernst equation

$$\phi = const. + \frac{RT}{zF} ln \frac{c_{ox}^{int}}{c_{red}^{int}}, \tag{2.28}$$

we obtain the Butler-Volmer equation for the current density j

$$j = Fv = j_0 \left(exp \frac{\alpha F(\phi - \phi_0)}{RT} - exp \frac{-(1-\alpha)F(\phi - \phi_0)}{RT} \right) \tag{2.29}$$

with

$$j_0 = F k_0 (c_{red}^{int})^{1-\alpha} (c_{ox}^{int})^{\alpha}, \tag{2.30}$$

where k_0 is the standard exchange reaction rate.

Chapter 3

On-chip redox-cycling techniques

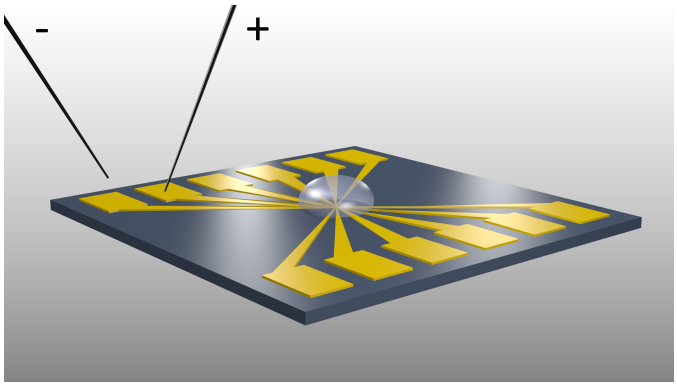

This chapter was reproduced in part with permission from "Enno Kätelhön and Bernhard Wolfrum. On-chip redox-cycling techniques for electrochemical detection. *Reviews in Analytical Chemistry*. 2012, 31, 7-14." The original article is available on www.degruyter.com, DOI: 10.1515/revac-2011-0031.

3.1 Preamble

During the last two decades, redox cycling techniques have evolved as a promising technique for the electrochemical detection of molecules that can undergo subsequent redox reactions. In particular, chip-based techniques received growing attention due to the option of parallel fabrication and easy integration into lab-on-a-chip devices. In this chapter, a review on current implementations of on-chip redox cycling sensors is provided. Advantages and limitations of various approaches are discussed with regard to their fabrication process and performance.

3.2 Introduction

Electrochemical techniques are used in a variety of scientific disciplines ranging from fundamental research on chemical reactions to applications such as fuel cells, solar cells, or sensors for operation in biological or environmental analysis. These sensors utilize certain surface reactions at interfaces between an electrode and a liquid or gaseous sample that link chemical reactions to electrical currents. Measured currents then allow conclusions regarding analyte concentrations or can be studied in order to gain insight into chemical reactions at the device. In most applications, a set of electrode probes that feature inert or chemically-modified electrode surfaces is used in liquid environments. During the measurement, the electrodes are immersed into the sample solution and then biased to a well-defined potential with regard to the solution's potential, which is typically defined via a reference electrode. Thus, chemical reactions of certain molecules may be enabled at the electrode surfaces, while electrode currents are measured. The detected currents, which are usually recorded as a function of the applied voltage as well as the applied voltage's chronological sequence, may then provide information on various characteristics of the sample, such as molecular reactions and diffusion characteristics. Most commonly, such investigations are performed using Amperometry, a method in which a working electrode is biased to a constant potential that is suitable to oxidize or reduce the species under investigation while a reference electrode or a set of a reference electrode and an auxiliary electrode define the solutions potential. The current at the working electrode is then proportional to the number of molecules that react per unit time at the working electrode and can hence

be used to calculate the analyte concentration. However, amperometry only offers little selectivity, since a wide range of molecules can participate in the redox reactions. A more detailed analysis can be done via the method of Cyclic Voltammetry (CV). Here, the electrode potential of the working electrode is repeatedly swept from an oxidizing to a reducing potential in a triangular fashion at a low frequency, while the electrode current is recorded [6, 7]. By this means, a more specific analysis can be performed, since not only the current, but the current as a function of the applied voltage is recorded. Hence, the analysis can also provide information on the analytes redox potential as well as its diffusive behavior. However, even though the CV approach can be used in a wide field of applications, it holds the disadvantage that the overall current and equally the detection limit are always restricted by the mass transfer of analyte molecules towards the electrode surface. This limitation can be overcome to some extent by the method of Fast Scan Cyclic Voltammetry (FSCV), which performs CV measurements at frequencies in the kHz [8] or even MHz range [9]. The sensitivity is then no longer limited by the mass transfer as long as the cycling frequency dominates diffusion and analyte molecules can undergo repeated redox reactions. Fast scan rates also lead to an increased selectivity, because mostly redox-active molecules, i.e. molecules that can undergo repeated redox reactions, are detected. Even though high capacitive background currents and electrode fouling remain challenges in current research [10, 11], today, FSCV is widely used for the detection and investigation of neurotransmitter release of biological cells [12–16].

Many issues regarding sensitivity and selectivity of electrochemical sensors can be eliminated by the application of multi-electrode systems that enable Redox Cycling [17]. In redox cycling, a second working electrode is placed in close proximity to the first electrode, while both electrodes are individually biased to potentials above and below the redox potential of a reversible redox couple. Driven by molecular diffusion, redox-active molecules then participate in repeated redox reactions between the electrodes, while a charge is transferred from one electrode to the other whenever a molecule subsequently reacts at both electrodes, see Figure 3.1. These charges can then be detected as a net current across the electrode gap.

Today, redox cycling sensors are used in a wide field of applications. The large signal amplification and the ability to integrate arrays of microscopic redox-cycling sensors at a high density make the technique interesting for detection of

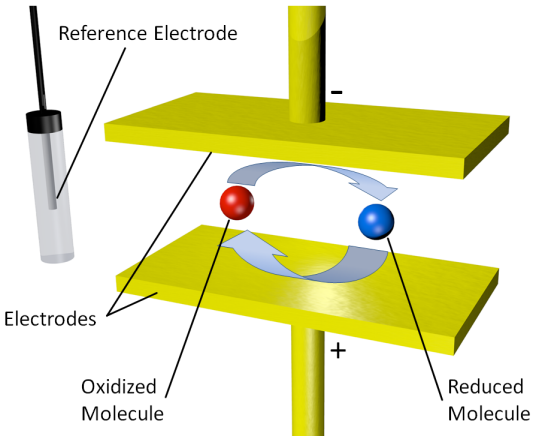

Figure 3.1: Illustration of the redox-cycling mechanism. The sketch depicts the oxidizing and the reducing electrode as well as a reference electrode. Redox-active molecules are indicated by the two spheres, while the red and the blue colorings represent the oxidized and reduced molecule states, respectively.

localized events, such as neurotransmitter release. Hence, redox cycling sensors may evolve to a tool for on-chip neuroscience experiments.

3.3 Redox cycling

The sensing performance of redox cycling devices is mainly determined by the device geometry. Amplification scales with the inter-electrode distance h, since the average time T_s a molecule requires for the shuttling from one electrode to the other highly depends this distance h. The shuttling time T_s for a plane-parallel arrangement can be calculated using a general solution of the one-dimensional diffusion equation:

$$(\Delta x)^2 = 2D\Delta t \tag{3.1}$$

(D describes the diffusion constant). Substituting h for the average spatial displacement Δx and T_s for the average time interval Δt this displacement takes, we obtain:

$$T_s = \frac{h^2}{2D} \tag{3.2}$$

Utilizing T_s, one can now calculate the average cycling current I_{cycl} across the electrode gap, which is caused by a single molecule that is located in between the electrodes and that can transfer n elementary charges e_0:

$$I_{cycl} = \frac{ne_0}{2T_s} = \frac{ne_0 D}{h^2}, \tag{3.3}$$

[18, 19]. In order to quantify the redox cycling amplification of the electrochemical current, different methods can be employed. The simplest approach is given by dividing the current of the working electrode in redox-cycling mode by the current obtained when the same device is used without redox cycling (i.e. only one working electrode is connected) [20]. However, this definition can be misleading for people interested in concentration sensing, since the single-electrode current is strongly dependent on the coupling of the sensor and the bulk reservoir. For example, consider the extreme case of a redox cycling device within a small confined box: Any such device would yield a finite steady state current while operating in redox cycling mode. However, in single-electrode mode, the resulting current will approach zero after all molecules have been either oxidized or reduced to the same state in the box system. Thus, with the definition above, the amplification factor of all strongly confined redox-cycling systems will tend towards infinity. Although the confinement can be an important parameter of the device, it should rather be addressed in terms of efficiency instead of the amplification factor as it will be discussed below. Another, and for concentration sensing more useful, way of defining amplification can be obtained by dividing I_{cycl} by the current that would be expected from a microelectrode I_{me} of the same size due to radial diffusion [19]. For illustration, the current of an ideal redox cycling device with two plane-parallel opposing electrodes at a separation of 50 nm is calculated and compared to the result for a single micro disk electrode of the same size as introduced by Shoup and Szabo [21]:

$$\frac{I_{me}}{4nFDrc_0} = f(\tau) \tag{3.4}$$

Using the definitions:

$$\tau = \frac{4Dt}{r^2} \tag{3.5}$$

And:

$$f(\tau) = 0.7854 + 0.8862\tau^{-\frac{1}{2}} + 0.2146e^{-0.7823\tau^{-\frac{1}{2}}} \tag{3.6}$$

(r represents the radius of the electrode and F the Faraday constant). Then one can determine the amplification factor as a function of the time as well as a function of the electrode radius a. The corresponding plots are shown in Figure 3.3. Using this definition, even at steady state, the amplification factor

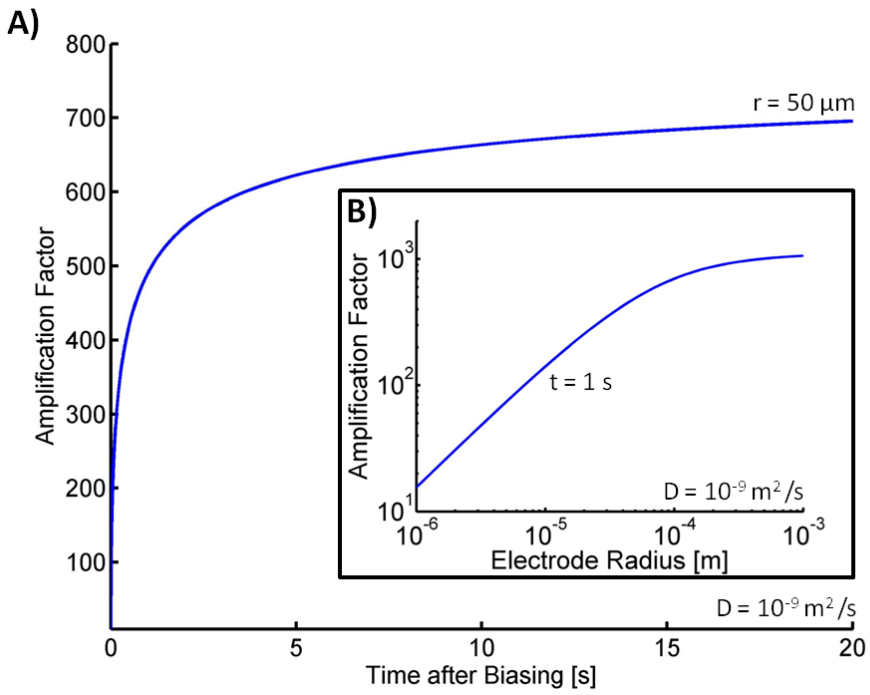

Figure 3.2: Amplification by the redox-cycling effect. The presented plots picture the analytically determined amplification factors of the Faradaic currents obtained from a redox cycling sensor compared to a single ring electrode of equal size. A) presents the amplification as a function of the time passed since the electrode was biased for an electrode radius of 50 μm. B) shows the amplification at t = 1 s as a function of the electrode diameter.

does not reach infinity but stays in the range of three orders of magnitude for a 50 μm radius electrode. From Figure 3.3 B), we see that the amplification factor strongly increases for larger electrodes that approach steady-state values. Hence, the use of redox-cycling in amperometric concentration sensing is particularly effective.

Another important design feature of redox-cycling sensors is the degree, to which analyte molecules are confined in between the electrodes. If a sensor design provides an easy access to the inter-electrode space from the bulk solution, sensors show a fast response to fluctuations in concentration of the analyte. However, the average number of redox cycles that each molecule performs inside the sensor is lower compared to more enclosed designs. This effect is insignificant for most concentration sensing applications, since the net number of molecules inside the sensor remains unaffected. Nevertheless, for certain

concentration measurements or spectroscopic applications, it is desirable that each single molecule performs a large number of subsequent cycles. Examples are given by the detection of the 'recyclable' molecule dopamine in presence of ascorbic acid, which cannot participate in subsequent redox reactions [19, 22] or the applications of redox-cycling sensors in adsorption spectroscopy as it was described by Singh *et al.* [23].

The degree of confinement is highly dependent on the geometry of the surrounding space that is open for diffusion and, hence, depends on a variety of different design features. One approach to define a key number that is related to these features is given by the Collection Efficiency η. It is usually defined as the ratio of the currents I_{gen} and I_{col} at the generating and collecting electrodes [24, 25] and can be calculated as follows:

$$\eta = \frac{I_{col}}{I_{gen}}. \tag{3.7}$$

Even though this definition is very illustrative, its use can be problematic due to the experimentally challenging determination of η. Since measured currents often interfere with other Faradaic currents that can result from various experimental conditions, the isolated recording of the generating and the collecting currents can turn out to be experimentally difficult. On the one hand, the measured value is well dependent on the ratio of oxidized and reduced analyte molecules in the bulk solution, since potentially not only molecules that were generated at the generator contribute to the current at the collector and vice versa. Hence, all analyte molecules in the sample solution have to exhibit the same oxidation state for an exact measurement. On the other hand, the concept does not represent any temporal aspects of the redox cycling itself. If the sensor impacts the analyte concentration in its immediate surroundings or forms a wide depletion layer of molecules that can react at the generator, collection efficiency will be time-dependent. In order to avoid these issues, one can suggest adding two additional criteria for the experimental determination of η: First, the experimentalist assures that the solution only contains analyte molecules of one oxidation state at the beginning of the experiment. This can be achieved via an additional macroscopic electrode in the bulk solution, for example. Second, measurements have to be performed after the system came to stationary conditions in currents and concentration distribution. Since we focus on on-chip sensors, the access to the considered sensors is typically very

small. In analog to microelectrodes, mass transfer towards the sensor is therefore affected by radial diffusion. Hence, mass transfer and Faradaic currents will equally converge to a certain value that can be measured [21].

3.4 Off-chip implementations of redox cycling sensors

First redox cycling experiments were performed in the field of Thin-Film Electrochemistry. During the mid-sixties, the group of Reilley used an electrode that was positioned in close proximity to an electrically conducting anvil, while the inter-electrode distance could be adjusted via a micrometer spindle [26, 27]. Furthermore, both electrodes could be biased individually and the current across the gap could be measured, hence allowing confined redox reactions in between the electrodes. By this means, detailed studies of the redox reactions of the Fe(II) - Fe(III) and the quinone - hydroquinone redox couples were enabled.

During the eighties, other fields of application arose. Among the off-chip techniques, Scanning Electrochemical Microscopy (SECM) evolved as one of the most important methods. This technique was first pioneered by the groups of Bard and Engstrom [18, 28–31] and later advanced by a variety of other groups. Analog to a scanning tunneling microscope (STM), this approach utilizes a microprobe that scans the sample surface. However, contrasting STM measurements, a microelectrode is employed instead of a needle and the sample is immersed in solution. During the measurement, redox cycling can be enabled in between the electrode tip and the substrate. In case redox cycling occurs, this method is usually referred to as positive feedback mode. It allows the mapping of surfaces in detail with regard to their topography and chemical reactivity [32, 33]. In 1995, Fan and Bard employed this approach for the detection of single molecules [18].

Even though advances in thin-film electrochemistry and SECM paved the way for the development of on-chip redox-cycling techniques, in the following, this review will solely focus on on-chip approaches.

3.5 Interdigitated arrays

Interdigitated Array Sensors (IDAs) represent a group of on-chip electrochemical sensors that utilize the redox-cycling technique. IDAs were initially described by

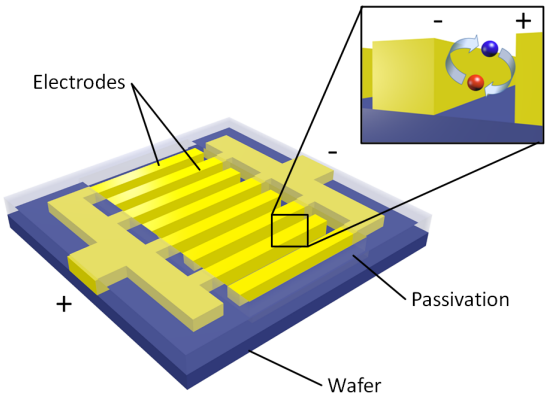

Figure 3.3: Illustration of an interdigitated array sensor. Both electrodes can be biased individually via feed lines that are covered under a thin passivating layer. Inset: Redox cycling occurs in between the electrodes. Oxidized molecules are indicated by a red sphere, reduced molecules by a blue sphere.

Sanderson and Anderson in 1985 and then further studied by other groups with regard to miniaturization and applicability for the detection of various redox-active species [34–37]. Today, IDAs are commonly used on-chip redox-cycling sensors and are employed in a wide range of applications.

A single IDA sensor consists of two coplanar electrodes that feature comb-like shapes and are arranged in an interdigitated fashion, see Figure 3.3. Electrodes are typically fabricated from inert metals and exhibit inter-electrode distances from the nanometer up to the micron scale [38].

In most sensing applications, IDAs are operated in amperometric or cyclic-voltammetry mode. During amperometric operation, electrodes are biased individually to potentials above and below the redox potential of the species under investigation, hence enabling redox-cycling in between the electrodes. The overall current across the electrode gap is then measured and conclusions regarding the analyte concentration can be drawn. In contrast to that, in cyclic voltammetry mode one electrode remains biased to a potential below or above the redox-potential, while the other is repeatedly swept from an oxidizing to a reducing potential and vice versa. During the measurement, the current at the constantly biased electrode is recorded. By this means, cyclic voltammograms are obtained that are mainly limited by the diffusive shuttling of reactive molecules in between the electrodes instead of the diffusive mass transfer from the bulk solution towards the electrode. This mode of data acquisition offers an additional insight into molecular kinetics at the electrode surface in a trade-off for a better temporal resolution in amperometric operation.

Besides their good measurement capabilities, the wide use of IDAs is also based on their comparable simple and cheap fabrication process in comparison

to other microelectrode-based approaches. Simple sensor designs can be fabricated via a single lateral structuring step using microfabrication techniques such as optical lithography or nano imprint lithography for parallelized production or electron beam lithography for prototyping. This results in a quick and inexpensive fabrication of nano-scaled devices. Regarding larger structures, printed electronics evolve as a cheap alternative. However, IDAs also exhibit certain disadvantages. First, the amplification by the redox-cycling effect is always limited by the distance between the electrodes, which itself is limited by the structuring method applied. Therefore, high amplification can only be achieved by sets of nanoelectrodes that were produced via more complex fabrication methods. Also, nanoelectrodes exhibit poorer stability at decreasing structure sizes, which results in shorter disabilities in sensing applications. Second, the redox-cycling efficiency does not reach the level achieved by confined redox cycling approaches, since a significant part of the analyte molecules do not participate in repeated redox cycling but diffuse away.

Recent developments related to the design of IDAs mainly focus on the increase of sensitivity by optimizing the senor geometries towards more confined redox cycling [39]. During the last decade, various methods were introduced that increase the aspect ratio of the interdigitated electrodes for better redox-cycling efficiency [40–42]. Furthermore, performance was increased significantly by scaling the inter-electrode distance down to sizes of 30 nm in IDAs or below 4 nm in a single nanogap [38, 43]. Other developments aim for on-chip signal amplification or processing based on CMOS technology [44–46].

3.6 Pore-based approaches

A different group of on-chip redox-cycling sensors is given by pore-based designs. In contrast to IDAs, which feature electrodes that are positioned in a coplanar fashion on the wafer surface, pore-based designs utilize electrodes that are aligned in parallel to each other and the wafer surface. The sensors consist of a stack of two or more electrodes that are separated by insulating layers for the option of individual biasing. Diffusive access to a bulk reservoir is enabled via small openings in form of pores that interpenetrate the stack, see Figure 3.4. Hence, the inter-electrode distance is no longer limited by the lateral resolution of the structuring method, but by the minimal thickness of the intermediate layer that is still sufficient for electrical isolation. In that way, the inter-electrode dis-

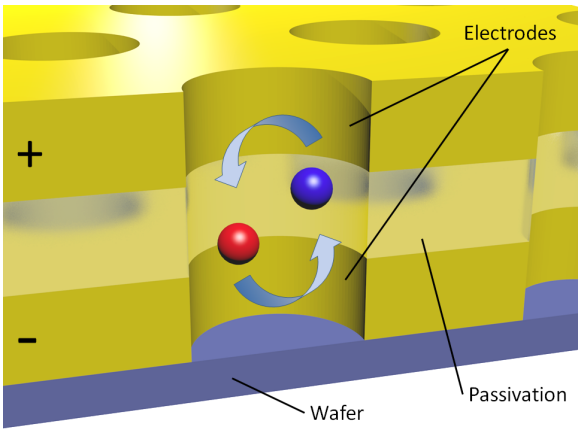

Figure 3.4: Illustration of a pore-based redox-cycling sensor. Two porous metal electrodes are separated by an insulating layer. Redox-active molecules are indicated by the two colored spheres, whereas different colors represent different oxidation states.

tance and thus the redox-cycling amplification can be enhanced significantly, even though the overall active surface of the sensor is smaller in comparison to many other sensor designs. Sensitivity in terms of the ratio of Faraday current per sensor area can be improved further by scaling pore size and electrode spacing down, since the overall available electrode surface is mostly defined via the pore outline and density. Due to their short-access-channel design, open-pore sensors are strongly coupled to the reservoir via molecular diffusion. This coupling increases the sensor's response characteristics to rapid concentration fluctuations making them especially suitable for time-resolved sensing applications. However, good coupling also leads to low degrees of confinement of the molecules inside the sensor pores and equally lowers redox-cycling efficiency and amplification. Since the coupling can be tuned via the aspect ratio of the pores dimensions, there is always a trade-off between temporal resolution and redox-cycling efficiency.

During the last fifteen years, various approaches to technical implementations of pore-based sensors have been described. In 1999, Henry and Fritsch introduced devices that feature stacks of gold electrodes separated by insulating polyimide layers [47, 48]. Each sensor is characterized by a single, several microns wide opening that is etched perpendicularly into the stack in order to enable diffusive access to the bulk reservoir. In operation, electrodes are biased individually to facilitate redox-cycling enhanced electrochemical detection. By this means, dopamine concentrations as low as 2 μM were detected at micron-scaled sensors featuring inter-electrode distances of about 4 μm [49]. Another approach was introduced by collaboration between the groups of Spatz, Stelzle, and Schuhmann in 2006. In contrast to the work by Henry and Fritsch,

here, electrode stacks do not feature only a single pore but are porous themselves [50–52].

Unlike the formerly described sensors, structures are obtained via a bottom up process. During fabrication, self-aligning nano particles are first disposed over the wafer surface and later utilized as a shadow mask in a lift-off process. By this means, dense patterns of pores were obtained that featured pore sizes down to 330 nm at an average spacing of about 650 nm. This method allows distinctly higher densities of active surface area compared to conventional top-down pore-based approaches and, hence, an increased redox-cycling performance. An alternative bottom-up approach to the fabrication of pore-based redox-cycling sensors makes use of nanoporous aluminum oxide templates [53]. Aluminum is deposited directly onto an electrode-insulator-electrode stack and anodized on spot generating nano-scaled pores that form self-aligned in a hexagonal pattern. The porous alumina layer is then used as a shadow mask for reactive ion etching, thus transferring the structure of the porous aluminum into the stack. This approach aims to scale down pore sizes and interpore spacings in a large-scale fabrication process without the use of electron beam or focused ion beam patterning.

3.7 Nanocavity devices

Nanocavity sensors (also referred to as 'Nanofluidic Electrochemical Sensors') currently represent the most spatially confined redox-cycling technique on-chip. First sensors were fabricated in the group of Lemay in 2007 and tested in various fields of application soon after [19, 20]. During the fabrication process, a laterally aligned stack of a micron-sized bottom electrode, a thin sacrificial layer, and a second top electrode are deposited on the wafer surface and subsequently buried under a mechanically stable passivation layer. Afterwards, a small opening is etched into the passivation in order to enable fluidic access to the sacrificial layer. This layer is then removed using an anisotropic etch, hence forming a cavity that separates top- and bottom electrode. Similar to pore-based approaches, the inter-electrode distance is defined by the layer thickness of a deposited layer instead of a lateral structuring method; however, compared to formerly introduced methods significantly larger opposing electrode surfaces can be produced with this technology. In operation, both electrodes are biased individually for redox-cycling through additional feed lines. Diffusive access to

the bulk reservoir is enabled via the opening in the passivation that formerly provided access to the sacrificial layer.

The central advantage of nanocavity sensors is the strong signal amplification in combination with high redox-cycling efficiency, which is due to the large surface areas that are obtained at nano-scaled inter-electrode distances. This combination allows sensitivity down to the ultimate limit: Zevenbergen *et al.* recently demonstrated the electrochemical detection of a single molecule inside a nanofluidic cavity [54]. In their experiment, each individual molecule contributed with an average electrochemical current of 78 fA to the overall current. Although sharp transitions due to molecule fluctuations were not observed because of the limited bandwidth, the results nicely demonstrate the possibilities for single molecule studies using on-chip electrochemical redox cycling amplification. Other advantages of nanocavity devices include the applicability in spectroscopic methods. In 2009, the same group introduced the method of Electrochemical Correlation Spectroscopy (ECS), which determines the fluctuations in the number of redox-active molecules within a given volume [55] and exhibits great potential for the in-depth investigation of adsorption and desorption effects. Another application is given by the characterization of fast electron-transfer kinetics inside of nanofluidic channels [56]. Design related limitations mostly apply to the sensor response to rapid concentration fluctuations. Due to the sensor's comparable high degree of confinement inside the cavity, diffusive coupling between the analyte concentration inside the sensor and the bulk reservoir is weak. This leads to longer response times in case of fast localized changes in concentration. However, for typical sensor designs, this effect impacts sensing performance on the millisecond scale and can be neglected in many applications. Experimentally, temporal sensing applicability for the detection of dopamine was recently confirmed and characterized in microfluidic environments [57, 58].

3.8 Conclusions

It appears to be likely that the recent concepts of nanocavity- and nanopore-based redox-cycling sensors will receive growing attention during the next years and equally expect a steady increase in activity in this field of research.

One the one hand, the production method of these new types of sensors allows the fabrication of highly sensitive devices at comparably low fabrications

costs and efforts. Contrasting IDAs, the inter-electrode distance is not limited by means of lateral structuring but only by the distance of an insulating layer. This can be easily down-scaled to the nanometer level using low-cost and standard clean-room methods, hence enabling ultra-high sensitivity. Also, the required structuring methods are limited to solely optical lithography, which is widely available in research and industry.

On the other hand, one can adopt the view that current research on nanocavity and nanopore devices just started to pioneer a wide range of potential future applications. Particularly, with regard to biosensing, spectroscopic electroanalysis as well as applications in neuroscience there is an enormous potential that is still waiting to be explored. One may further expect advances in theory and simulation science that provide new impulses to the development of novel spectroscopic applications.

Chapter 4

Dopamine fluctuations in microfluidic gradients

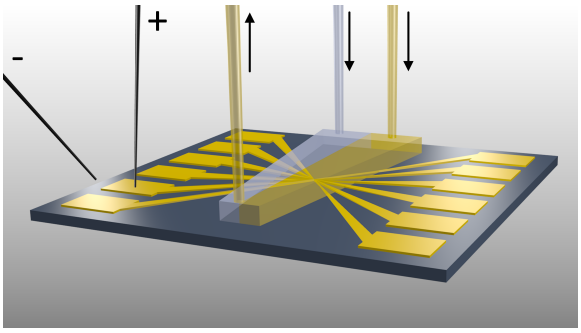

This chapter was reproduced in part with permission from "Enno Kätelhön, Boris Hofmann, Serge G. Lemay, Marcel A. G. Zevenbergen, Andreas Offenhaüsser, and Bernhard Wolfrum. Nanocavity Redox Cycling Sensors for the Detection of Dopamine Fluctuations in Microfluidic Gradients. *Analytical Chemistry*. 2010, 82, 8502-8509. DOI: 10.1021/ac101387f". Copyright 2010 American Chemical Society.

Figure 4.1 and the respective caption were reproduced from: "Enno Kätelhön and Bernhard Wolfrum. On-chip redox-cycling techniques for electrochemical detection. *Reviews in Analytical Chemistry*. 2012, 31, 7-14. The original article is available on www.degruyter.com, DOI: 10.1515/revac-2011-0031.

The fabrication, parts of the characterization, and the development of the microfluidic setup were part of my diploma thesis. Data and micrographs shown in Figures 4.2 and 4.3 have been previously used in my diploma thesis.

4.1 Preamble

Electrochemical mapping of neurotransmitter concentrations on a chip promises to be an interesting technique for investigating synaptic release in cellular networks. This chapter presents a novel chip-based device for the detection of neurotransmitter fluctuations in real-time. The chip features an array of plane-parallel nanocavity sensors, which strongly amplify the electrochemical signal.

The sensor's capability of resolving concentration fluctuations of redox-active species in a microfluidic mixing gradient is demonstrated and the results are explained by a simulated concentration profile that was calculated on the basis of the coupled Navier-Stokes and convection-diffusion equations using a finite element approach.

4.2 Introduction

As already mentioned in the former chapter, redox cycling amplification is a powerful tool for increasing the sensitivity of certain electrochemical measurements [18, 34, 47, 52, 59–67]. Molecules that can undergo reversible redox reactions are repetitively oxidized and reduced at independently biased electrodes, which are located in close proximity to each other. Since the oxidation state is "recycled" after exchanging electrons with the electrodes, this approach allows multiple reactions of a single molecule at the electrode, resulting in an amplified electrochemical signal. The efficiency of this recycling method depends on the average number of cycles a molecule performs before it escapes from the sensor and the time it takes to undergo a complete redox cycle. Thus, it is strongly influenced by the geometry and size of the device [24, 39].

Very efficient redox cycling can be performed in confined geometries where the electrode distance is well below 100 nm. Nanofluidic channels with integrated electrodes have especially demonstrated an increase in molecular sensitivity by several orders of magnitude compared to conventional voltammetry [19, 20, 56]. Another interesting feature of nanofluidic redox cycling sensors is the anticorrelation of the anodic and cathodic current, which is useful for the discrimination of interfering signals. The anticorrelation is also displayed in the current noise that is caused by concentration fluctuations in the sensor and can be exploited to perform electrochemical correlation spectroscopy [55].

The distinct advantages of confined redox cycling make this technique an

interesting candidate for biosensing applications [49, 68, 69]. One application is the on-chip spatiotemporal detection of redox-active neurotransmitters with the prospect to investigate localized release of neurotransmitters from neuronal networks with high sensitivity. It has previously been shown that nanofluidic redox cycling sensors are capable of detecting catechol, a precursor of the neurotransmitter dopamine, in a strong background of ascorbic acid [19]. However, the spatial and temporal resolution of the formerly presented redox cycling devices with double-inlet nanofluidics is limited by long access channels. Furthermore, the fabrication of those devices was based on electron beam lithography, which is not well suited for parallel processing of arrays required for network analysis.

This chapter describes arrays of circular nanocavity sensors which were structured by means of optical lithography. The redox cycling efficiency of these sensors and their applicability for the detection of redox active compounds such as hexacyanoferrate and the neurotransmitter dopamine is demonstrated. Furthermore, it is shown that via the array-based approach, chemical gradients and changes in the local concentration can be spatiotemporally characterized on-chip. This feature is a crucial requirement for future applications such as mapping neurotransmitter release from chemical synapses in a cellular network.

4.3 Methods

4.3.1 Reagents

The photoresists Ma-N 2505 and AZ 5214 E were acquired from Microresist Technology GmbH (Berlin, Germany) and Clariant GmbH (Wiesbaden, Germany). Chromium Etch was obtained from Honeywell Deutschland Holding GmbH (Offenbach, Germany). Dopamine hydrochloride and potassium hexacyanoferrate II were obtained from Sigma-Aldrich Chemie GmbH (Steinheim, Germany). All chemicals were used without further purification.

4.3.2 Devices and fabrication

The redox cycling chip is equipped with one test electrode and 29 nanocavity sensors that are arranged on a grid pattern. Each sensor itself features a circular bottom electrode with a diameter of 15 or 30 μm and a ring shaped top electrode with an outer diameter matching the bottom electrode and an inner diameter of 7 or 9 μm, respectively. Both electrodes are aligned parallel to the wafer surface

and on top of each other, separated by an 65 nm high cavity that is either 20 or 35 μm in diameter. The whole system is stabilized by an approximately 850 nm thick passivation layer, which is opened at 3 or 5 μm wide spots located at the centers of the top electrodes.

Figure 4.1 shows a sketch of the fabrication scheme. The sensor arrays were fabricated on 100 mm silicon substrates employing standard optical lithography (MA-6, SUSS MicroTec AG, Garching, Germany) in a cleanroom environment (class 100). Initially, the silicon substrate was thermally oxidized under wet conditions to grow 1000 nm of SiO_2. After that, bottom electrodes including feed lines and bond pads were patterned via a resist lift-off process using the resist Ma-N 2405, while the electrodes were fabricated by depositing 7 nm Ti, 50 nm Pt, and 7 nm Cr via electron beam physical vapor deposition. In a next step, circular sacrificial chromium layers of 50 nm thickness were deposited via a lift-off (Ma-N 2405) centrally on top of the bottom electrodes. Afterwards, top electrodes including feed lines were deposited (7 nm Cr, 50 nm Pt, 7 nm Ti) and structured by lift-off (Ma-N 2405) on top of the sacrificial layers. The whole device was then insulated by a stack of six alternating layers of silicon nitride and silicon dioxide featuring an overall height of 850 nm using a PECVD process. Access holes were etched via reactive ion etching (Oxford Instruments, Wiesbaden, Germany) at the center of every sensor for fluidic access, whereas the etch mask was structured using a resist lift-off process (AZ 5214 E). The whole wafer was then cut into (11 x 11) mm^2 chips, each containing the sensor arrays in the center and the bondpads at the outer edges of the chip. The sacrificial layers of the individual chips were chemically removed using a wet chromium etch at room temperature. The progress of the sacrificial layer etching was monitored optically and electrically by measuring the resistance between top and bottom electrodes. This etching step generates the nanocavities between the reducing and oxidizing electrodes and finishes the fabrication of the sensor arrays. In the fabrication process, we obtained a yield of approximately 80 percent of functional sensors. A micrograph of a fully processed sensor array and a single sensor unit before the removal of the chromium layer are shown in Figure 4.2.

4.3.3 Microfluidics

The microfluidic channels were fabricated by polydimethylsiloxane (PDMS) casting from an aluminum mold, which was machined in our mechanical workshop.

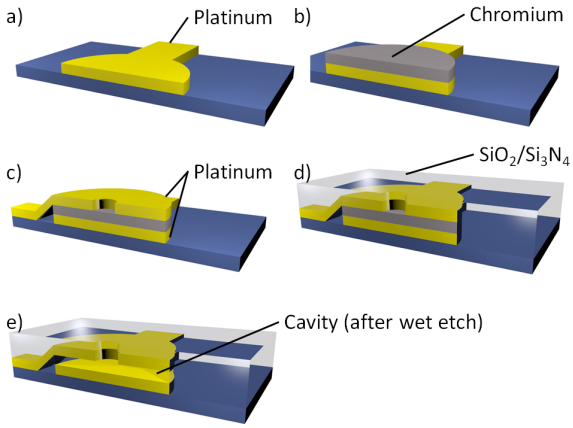

Figure 4.1: Illustration of the fabrication process of a nanocavity redox-cycling sensor in a cross section view. The sketch shows demonstrates the individual production steps, i.e. the deposition of the bottom electrode (a), the sacrificial layer (b), the top electrode (d) and the passivation layer after the anisotropic etch (d). The last picture pictures the final sensor after the removal of the sacrificial layer (e).

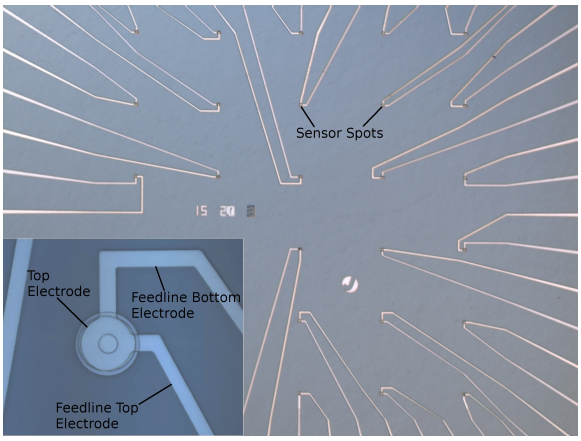

Figure 4.2: Micrograph of a nanocavity sensor array. The image presents a full array of sensors featuring a diameter of 15 μm, while the inset shows a single 30 μm sensor before the opening of the passivation.

In the experiment, this PDMS channel covered most of the active surface of the sensor array. Its T-shape design featured two inlet ports and a single outlet port, which were connected to a poly(methyl methacrylate) (PMMA) flow cell. Each of the inlet ports was connected to a separate channel of a pressure controlled pump (MFCS-4C, Fluigent, Paris, France) and an associated chemical reservoir. The outlet port of the cell led into a waste solution container. By modifying the pressure at the inlets of the flow cell chemical gradients inside the channel could be shifted on top of the sensor array, as explained further below. An illustration of the channel design is given in Figure 4.4.

4.3.4 Electrochemical measurements

Electrochemical measurements were performed in aqueous solutions using two multichannel patch clamp amplifier systems (EPC-10 Quadro PCI and EPC-10 Triple PCI, Heka Elektronic Dr. Schulze GmbH, Lambrecht, Germany), which were controlled by the software "Patch Master". The chips were mounted into the microfluidic chamber and the outer bond pads were connected to the preamplifiers via probe heads (ph 100, SUSS MicroTec AG, Garching, Germany). A standard Ag/AgCl reference electrode (RE-6, BASi, Stareton, United Kingdom, 3 M NaCl solution) was inserted into an access port of the PMMA flow cell and used as a combined reference and counter electrode. During the measurements, the current through the reference electrode was usually well below 1 nA. Thus, an independent counter electrode was not required. Cyclic voltammograms as well as amperometric measurement protocols were programmed for multiple redox cycling sensors and used to characterize the system. The solutions of dopamine and hexacyanoferrate were prepared in a background electrolyte of physiological phosphate buffered saline (PBS) at a pH of 7.3 (specific conductivity 0.65 Ωm). After the experiments devices were cleaned with MilliQ water (Millipore Corporation, Billerica, MA, United States), dried and stored for further reuse.

4.3.5 Numerical simulation

We performed a three-dimensional finite element simulation of the microfluidic gradient inside the flow cell by coupling the incompressible Navier-Stokes equations:

$$\rho\frac{\partial \mathbf{u}}{\partial t} + \rho(\mathbf{u}\bigtriangledown)\mathbf{u} - \eta \bigtriangledown^2 \mathbf{u} + \bigtriangledown p = f \tag{4.1}$$

with the equation for convection and diffusion:

$$\frac{\partial c_{o,r}}{\partial t} + \bigtriangledown(-D_{o,r} \bigtriangledown c_{o,r}) + \mathbf{u} \bigtriangledown c_{o,r} = 0 \tag{4.2}$$

The solutions were calculated in COMSOL Multiphysics (COMSOL AB, Stockholm, Sweden) for the variables **u**, p, and c_o, r, which describe the velocity field, the pressure, and the concentration of the oxidized and reduced redox-active compound, respectively. Other parameters are the density of the solution ρ = 998 kg/m^3, the dynamic viscosity $\eta = 10^{-10}$ Pa s, and the diffusion constant of the oxidized and reduced redox-active molecules $D_{o,r} = 6.5 * 10^{-10}$ m^2/s. Body forces f, such as gravity, can be neglected in the simulation. The time dependent boundary conditions for the coupled equation system were given by the measured pressures at the inlets (data not shown) and the bulk concentrations of the redox-active molecules. Further coupling of the reduced and oxidized species at the sensor electrodes can be introduced by using the potential dependent Butler-Volmer equations. However, we assume that the concentrations in the experiment are predominantly governed by the convective flow in the microfluidic chamber. For that reason, this additional aspect is excluded in the present model. Symmetry boundary conditions were given by the chip and the walls of the microfluidic chamber. The geometry of the flow cell was assumed to be an ideal replica of the fabrication mold, whose geometry was imported into the software to define the location of the boundaries. The relative positions of the sensor locations to the microfluidic channel were obtained via optical microscopy.

4.4 Results and discussion

4.4.1 Redox cycling response

The nanocavity redox cycling sensors were characterized in phosphate buffered saline containing either potassium hexacyanoferrate or dopamine as a redox-active substance. Figure 4.3a shows the cyclic voltammograms of the 30 μm wide sensor for five different concentrations of hexacyanoferrate. The graphs exhibit a current wave with inflection points between 300 mV and 450 mV. Nevertheless, the current does not reach the full saturation at higher poten-

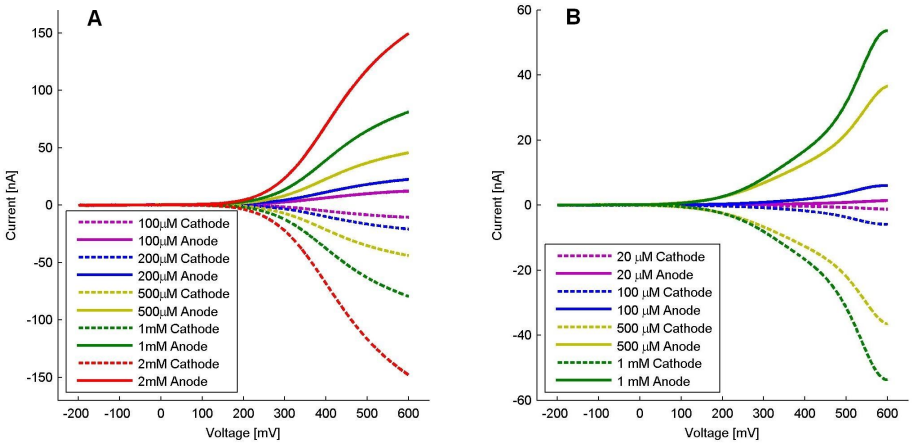

Figure 4.3: Voltammograms of a 30 μm wide nanocavity redox cycling sensor in PBS at different concentrations of potassium hexacyanoferrate (A) and dopamine (B). The anodic potential was swept from -200 mV to 600 mV versus an Ag/AgCl reference electrode, while the cathode was constantly biased to -200 mV. A) The data was recorded at a sweep rate of 80 mV/s. The measurement was run after a balancing time of 5 s, during which both electrodes were biased to -200 mV. B) The sweep rate was 20 mV/s, and before each measurement both electrodes were cycled twice at 20 V/s between -1 V and +600 mV.

tials. Moreover, the inflection point of the graph is located significantly higher than the expected 220 mV versus Ag/AgCl [70, 71]. This can be explained by potential-dependent limitations in the electron kinetics at the electrode. Such limitations may be caused by fouling of the electrodes or residual layers from the production process.

The dependency of the current on the concentration of hexacyanoferrate was determined in an amperometric measurement. The graphs of the absolute anodic and the cathodic currents exhibit similar linear courses with essentially identical magnitudes demonstrating the sensors high redox cycling efficiency of nearly 100 percent. We observed the same results when switching anode and cathode of a sensor. This shows that the current amplification by the redox cycling effect significantly exceeds the current contributions caused by the different electrode geometries. However, deviations from the theory can be found with regard to the size of the overall signal at the maximum voltage difference between the electrodes. Since the redox potential of the species under consideration is 220 mV and the anodic and the cathodic potentials were set

to 600 mV and -200 mV, respectively, the redox molecules should feature a high reaction probability at the electrodes. Considering only limitations in the diffusive mass transport to the electrode surfaces, we can estimate an upper boundary for the electrode currents:

$$i_{cycl} = \frac{< n > Dze_0}{h^2} \tag{4.3}$$

where $< n >$ is the average number of molecules in the sensor, $D = 6.5 * 10^{-10}$ m^2/s the estimated diffusion coefficient, ze_0 the transferred charge and h the distance of the two electrodes [19]. However, the measured currents of the 30 μm sensor shown in Fig. 4.3 amount to only 12 percent of the predicted value. This trend is observed for most of the sensors throughout a batch although single chips temporary exhibited significantly higher currents. As discussed above, this effect may partially be explained by kinetic limitations at the electrodes or by misalignment during lithography. Possible buckling of the upper electrodes would also lead to a decrease in the measured current. Nevertheless, the response of all sensors showed the characteristic anticorrelated behavior for anodic and cathodic currents with almost 100 percent cycling efficiency. The anticorrelation of the anodic and cathodic signals was also represented in the current noise caused by the number fluctuations in the sensor.

Further cyclic voltammograms have been recorded in presence of dopamine (see Figure 4.3b. For concentrations below 500 μM, the graph exhibits one inflection point and currents remain almost unaffected by changes in the applied potential beyond a certain distance to the inflection point. In the plot, we can find the inflection point between 300 mV and 500 mV, which is in line with the results obtained from various electrochemical methods [22, 42, 72]. However, the graph does not reach full saturation at higher potentials. This again suggests that the electrode surface is partially passivated by a blocking layer, which retards the electron kinetics in dependence of the applied electrode voltage. Interestingly, at higher concentrations the current response for dopamine did not exhibit a strictly linear behavior. Furthermore, during prolonged measurements in dopamine, we observed a decrease in the electrode currents, probably due to adsorption and chemical reactions at the electrode. This effect was partly reversible by performing fast scan cyclic voltammograms between -1000 mV and +600 mV at 20 V/s. As expected, both anodic and cathodic currents feature similar magnitudes at equal concentrations. Thus, the sensor shows a high cy-

cling efficiency and absolute measurements of the dopamine concentration can be achieved without the direct interference of substances that do not undergo redox cycling. However, the discrimination between very similar molecules such as dopamine and norepinephrine will remain difficult and additional techniques have to be considered if further selectivity is required. The sensors were stable over periods of months in air and more than a week if stored in phosphate buffered saline or under cell culture conditions (F12 Kaighn's Medium, Invitrogen GmbH, Karlsruhe, Germany, at 37°C, 99% rel. humidity and 5% CO2)

4.4.2 Detection of chemical fluctuations

To demonstrate the possibility for spatiotemporal detection of chemical fluctuations we applied a shifting microfluidic gradient on top of the nanofluidic sensor array inside a microchannel, which was described in the experimental section. During the measurement, the chip was incorporated into the flow cell, while six electrodes in three sensors were used simultaneously in redox cycling mode. These sensors were located as indicated in Figure 4.4 and measured the concentration of redox active species amperometrically throughout the experiment. At the same time, two sample solutions were injected at the two inlets, while the applied pressures were varied periodically at a phase shift of about 180 degrees. The two inlets were supplied with different PBS solutions, one containing a redox active substance and the other being a pure PBS solution. Thus, a time dependent chemical gradient was formed inside of the channel. For a clearer presentation of the acquired redox cycling currents, we present the sensor responses as a fraction of the maximum response that was obtained during the measurement. The recorded anodic and cathodic currents, which were acquired in presence of hexacyanoferrate, are shown in Figure 4.5. The plot shows that the measured signals at the sensors change periodically with the frequency of the applied pressures. Moreover, the sensor responses of the individual sensors vary in accordance to their position in the microchannel. In particular, it can be seen that the responses of the two sensors (A and B) on the one side of the channel exhibit an earlier and longer lasting response in periodic time than the sensor (C) on the other side of the channel.

The concentration profile inside the channel was simulated via a finite element approach. The full geometry of the microchannel and its inputs was transferred into the software and the chronological sequence of the dopamine concentration field in the channel was modeled on the basis of the incompressible

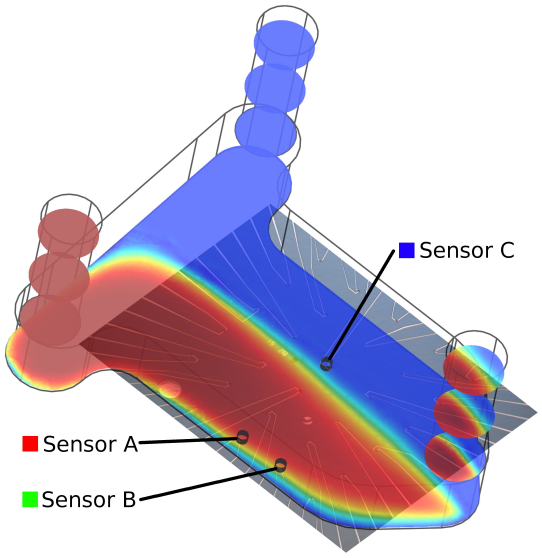

Figure 4.4: Schematic drawing of the nanofluidic sensor array in the microchannel. The geometry of the microchannel with two inlets and one outlet is indicated by the wire frame. The semi-transparent colors represent a snapshot of the concentration distribution of redox-active species at four horizontal cross sections. Red and blue indicate maximal and minimal concentrations, respectively. The distance between sensor A and B is 400 μm.

Navier Stokes Equation and the equation for convection and diffusion. The concentrations at the locations of the three sensors were extracted from the results of this simulation. The concentration field as well as the local concentrations at the sensors is shown in Figure 4.6. The plot shows that the hexacyanoferrate concentration varies at the spots of all three sensors. In the simulated periodic time, the concentration rises first at the sensors A and B. After that, all three sensors are exposed to a high concentration, before the concentration first drops at sensor C and eventually at the sensors A and B. It can be seen that the sensors A and B are exposed to a similar temporal concentration profile, while the profile at sensor B is slightly delayed in regard to the one at sensor A.

In principle, the experimental and the simulated results represent different types of information. While the experimental sensor signals display the measured electrode currents, the simulation provides information on the concentrations of redox-active species at the locations of the sensors. However, since both signals are connected via the frequency-dependent sensor transfer function $H(f)$, the simulated concentrations can be used as a reference for the recorded currents at the sensors. In this way, an exact experimental measurement of the concentrations can be achieved via a deconvolution of the measured signals after the determination of $H(f)$. However, due to the size of the sensors it can be expected that the timescale, on which $H(f)$ differs from 1 in response to local concentration fluctuations, is smaller than the resolved timescale in the experi-

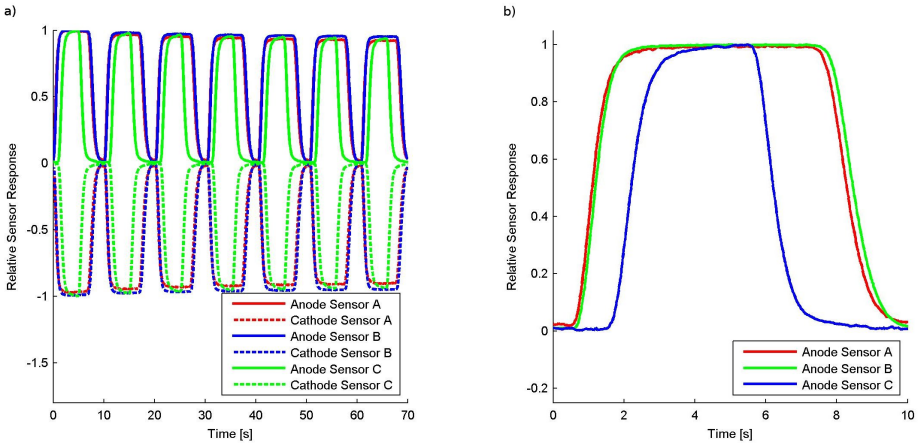

Figure 4.5: Spatiotemporal measurement of a hexacyanoferrate gradient in a microfluidic channel. b) represents an enlarged excerpt from the data shown in a). The upper graphs represent the normalized anodic currents, while the lower graphs show the normalized cathodic currents of the respective sensors. Each graph is normalized to the maximal absolute value of the respective sensors response. During the measurement, the right inlet in flow direction was supplied with 2 mM hexacyanoferrate in PBS solution, while the left inlet was supplied with pure PBS solution. The pressures at the two inlets were swept contrarily at a frequency of 0.1 Hz. Amperometric measurements were performed versus a Ag/AgCl reference electrode, while the anode and cathode were biased to 600 mV and -200 mV, respectively. The data in this plot was recorded at a frequency of 500 Hz. For a clearer presentation we applied a standard median filter of the order 50 and every fifth point is shown in the graph.

ment. Thus, one may assume an ideal signal transfer ($H(f) = 1$), i.e. the local concentrations at the sensors correspond to the recorded currents. Hence, we can in good approximation compare the normalized simulated concentrations in Figure 4.6 with the normalized sensor responses in Figure 4.5. In doing so, we find that the overall characteristics of the simulated responses are in agreement with the experimental data. However, deviations regarding the exact timing of the sensor responses are visible. Especially, the increase in concentration at sensor C was detected later than expected from our simulation with regard to the responses of sensor A and B. These deviations may either be caused by inaccurate modeling of the system geometry or by improper determination of exact boundary conditions, which both potentially may affect the simulation. In particular, the sensors switching characteristics in simulation and experiment

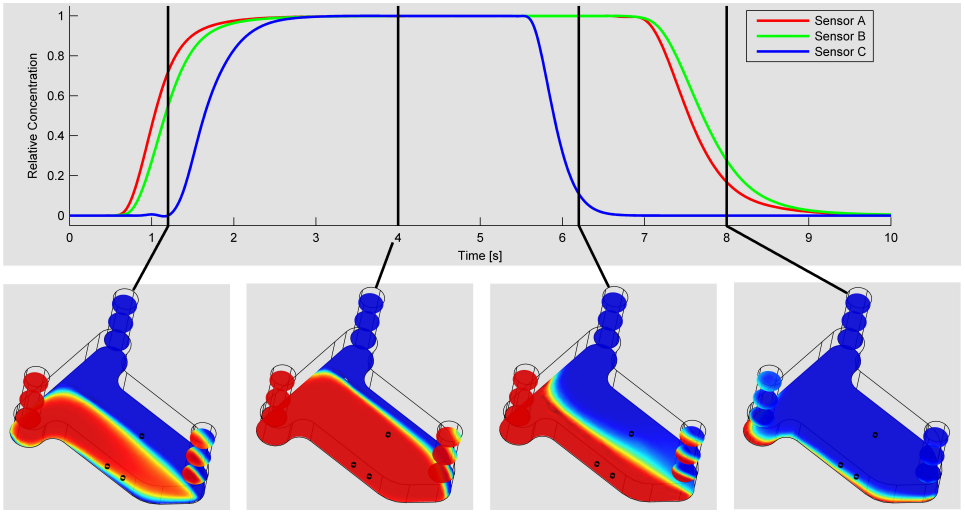

Figure 4.6: Finite elements simulation of the time-dependent dopamine concentration field in the microchannel. The upper graph shows the temporal evolution of the simulated dopamine concentration at the locations of three nanofluidic redox cycling sensors (see Fig. 4.4). The lower part shows four snapshots of the concentration profiles in the horizontal cross sections.

support these assumptions. Both, the experimental data and the simulation show the same trends for the switching characteristics. This fact suggests that deviations were caused by inaccurate modeling of the exact system geometry or boundary conditions in the simulation rather than a malfunction of the sensor array. The limit for the temporal resolution of the sensor response is determined by the diffusion and mean residence time of the molecules inside the nanocavity.

In regard to future applications such as the characterization of neuronal activities, the sensor arrays' abilities in detection of localized neurotransmitter fluctuations are particularly interesting [13, 16, 73, 74]. Figure 4.7 presents the sensors' responses obtained from measurements using the neurotransmitter dopamine. In the plot, it can be seen that the sensor response changes periodically with the frequency of the applied pressure, thus demonstrating the detection of localized changes in concentration. However, the maximum current decreases throughout the measurement. This effect has already been widely discussed in literature. Various groups reported that dopamine can be electropolymerized during the reaction at the electrode, which causes a passivation of the electrode surface [75]. Hence, electrochemical measurements in presence of dopamine may lead to the deposition of a solid layer on the electrode surface

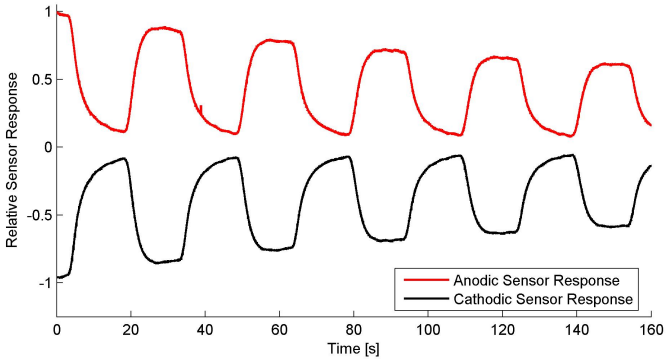

Figure 4.7: Temporal measurement of the dopamine concentration in a microfluidic channel. The upper graphs represent the anodic current, while the lower graphs show the cathodic currents of the respective sensors. During the measurement, a 1 mM dopamine in PBS solution was used as the redox active substance and the applied pressures were varied at a frequency of 0.033 Hz. All other settings were chosen in accordance to the specifications in Figure 4.5

and result in a steady decline of the measured current, potentially impacting quantitative measurements. Accordingly, an electrode passivation by dopamine reaction products appears to be an explanation for the measured data. However, a variety of different methods to overcome this issue have been reported during the last decades, among which surface coatings by thiol groups like MPA seem to be one of the most promising approaches [76]. Nevertheless, the time-integrated exposure of dopamine resulting from actual neuronal communication is significantly smaller than that used in the experiment. Thus, a negligible impact of this effect can be expected in experiments including long-term culture of neuronal cells.

4.5 Conclusion

A novel chip-based device for the spatiotemporal detection of chemical gradients was introduced. Following the nanofluidic redox cycling approach, this device utilizes arrays of circular nanocavity sensors. Each sensor features two independently biased electrodes, which are separated by an 65 nm wide gap. The sensors were characterized using the redox active substances hexacyanoferrate and the neurotransmitter dopamine. The theoretically predicted dependency of the sensor response on the changes in concentration was verified. Moreover, the

applicability of the device in spatiotemporal measurements was demonstrated. To this end, time-dependent concentration fluctuations were generated in a microfluidic channel, while the redox-cycling current was simultaneously measured at various positions in real-time. A finite element simulation supports the experimentally obtained results. Since the developed fabrication process is solely based on optical lithography, the devices are suitable for large-scale production processes. Thus, the sensors can potentially be incorporated into lab-on-a-chip applications.

Chapter 5

Nanocavity cross-bar arrays for high-resolution electrochemical imaging

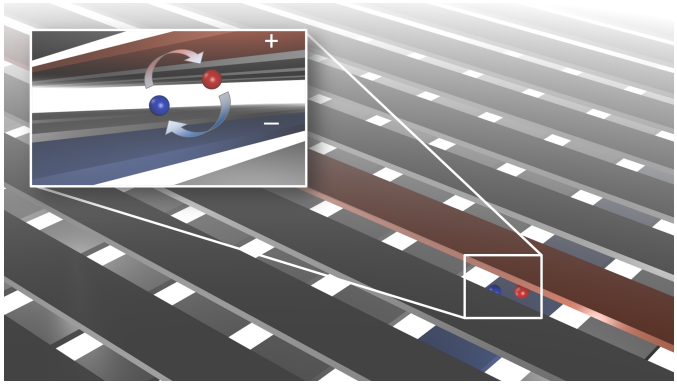

This chapter was reproduced in part from the unpublished work "Enno Kätelhön, Dirk Mayer, Marko Banzet, Andreas Offenhäusser, and Bernhard Wolfrum. Nanocavity cross-bar arrays for high-density electrochemical imaging" (in preparation).

5.1 Preamble

This chapter introduces a novel device for the mapping of redox-active compounds at high spatial resolution based on a crossbar electrode architecture. The sensor array is formed by two sets of 16 parallel band electrodes that are arranged perpendicular to each other on the wafer surface. At each intersection, the crossing bars are separated by a ˜65 nm high nanocavity, which is stabilized by the surrounding passivation layer. During operation, perpendicular bar electrodes are biased to potentials above and below the redox potential of species under investigation, thus, enabling repeated subsequent reactions at the two electrodes. By this means, a redox cycling current is formed across the gap that can be measured externally. As the nanocavity devices feature a very high current amplification in redox cycling mode, individual sensing spots can be addressed in parallel, thus, enabling high-throughput electrochemical imaging. This chapter introduces the design of the device, discusses the fabrication process and demonstrates its capabilities in sequential and parallel data acquisition mode using a hexacyanoferrate probe.

5.2 Introduction

Redox cycling represents a powerful method for the detection of analytes that can participate in repeated redox reactions [18, 34, 37, 39, 50, 61, 77, 78]. Sensors typically use two electrodes that are located in close proximity to each other and can be biased individually. During operation one electrode is set to a potential above the redox potential E_0 of the analyte under investigation, while the other electrode is set below this potential. Molecules can then repeatedly participate in subsequent redox reactions at the electrodes, hence forming a current across the gap. This current can then be measured externally and allows drawing conclusions on a variety of analyte or reaction characteristics such as the electrode kinetics or the analyte concentration.

A distinct advantage of this technique over conventional amperometry, using a single working electrode, is given by the increased Faradaic current caused by the redox cycling effect. A single molecule entering the sensor does not only contribute with an individual charge transfer to the Faradaic current but participates in multiple reactions that each result in a charge transfer to the working electrode. Sensitivity differs among sensor designs and is mainly deter-

mined by the collection efficiency of the sensor and the average time a molecule requires for passing one redox cycle. Hereby, the highest sensitivity per electrode area was reported for nanofluidic redox cycling sensors. These sensors feature micron-sized electrodes that are arranged in parallel to each other and the wafer surface, being separated by a nano-scaled gap [17,79,80]. The current per molecule obtained with such a sensor featuring the inter electrode distance h is directly proportional to h^{-2}, hence small inter-electrode distances can significantly amplify the electrochemical signal [19, 57]. So obtained amplification factors that can be calculated via comparison to a single electrode of the same size may reach several orders of magnitudes, thus allowing very low detection limits: Recently, Lemay's group reported the ultimate detection limit by sensing a single ferrocene molecule inside a nanofluidic redox cycling device [54, 81]. Besides the advantages of electrochemical amplification, redox cycling sensors allow to form large, dense arrays of electrochemical sensors that are highly desirable for applications such as on-chip parallel biosensing or the detection of chemical communication in a neuronal network. This can be achieved via the organization of feed lines in a perpendicular arrangement. Individual sensors are then located at each of the feed line intersections. Redox cycling is enabled at the intersection by setting the potentials of two orthogonal feed lines to values above and below the redox potential of an analyte. Even though faradaic currents may also occur at all other electrodes that are connected to the biased feed lines and are exposed to redox-active molecules, their individual contribution to the overall measured current is comparably small due to the strong amplification by the redox cycling effect. Hence, individual sensors can be easily read out by this method.

Addressable redox cycling electrode arrays have been pioneered by the group of Matsue since 2008 and various designs have been reported since then. Implementations include systems, which consist of two wafers that are glued face-to-face to each other while both wafers hold parallel bar electrodes [62, 82], arrays of ring-ring-based sensors with orthogonal feed lines [83], and designs featuring interdigitated electrodes at the intersections [84]. Reported applications include gene-function analysis [82], electroluminescence detection [85], mapping of cell topographies [86], detection of cellular enzyme secretion [83], detection of DNA hybridization [87], and evaluation of embryoid bodies [88]. So far these approaches have been limited to sequential data acquisition and relatively large lateral intersensor spacings, which limit the temporal and spatial resolution of

the method.

This chapter describes the design and fabrication of a crossbar-based nanocavity redox cycling sensor array that combines the advantages of the two approaches: crossbar architecture and nanocavity sensors. The large redox cycling amplification of the nanocavity sensors allows such arrays to be operated in a parallel readout for high-throughput applications. The redox cycling response during electrochemical imaging using parallel data acquisition is demonstrated and different modes of operation for its future use in mapping neurochemical events are discussed.

5.3 Methods

5.3.1 Sensor design

Our device features two orthogonal sets of each 16 parallel bar electrodes. These electrodes are 14 μm wide and fabricated in parallel to the wafer surface. At each intersection, the electrodes are separated by a ˜65 nm wide gap, while the arrangement is stabilized by a thick passivation layer that covers the whole device. The inter-electrode area is connected to the bulk reservoir via small access channels that interpenetrate the passivation layer and enable diffusive access to a bulk reservoir. An illustration of the sensor array and a top view microscopic image as well as cross sections of the nanocavity sensor, cut by a focused ion beam (FIB), can be found in Figure 5.1.

5.3.2 Fabrication

Devices are structured by means of optical lithography and are processed in class 100 cleanroom facilities. Nanocavities at the intersections between platinum electrodes are formed via the deposition of a sacrificial layer followed by an isotropic etch. The full device is stabilized by a silicon oxide/silicon nitride stack.

The sensor is fabricated on a thermally oxidized silicon substrate while all structures are formed via a lift-off processes. Electrodes are fabricated by depositing a Ti/Pt/Cr stack that features the thicknesses 7/50/7 nm using electron beam evaporation. In the next step, 50 nm thick chromium sacrificial layers are deposited at the positions of the future intersections. These layers define the geometric features of the nanocavities. Afterwards, the top electrodes are

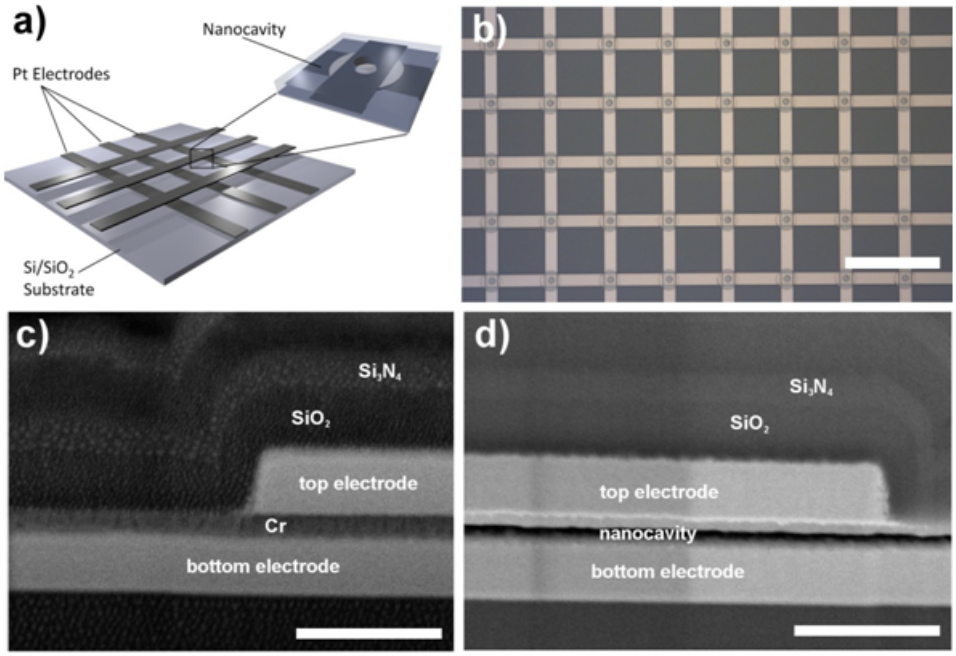

Figure 5.1: Nanocavity array chip: a) Illustration of a sensor array. The inset sketches a nanocavity sensor that can be found at each feed-line intersection. b) Microscopic top view of a part of the array. c,d) scanning electrochemical microscope images of FIB-induced cross sections of a nanocavity sensor before (c) and after (d) removal of the sacrificial chromium layer. The scale bars for the images in (b), (c), and (d) are 100 μm, 400 nm, and 400 nm, respectively.

fabricated from an electron-beam evaporated stack of Cr/Pt/Ti stack of the thicknesses 7/50/7 nm. Subsequently, a passivation composed of alternating layers $SiO_2/Si_3N_4/SiO_2$ is deposited via plasma enhanced chemical vapor deposition. In the next step, access holes are etched into the passivation down to the chromium sacrificial layer by reactive ion etching. The chromium is then removed in an isotropic wet etch using chrome etch solution.

5.3.3 Electrochemical methods

Electrochemical characterization is either performed via cyclic voltammetry or amperometry. Cyclic voltammograms or recorded using an EPC 10 patch clamp system (HEKA Elektronik Dr. Schulze GmbH, Lambrecht, Germany) and the corresponding software Patch Master. Hereby, one bar electrode is swept from -200 mV to 600 mV and vice versa at a speed of 80 mV/s, while the corresponding other electrode(s) remain on a reducing potential of -200 mV. Parallel redox cycling amperometric measurements for electrochemical imaging are performed using a home-built amplifier system (picoAmp64) [89]. The electrodes are set to constant potentials of either -200 or 600 mV. All measurements are performed after a balancing time of 10 s, while the solution's potential is controlled via an Ag/AgCl reference electrode.

5.4 Results and Discussion

Our sensors offer two different modes of operation: The sequential and the parallel readout mode. During sequential data acquisition, each crossing point on the sensor is addressed individually one after the other, while the electrochemical image of the sensor surface is assembled afterwards. As it can be seen in Figure 5.2a), two electrodes that are arranged perpendicular to each other are set to potentials above and below the redox potential, while all other electrodes remain unbiased. Hence, redox cycling is enabled at the corresponding intersection and the respective redox-cycling current can be detected at both electrodes. In parallel acquisition mode, however, two or more electrodes that are arranged perpendicular to the one oxidizing electrode are biased to reducing potentials. Hence, redox cycling is enabled at each intersection between a reducing electrode and the oxidizing electrode, thus, resulting in a row-wise read-out. As sketched in Figure 5.2b), the intersection's individual redox-cycling

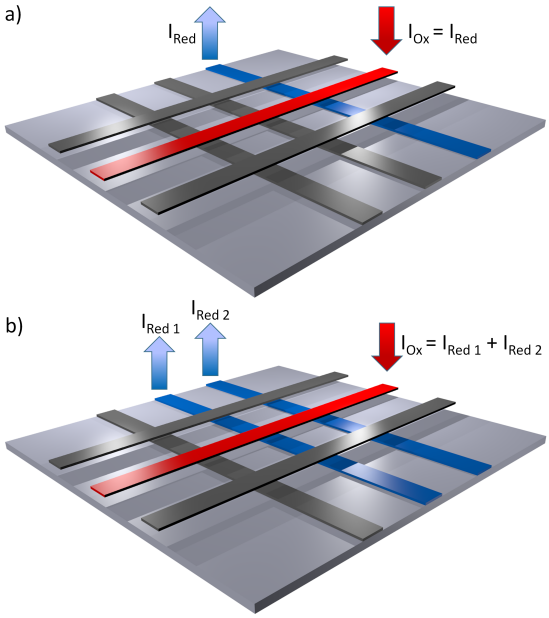

Figure 5.2: Illustration of the two modes of operation: a) Sequential data acquisition; each intersection is read out sequentially. b) Parallel data acquisition; intersections are read out simultaneously in a row-wise fashion.

currents can be measured at the reducing electrodes, while the current at the oxidizing electrode amounts to the sum of all other redox cycling currents.

Figure 5.3 compares data of the sensor during operation in both acquisition modes. Hereby, both graphs exhibit some characteristics in common: Below the redox potential, which can be found around 180 mV, the current does not increase with the anodic voltage. However, above the redox potential there is a fast increase in current, which is due to the now enabled redox cycling. Nevertheless, the current does not reach full saturation at higher voltages. This effect can be attributed to kinetic limitations that may be caused by impurities on the electrode surfaces that remain from the fabrication process. Furthermore, in both cases the anodic and the sum of the cathodic currents equal. Thus, redox cycling inside the sensor is highly efficient.

Figure 5.4 demonstrates the concentration dependency of an individual sensor. Hereby, a single intersection was characterized at varied concentrations of hexacyanoferrate in sequential acquisition mode. As it can be seen in the plot the redox cycling current scales approximately linearly with the concentration. The slope of the sensor response was obtained via a linear regression yielding a sensitivity of 2.4 $\pm$ 0.2 x 104 A m^{-2} M^{-1} in the overlapping electrode area (1.68 x 10-12 m^2). Figure 4 shows a typical sensor response but the array exhibits a large variance in sensitivity making it necessary to calibrate individual

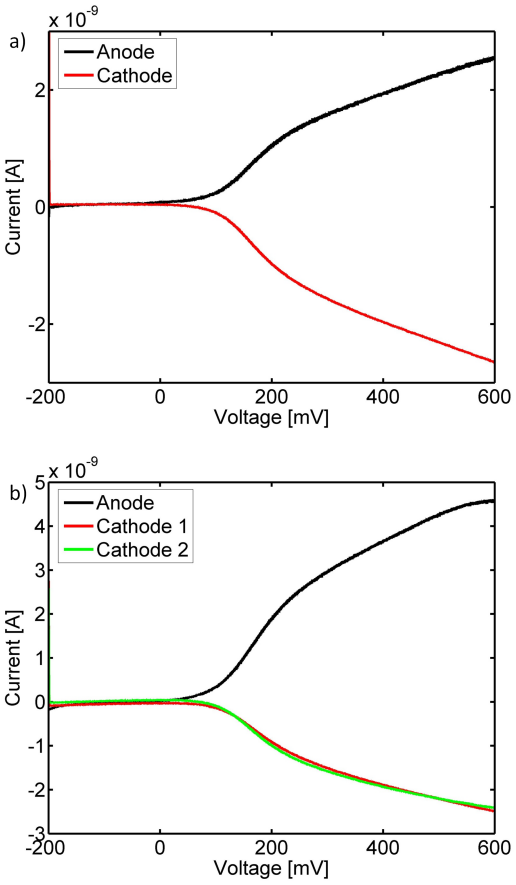

Figure 5.3: Redox cycling currents: a) Cyclic voltammogram detected in sequential data acquisition mode at a single intersection. b) Cyclic voltammograms recorded at two intersections during parallel acquisition. Both data sets were recorded in 1 mM hexacyanoferrate in PBS and filtered via a Butterworth filter. Furthermore, the data was offset corrected and traces recorded in a single electrode setup were subtracted from the anodic currents in order to isolate the respective redox cycling currents.

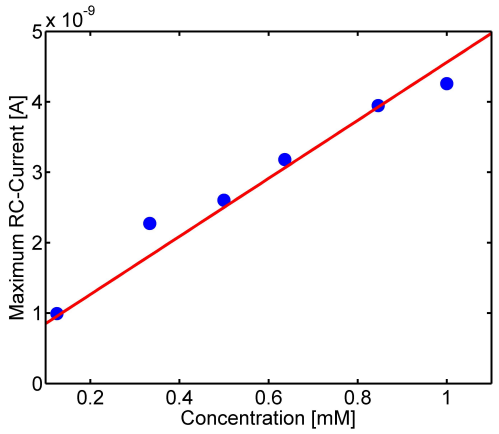

Figure 5.4: Concentration dependency of an intersection in sequential data acquisition. Data was recorded during cyclic voltammograms at different concentrations of hexacyanoferrate in 100 mM KCl and represents the difference between the peak current and a measurement using only the background electrolyte.

sensors for quantitative imaging. The largest current responses obtained were in the range of 1.7 x 10^5 A m^{-2} M^{-1}, which is still significantly less than the theoretically expected diffusion-limited value for the devices if we neglect kinetic limitations:

$$\frac{I}{c * A} = \frac{1000 * D * F}{h} = 9.5 * 10^5 \frac{A}{m^2 M}. \tag{5.1}$$

Here, c is the concentration in (mol/l), A the overlapping electrode area in m^2, D = 0.64 x 10^{-9} m^2/s the diffusion coefficient, F = 96485 C/mol the Faraday constant, and h = 65 nm the nanocavity height. Deviations between expected and recorded current responses in nanocavity devices have been observed previously and are thought to depend on fabrication inhomogeneities and residues as well as adsorption effects limiting the electrode kinetics.

In order to demonstrate the electrochemical imaging capabilities of the device, the dissolution of a hexacyanoferrate crystal on top of the sensor array is monitored. For this purpose, all but one electrode are biased to a reducing potential of -200 mV, while the one electrode is biased to an oxidizing potential of 600 mV. In this operation mode, redox cycling mode is simultaneously enabled at all 16 sensors along the oxidizing electrode and the respective sensor signal can be read out at the corresponding perpendicular cathodes. The device is then calibrated in plain 100 mM KCl solution as well as in a 1 mM hexacyanoferrate solution in order to linearly interpolate the response curve for the individual sensors. After adding the 1 mM hexacyanoferrate solution, three sensors that are located next to each other (the yield of functional sensors is approximately 40%) are chosen and a hexacyanoferrate crystal is added to the solution. The so

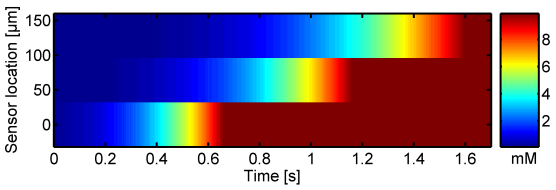

Figure 5.5: Electrochemical image of a hexacyanoferrate crystal that dissolves above the sensor surface.

obtained electrochemical image of its dissolution after background subtraction can be seen in Figure 5.5. The parallel readout of the crossbar array allows the chemical concentration to be mapped with a millisecond temporal resolution, which is sufficient for resolving fast dissolution processes. The sensitivity is determined by the height of the nanocavities (65 nm) while the spatial resolution relies on the sensor array density (˜$244/\mathrm{mm}^2$). In principle, the crossbar array design could allow high density mapping in the range of $10000/\mathrm{mm}^2$ for reasonable cross bar pitches of 10 μm as obtainable by conventional optical lithography.

5.5 Conclusions

This chapter introduced the design and fabrication of a novel device for the electrochemical on-chip imaging of redox molecules by redox cycling. The presented chip was fabricated with standard cleanroom technology and features nanocavity redox cycling devices in a crossbar architecture for sensitive electrochemical detection at a high sensor density. Measurements in hexacyanoferrate solution are shown and different modes of operation are demonstrated: the sequential readout of individual sensors and the parallel readout mode, which allows the spatiotemporal sensing along one feed line.

It can be assumed that the presented technique, which combines high-density sensing of electrochemical species with redox cycling amplification in the nanofluidic cavities, will be advantageous for electrochemical imaging methods and electrochemical biological assays. Particularly, one may expect that the detection or mapping of neurotransmitter secretion in neuronal networks will be one of the most interesting applications [13, 16, 89–96]. In this case, the sensor array is exposed to fast fluctuations in the neurotransmitter concentration. By biasing the two parallel sets of bar-electrodes to reducing and oxidizing potentials, one can then correlate the electrochemical signals at orthogonal electrodes, hence recording data from all sensors simultaneously (see Figure 5.6).

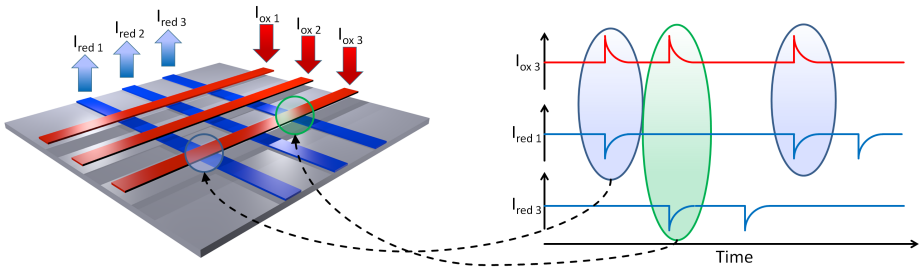

Figure 5.6: Electrochemical setup for parallel spike recording on-chip. By correlation of individual spike events at anodic and cathodic electrodes, all electrodes intersections can be read out simultaneously.

Chapter 6

Noise characteristics of redox-cycling sensors

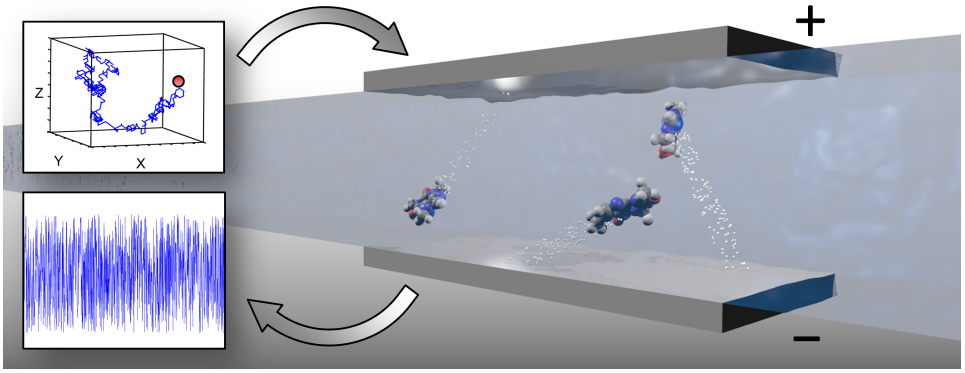

This chapter was reproduced in part with permission from "Enno Kätelhön, Kay J. Krause, Pradyumna S. Singh, Serge G. Lemay, and Bernhard Wolfrum. Noise characteristics of nano-scaled redox-cycling sensors: Investigations based on random walks. *Journal of the American Chemical Society*. 2013, 135, 8874-8881. DOI: 10.1021/ja3121313." Copyright 2013 American Chemical Society.

6.1 Preamble

This chapter investigates noise effects in nanoscaled electrochemical sensors using a three-dimensional simulation based on random walks. The presented approach allows the prediction of time-dependent signals and noise characteristics for redox cycling devices of arbitrary geometry. Simulation results closely match experimental data as well as theoretical expectations with regard to measured currents and noise power spectra. Furthermore, the impact of the sensor design on characteristics of the noise power spectrum is analyzed. Specific transitions between independent noise sources in the frequency domain are indicative of the sensor-reservoir coupling and can be used to identify stationary design features or time-dependent blocking mechanisms. Since the presented approach is highly flexible with regard to the implemented boundary conditions, it opens up the possibility for integrating a variety of surface-specific molecular reactions in arbitrary electrochemical systems. Thus, it may become a useful tool for the investigation of a wide range of noise effects in nanoelectrochemical sensors.

6.2 Introduction

Following the first description of interdigitated arrays in 1985 [34], the development and characterization of on-chip redox-cycling sensors has evolved to be an active field of research. Since then, a variety of sensor types and designs have been introduced and probed in a wide range of applications [17, 80, 97]. Described methods include interdigitated electrodes [35–37, 88, 98], pore-based approaches [47–53], and nano- and microcavity devices [19,20,56,57,61,87,99]. With respect to measurements involving only few molecules, nanocavity-based sensors represent one of the current methods of choice. Featuring sensitivity capable of resolving single-molecules [54] as well as a comparably simple fabrication process that is based on standard clean room technology, they have received growing attention during the last years. Typically, sensors consist of two micron-scaled electrodes that are separated by tens of nanometers and arranged parallel to each other and the wafer surface. The electrodes can be biased individually and are covered by a passivation layer, while access to the analyte is enabled via small connecting channels. In sensing applications, electrodes are biased to potentials below and above the redox potential of a redox-species under investigation. Molecules can then participate in subsequent oxidation and reduction

reactions and, hence, form a measurable current across the electrode gap.

Besides applicability for the detection of redox-active molecules, nanocavity sensors can also be used for spectroscopy applications. In 2009, Zevenbergen *et al.* introduced a novel spectroscopy approach called Electrochemical Correlation Spectroscopy (ECS) [55]. Analogous to Fluorescence Correlation Spectroscopy (FCS), here, the measured current noise is recorded and its time evolution [55] or amplitude [23] can be analyzed to gain insight into concentration fluctuations as well as adsorption and desorption dynamics of the analyte at the electrodes [55]. Since the electrochemical current of these sensors scales with the number of molecules N that are present in a given volume and statistical fluctuations scale with $\sqrt{N}$, noise-to-signal ratios are much improved when few active molecules are located inside the sensor. Due to the nanocavity sensors' ability to operate with ultra-low molecule numbers, they represent an ideal platform for noise spectroscopy.

In electrochemical fluctuation spectroscopy, investigations are so far mostly based on noise power spectral densities or autocorrelation descriptions that contain a wide range of information on the respective electrochemical and diffusive processes. However, in many cases, both methods represent a fingerprint of an electrochemical process rather than its full description. Parameters such as sensor design, adsorption- and desorption rates, inactivation of the analyte, and passivation of the electrodes may impact the resulting noise characteristics in multiple ways. Therefore, one may believe that, with regard to future applications, the technique of ECS can be further advanced by supporting simulations. The simulations may then take into account these diverse effects and determine their influence on the noise spectra, thus leading to a better understanding of the experimental data.

Diffusive processes are often modeled via means of finite element simulation software that is widely available. However, since finite element approaches are based on probability densities for the locations of analyte molecules, only averaged currents can be described, and the modeling of noise remains difficult. For relevance to noise spectroscopy, here, the simulations are based on stochastic random walks, which simulate every individual molecule's movement. Even though this approach leads to comparably high computational workloads, random walks continuously offer better modeling opportunities due to steady advances in computational power and parallelization. The model further mirrors real-life processes in a detailed, yet simple and demonstrative way. It is easily

extendable with regard to effects on the molecular scale, such as adhesion or deactivation of molecules. For these reasons, random walk simulations evolved to a commonly used approach during the last two decades. Successful applications include, the modeling of electron-transfer kinetics [100], single-molecule electrochemistry [81], diffusion controlled electrode processes [101–103], potential-step chronoamperometry [104], stochastic variations in molecule capturing times at electrodes [105], as well as generator-collector systems based micro-band electrodes [106, 107], plan-parallel dual disk microelectrodes [108], and inside concentric spherical electrochemical cells [109].

In a previously published work, a random walk simulation was applied to different geometries and two sources of noise were identified: Number Fluctuation Noise that results from the stochastically varying number of molecules in between the two electrodes and Redox Cycling Shot Noise, which occurs as a consequence of the diffusive shuttling of molecules in between the electrodes [110]. Based on this, this chapter provides a significantly more detailed analysis of the noise phenomena in redox-cycling sensors. Using an advanced random walk model based on Monte Carlo simulations in a cubic lattice, this chapter first discusses the accuracy of random walk simulations with regard to the ratio of device size and random walk step width and compares the simulation results to experimental data. Based on these results, series of simulations for different structure geometries is performed and key parameters for spectroscopic applications are considered.

6.3 Methods

The simulation model is based on three fundamental assumptions. First, redox active molecules perform stochastic random walks in accordance with the diffusion equation and are reflected upon collisions with boundaries. Second, each molecule can adopt two different oxidation states, namely the reduced and the oxidized state. Further, molecules change their oxidation state instantly whenever they touch an appropriately biased electrode, i.e. if an oxidized molecule is reflected at a cathode, it changes its state to 'reduced'. A reduced molecule only changes its state at an anode and oxidized molecules that hit an anode or reduced molecules that hit a cathode do not react. This implies the approximation that the plane of electron transfer (PET) equals the electrode surface. Typically, PET and electrode surface are separated by 1 nm, which is below the

accuracy that usually can be reached in the fabrication of the channel height in nanocavity sensors. Third, redox active molecules do not interact with each other and the electric field of the electrodes. Since nanocavity redox cycling experiments are typically performed at high electrolyte concentrations to ensure a good reference potential throughout the nanofluidic, the Debye length is less than one nm for most experimental conditions.

The software is implemented as follows: The simulation is written in C++ and compiled via the GNU Compiler Collection (GCC). Random walks are calculated independently on all available CPUs, while parallel computing is achieved through the application programming interface (API) Open Multi-Processing (OpenMP). During the random walk, each molecule is virtually displaced in time intervals dt by a pseudo random vector of the length dr. This vector is calculated from three pseudo random numbers that are obtained via routines taken from the GNU Scientific Library, namely the algorithm mt19937 that is based on the Mersenne Twister code [111]. Hereby, the time dt and the length dr fulfill the following equation that can be derived from the three-dimensional diffusion equation:

$$dr = \sqrt{6Ddt}. \tag{6.1}$$

At every step, each Cartesian coordinate of a molecule is either increased or decreased by the fixed distance $dr' = dr/\sqrt{3}$. Molecules further move on a static grid, while virtual boundaries are always placed in between two neighboring grid points.

When calculating the random walks, the software processes and records three data traces: The number of reactions at the oxidizing and the reducing electrode (1 and 2) that occur within a predefined sampling interval dT and the average number of redox molecules that are located in between the redox electrodes during the same time (3). Data is then stored in an ASCII file and later processed using the numeric computing environment Matlab.

If not indicated separately, all simulations employ diffusion constants D of 10^{-9} m^2/s, a virtual sampling rate of 10 kHz, and a spatial step width of 2 nm for the simulated current traces, which exceeds the chosen temporal resolutions of the random walks by orders of magnitude.

6.4 Results and discussion

6.4.1 Applicability of random walks to the nano-scale

In open space, diffusive processes can be easily modeled via stochastic random walks. As long as the step width is kept constant and the spatiotemporal displacement is modeled according to the diffusion equation (see Formula 6.1), the simulation is mathematically identical to the analytical solution and results can directly be used without further processing. However, the design of simulations becomes more challenging, if the space available for diffusion is limited by boundaries. In a random walk simulation, the displacement of each molecule is virtually triggered at a fixed rate $1/dt$. Hence, the actual molecule pathway is reduced to a linear movement between a defined start- and end position, while all intermediate positions are neglected. Potential collisions at boundaries cannot be considered in such a model. Therefore, any type of boundary condition may impact the simulation results in multiple ways, depending on the simulated geometry and the reflection algorithm chosen.

In order to quantify the impact of this effect on the simulations, a simple geometry is chosen for a parameter screening: A model of two infinite parallel plates that represent electrodes biased for redox cycling (See Figure 6.1a). A set of 80 active molecules at random oxidation states is released uniformly distributed between the electrodes. The electrode response is then recorded for a time interval of 0.1 s. The simulation is repeated several times with varied step widths and the average current is individually determined for each repetition. Simulation results can then be compared to an analytical solution for the average current that can be derived from the one-dimensional diffusion equation: On average, the transmission of one molecule's redox charge load from one electrode to the other requires twice the time T_{trans}, it takes for a molecule to diffusively travel the distance h between the electrodes. Analogous to equation 6.1, in the one-dimensional case this time can be calculated as follows:

$$T_{trans} = \frac{h^2}{2D}. \tag{6.2}$$

Hence, the average current per redox-active molecule in between the electrodes is given by:

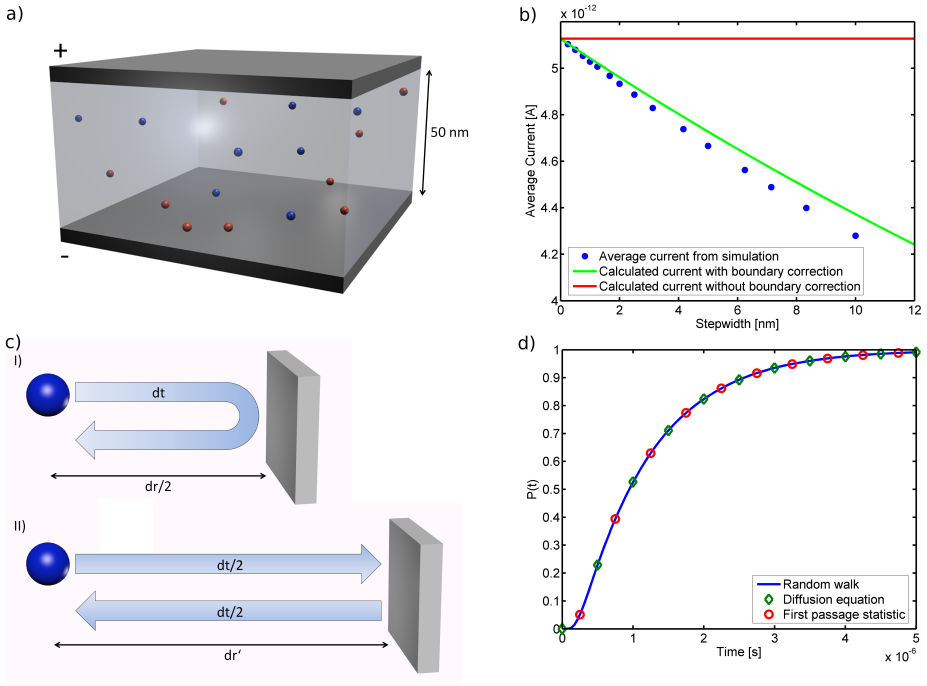

Figure 6.1: a) Simple model for the isolated investigation of the redox cycling effect. The sensor consists of two infinite parallel electrodes separated by a nano-scaled gap. b) Average simulated currents of a sensor consisting of two infinite parallel electrodes at a distance of 50 nm. The red graph represents the theoretical result, the blue graph shows the simulated average current at one electrode, and the green graph shows the corrected current according to Formula 6.7. The random walk simulation used 80 molecules and the charge transfer per reaction amounts to the elementary charge. c) Two reflection models: I) Pathway of a single step dr at a simple reflecting boundary within the time interval dt. II) Corrected boundary position according to diffusion equation. The random walk is subdivided into two steps of the spatial step width dr' and the temporal step width $dt/2$. d) Cumulated reaction probability of a molecule that is located in between two parallel absorbing boundaries that are separated by a distance of 100 nm. The molecule is released centrally at the time $t = 0$. The probability was calculated in three different ways.

$$I_{Molecule} = \frac{Dq_{molecule}}{h^2}, \tag{6.3}$$

where $q_{molecule}$ represents the charge that can be exchanged by one molecule [18, 19].

The result of this model can be seen in Figure 6.1b, which compares the theoretically calculated current with the values obtained from simulations that use various step widths. In the plot one can find an increasing underestimation of the simulated current at higher step widths, which relates to the discrete nature of the random walk approach that disregards intermediate positions of a molecule's trajectory in between two subsequent positions in the simulation. One effect is particularly relevant for the simulation of nano-electrochemical effects: Whenever a molecule is located in immediate proximity to a reflecting boundary and follows a reflected pathway (as seen in see Figure 6.1c, (I)), the molecule's distance to the boundary is underestimated. During this time interval dt, the molecule first approaches the electrodes, while passing the distance $dr/2$. Then it is reflected and again passes the distance $dr/2$ back towards its initial position. However, since the molecule's diffusive pathway is not linear in time, the reflection has to be treated as two individual steps that are performed within the interval dt and that feature a different spatial step width dr', see Figure 6.1c, (II). Based on the one dimensional diffusion equation,

$$dr_{1D} = \sqrt{2Ddt} \tag{6.4}$$

we can calculate the length of dr' as follows:

$$dt = \frac{dr_{1D}^2}{2D} = \frac{2dr'^2_{1D}}{2D}. \tag{6.5}$$

This leads to an expression for dr':

$$dr'^{1D} = \frac{dr_{1D}}{2}. \tag{6.6}$$

We can now calculate an effective distance h' between the two electrodes that is corrected for the discrepancy in the step size at both boundaries:

$$h' = h - 2\frac{dr_{1D}}{2} + 2dr'_{1D} = h + (\sqrt{2} - 1)dr_{1D}. \tag{6.7}$$

Based on this formula and equation 6.3, we can calculate the deviation in

the simulated current that is caused by this effect. The so-predicted current explains most deviations caused by the discrete nature of the random walk, as illustrated in Figure 6.1b. In the following, however, all simulated currents are corrected according to the deviation that was measured between the simulated data and the theoretical value that was found via equation 6.3.

In conclusion, by running the simulation that is sketched in Figure 6.1a, it is shown that the average value of T_{Trans} in the simulation closely matches the theoretical value at small step widths and that one can correct the simulation results in case of longer step widths. However, its statistical distribution has not been validated, yet. Therefore, a second, slightly modified simulation is run in order to confirm the statistical distribution of T_{Trans}: 170,000 molecules are released centered in between the electrodes, while the time interval until they hit one of the electrodes for the first time is recorded. Out of this data, the accumulated reaction probability as a function of the time since the molecules release is calculated. These results are compared to two analytical solutions: First, the reaction rate can be addressed via the general solution of the one-dimensional diffusion equation, see Formula 6.4. More generally, the latter can be written as the spacial probability density of finding a molecule at the time t after its release at the point x_0:

$$p_0(t, x, x_0) = \frac{1}{\sqrt{4\pi D t}} e^{-\frac{(x-x_0)^2}{4Dt}}. \tag{6.8}$$

Here, the method of images to approximate the reaction probability as a function of time is employed. The molecule is hereby released at x=0 and the boundaries are located at the positions 50 nm and -50 nm. In order to approximate the boundary condition c(x=-50 nm) = c(x=50 nm) = 0, Formula 6.8 is super-positioned with alternating signs at multiples of 100 nm, starting from -800 nm to 800 nm. Hence, we obtain:

$$P(t) = 1 - \int_{-50nm}^{50nm} dx \sum_{i=-4}^{4} (-1)^i p_0(t, x, x_0 = i * 100nm). \tag{6.9}$$

Second, a discrete analytical approach is chosen based on the Gambler's Ruin problem that was previously introduced by Zevenbergen *et al.* to describe the first passage of molecules in a 1-dimensional nanofluidic channel [20]. In this context, the model describes the absorption probability $P(n)$ of a random walker that is released centrally in between two absorbing boundaries. Hereby,

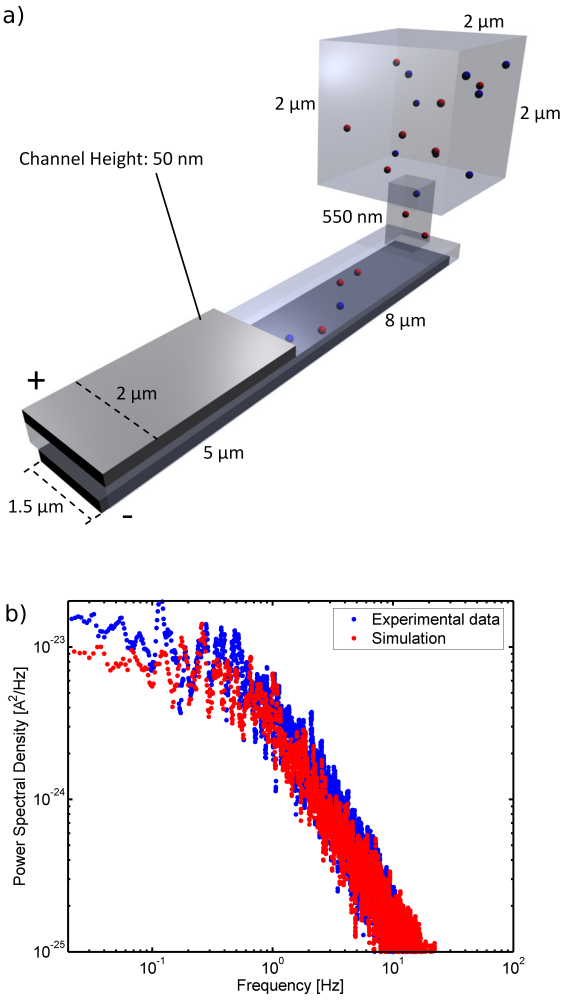

Figure 6.2: a) Sketch of the model that is used for simulation in order to compare simulated to experimental data. The sensor consists of two parallel electrodes separated by a nanocavity. Access to a small bulk reservoir is enabled via an access channel at the end of the nanocavity. b) Power spectral densities obtained from simulation (red) and experiment (blue). Our simulation uses 200 individual random walks and a diffusion constant of 0.67 * 10^{-9} m^2/s. The temporal step width is 10^{-7} s and the sampling interval is 2 ms. Data was filtered using a moving average filter.

n describes the number of steps that the molecule performed since its release and a is the distance between the two boundaries in steps.

$$P(n,a) = \frac{2}{a}\sum_{v=1}^{a-1} cos^{n-1}\frac{\pi v}{a} sin\frac{\pi v}{a} sin\frac{\pi v}{2}. \tag{6.10}$$

As can be seen in Figure 6.1d, all three models are in close agreement. Hence, the simulation offers good applicability for the modeling of statistical processes.

6.4.2 Comparison simulation and experiment

In order to validate the model, the simulations are compared with experimentally obtained data. Here, a nanofluidic device that was described by Zevenbergen *et al.* in 2009 [56] was used. In short, this device features a nano channel (26 μm x 1.5 μm x 50 nm) and two Pt electrodes that are located centrally on top and below the nano channel and overlap in an area of 10 μm x 1.5 μm. The sensor further has two access channels (1 μm x 1 μm x 550 nm) at either end that provide diffusive access from the bulk reservoir to the nano channel. Measurements were performed in a 50 μM $Fc(MeOH)_2$ solution after functionalizing the electrodes with 3-mercaptopropionic acid (3-MPA). Exact parameters of this experiment have been described elsewhere [23]; detailed information on the data processing can be found in Appendix B. The design used in the simulation can be found in Figure 6.2a. It is based on the symmetry of the real-life sensor design; however, a simplification is introduced: the system's symmetry is used and only one half of the sensor is implemented. Since molecules do not interact with each other and reflect at the intersecting plane, this system is identical to the experiment as long as the concentration is doubled.

As it will be shown later, the amplitude of the power spectral density at low frequencies scales linearly with number of molecules inside the sensor. Since the number of molecules involved in the experiment exceeds the number of molecules that can be simulated in reasonable time on the system employed, one can utilize this linear relationship in order to derive data that matches the experimental parameters from a simulation that uses fewer molecules. When doing so, first the number of molecules that contribute to the experimentally obtained current is calculated by dividing the average measured current by the theoretical current contribution of a single molecule (see Formula 6.3). By this means, one can estimate the average number of molecules inside the sensor to approximately 19.760 and scale the amplitude of the simulated power spectral density accordingly. Furthermore, the deviation caused by adsorption effects was corrected. These effects generally lead to a rescaling of the frequency axis by a constant factor in the power spectral density, while the magnitude of the shift is known from literature [23, 55]. In short, adsorption inside the nanochannel slows down the average speed of the active molecules' diffusive movement along the channel, leading to an effective diffusion constant that is smaller than the diffusion constant in bulk solution. For the current design, the frequency axis is scaled by a factor of 0.5 according to the calculations by Singh *et al.* [23].

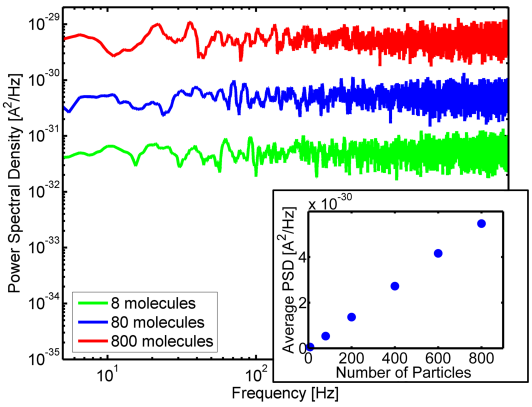

Figure 6.3: Top: Simulated power spectral densities of the currents in the parallel plates model. The pictured simulations use 8, 80, and 800 molecules (green, blue, red) and the data is filtered using a moving average filter. Bottom: Average values of each power spectral density (PSD) as a function of the number of molecules inside the sensor.

Figure 6.2b shows the so obtained simulated data together with recordings from the experiment. As it can be seen in the figure, the simulation closely reproduces the experiment.

6.4.3 Investigations of noise spectra

As mentioned previously, nanocavity sensors exhibit two intrinsic types of noise that result from different sources: The molecules shuttling between the electrodes and the molecules entering and leaving the sensor's detection region. In the following, both effects are threated separately first and various parameter dependencies are investigated. Later the full spectrum of a typical nanocavity sensor is modeled.

6.4.4 Redox-cycling shot noise

Redox-cycling shot noise results from the thermal motion of redox-active molecules inside the sensor. Since molecules shuttle diffusively in between the electrodes, the measured overall current across the gap always depends on the individual trajectories of all molecules. As each trajectory is stochastic, the measured current is also subject to stochastic fluctuations. In order to quantize their impact on the spectra, the power spectral density of a varied number of molecules in the above mentioned parallel-plates geometry is simulated (see Figure 6.1a). Since the number of molecules inside the sensor is held constant in this model, the obtained noise is exclusively caused by redox cycling shot noise; noise from concentration fluctuations cannot occur. The corresponding power spectral

densities can be seen in Figure 6.3.

The figure demonstrates that, as expected for the relatively low frequencies investigated here [110], the redox-cycling shot noise exhibits a white noise characteristic, i.e. the noise power at a certain frequency is independent of the frequency itself. This white noise characteristic is also independent from the number of molecules inside the sensor; however, the amplitude of the noise power varies with the concentration. As it can be seen in the inset, the average values of the power spectral densities scale linearly with the number of molecules inside the sensor. This result is in line with theoretical considerations: In molecular processes that are dominated by Poisson statistics, fluctuations generally scale with the square root of the number molecules involved. Hence, their power scales linearly with the number of molecules.

In the context of the spectroscopy methods described below, redox cycling shot noise contributes one characteristic number: The average power spectral density S_1 of the white noise spectra, which both depends on the number of particles N inside the sensor and scales with h^{-2}, as previously shown in Equation (3). Due to its dependency on N, the contribution of this type of noise is small at low concentrations and, hence, difficult to observe in measurements like in single-molecule detection [81]. However, the magnitude of redox-cycling shot noise increases at higher concentrations and larger electrode surfaces as can be seen in Figure 6.3.

6.4.5 Number fluctuation noise

In addition to redox cycling shot noise, nanocavity redox cycling devices exhibit another type of noise that results from fluctuations in the number of molecules inside the sensor [23, 55]. Due to the sensors strong amplification of the individual Faradaic currents caused by each single molecule, small statistical fluctuations in the number of analyte molecules cause a significant part of the overall noise on the current.

For quantization of the noise character that results from this effect, a design similar to the real-life redox-cycling sensors in the simulation model is implemented [57]. The simulated design features two circular electrodes that are 15 μm wide and located in parallel to each other. They are separated by a 50 nm wide cavity of the same lateral size. The setup is integrated into an 850 nm thick passivation layer that is interpenetrated by a circular access channel, centrally with regard to the electrodes positions. Furthermore, a cylindrical bulk

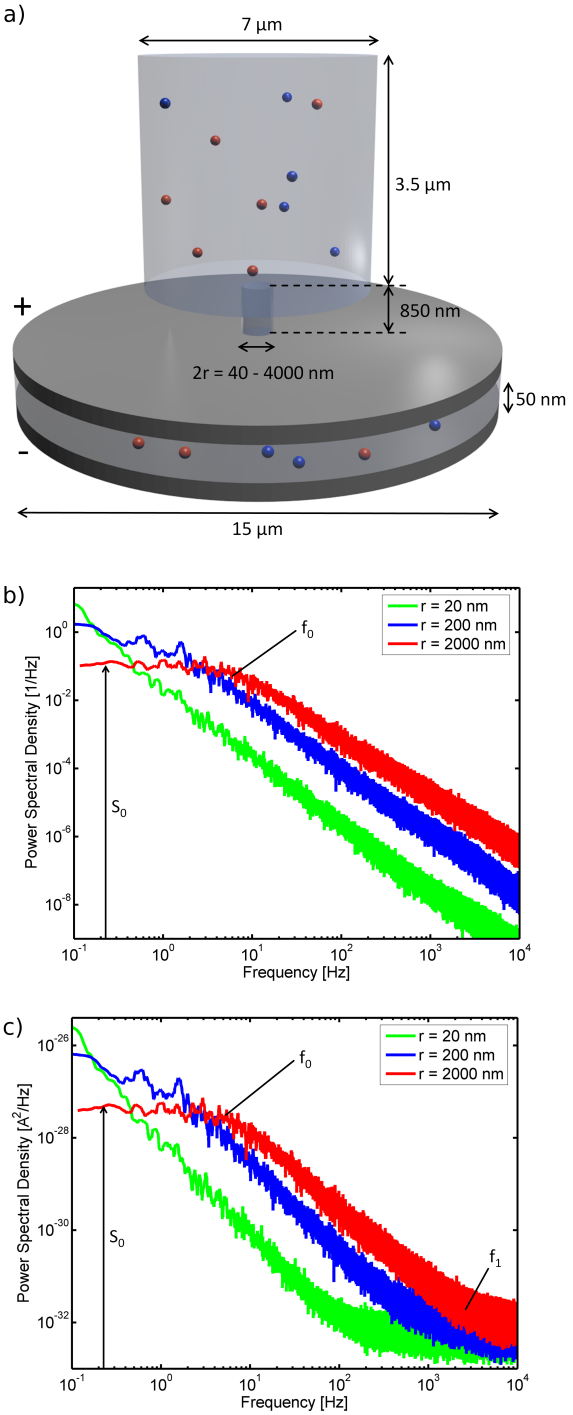

Figure 6.4: a) Sketch of the model that is used to investigate the number fluctuation noise. The sensor consists of two parallel electrodes separated by a nanocavity. Access to a small bulk reservoir is enabled via an access channel that interpenetrates the top electrode. b) Power spectral density of the number of molecules between the electrodes at different sensor openings. This corresponds to the spectral density of the number fluctuation noise alone. The simulation was calculated for radii of 20 nm (green), 200 nm (blue), and 2000 nm (red). The traces magnitude was normalized to an average of one molecule inside the sensor. The model uses 80 molecules and data was filtered using a moving average filter. c) Power spectral density of the simulated current for different radii of the sensor opening. This includes both shot noise and number fluctuation noise. The crossover from between which of these sources of noise is dominant is indated by the label f1. Parameters match the ones chosen in Figure 4b.

reservoir is added to the system centrally at the opening of the access channel, see Figure 6.4a.

Since the overall electrode current is always affected by both noise sources - the redox cycling shot noise and the diffusion number fluctuation noise - , additionally, the average number of molecules that are located in between the electrodes within each sampling interval is recorded. By analyzing this additional trace, one can investigate the impact of fluctuations in the number of molecules inside the sensor separately from the redox cycling shot noise. Assuming the system under investigation remains in a state of equilibrium, the character of these fluctuations depends on only two factors: The nature of the analyte molecules' diffusive movement and the geometry of the sensor. In particular, the geometry of the space that is enclosed by the electrodes and its connection to the bulk reservoir play an important role. In the simulations, the impact of this design feature is probed by varying the diameter of the sensor access channel to the bulk reservoir. By this means, the overall surface area of this diffusive link to the nanocavity is varied. Plots showing the power spectral densities of the number of molecules that were obtained at varied surface areas of the diffusive interconnection between the space enclosed by the electrodes and the other parts of the sensor can be found in Figure 6.4b.

In the plot, we can find a characteristic feature that was formerly described by Zevenbergen *et al.* and *Singh et al.* [23,55]. The graphs show a flat plateau in the low frequency regime, which spreads up to a transition frequency f_0. Above this frequency the power spectral density drops according to a power law, which can be seen by the linear trace in the logarithmic plot. Furthermore, one can find that the level of the noise S_0 at the plateau decreases with the diameter of the sensor opening, while f_0 moves to lower frequencies. Besides this offset in frequency and level, the shape of the power spectral density remains unchanged by the variation of the coupling between the sensor and the reservoir. Neither is the character of the power law drop above the transition frequency f_0 affected.

For spectroscopy applications, one can make use of the fact that both f_0 and S_0 are dependent on this design feature. Hence one can employ the average value S_0 of the low frequency plateau as well as the frequency f_0 for the specification of the diffusive connection between the inter-electrode area and the bulk reservoir in this idealized model.

6.4.6 Current Noise in Nanocavity Sensors

The sensor's current is subject to both sources of noise, the redox cycling shot noise and the number fluctuation noise. This can be seen in the plot of the power spectral densities from the current traces (see Figure 6.4c).

The plot illustrates that the low frequency domain is fully dominated by the number fluctuation noise. As it can be expected from Figure 6.3, the redox cycling shot noise in this regime is too small to significantly contribute to the current noise. However, since the fluctuation concentration noise drops with a power law at higher frequencies, there is another, second transition frequency f_1 that occurs at the frequency, at which the magnitude of the fluctuation concentration noise drops below the level of the white noise spectra of the redox cycling shot noise. Hence, the noise spectra of the current can be considered to be a sum of the two other noise sources: redox cycling shot noise and number fluctuation noise. The two characteristic values S_0 and S_1 can be found in the graph and be used as reference values for spectroscopic applications. Furthermore, the value f_1 of the second transition frequency can be obtained from the simulation. This value can be used to determine the ratio of the impacts of the two noise sources. Since the magnitudes of both noise sources scale equally with the number of molecules n in the system and, thus the analyte concentration, f_1 provides a direct measure for the sensor's diffusive access to the bulk reservoir, which is independent from the concentration and only requires the knowledge of the inter electrode distance h.

Potential applications can be found particularly for gated redox currents [112] with nanoporous devices. Since f_1 strongly depends on the size of the connecting channel and increases with its diameter, devices that feature only small connecting channels between the active area of the sensor and the bulk reservoir are best suited to avoid exceeding the measurable frequency range. Furthermore, when this requirement is met, changes in the diffusive coupling between the sensor and the bulk reservoir are reflected in the sensor noise. Hence, sensing approaches that can measure blocking of the sensor's access channels - for example via an antibody-antigen interaction or a chemical modification of the channel's surface - can be based on this spectroscopy method.

6.5 Conclusions

This chapter presents a simulation framework for the noise characteristics of nanocavity redox cycling sensors. First, the applicability of these simulations by comparison to theoretical results is discussed and the impact of the step width used in the simulation on the result is quantified. Then, the simulation is compared to experimental data and demonstrates the applicability to modeling real-life sensors. The last part of this work focuses on the two characteristic sources of noise, redox cycling shot noise and number fluctuation noise. Here, the dependency of redox cycling shot noise on the system's parameters is described. Then the main characteristics of noise caused by concentration fluctuations in a nanofluidic sensor are reproduced. Furthermore, the impact of variations in the connection of the sensor to the bulk reservoir on the noise spectrum is analyzed and it is found that the number fluctuation noise level in the low frequency regime scales inversely with the diffusive access to the bulk reservoir. Both sources of noise are present in electrochemical current noise, where the number fluctuation noise dominates the low frequency regime and redox cycling shot noise dominates the higher frequencies. Since only the number fluctuation noise is affected by the strength of the diffusive coupling to an external reservoir, one can utilize the transition frequency to determine this coupling parameter.

Based on simple model assumptions, random walk simulations offer a fast and easy option to obtain noise power spectral densities of complex sensor designs that are difficult to attain otherwise. Due to the model's simple structure, it can be easily extended towards other effects like adsorption or electrode passivation and, hence, offer an insight into more complex spectroscopy methods for future applications.

Chapter 7

Noise phenomena caused by adsorption

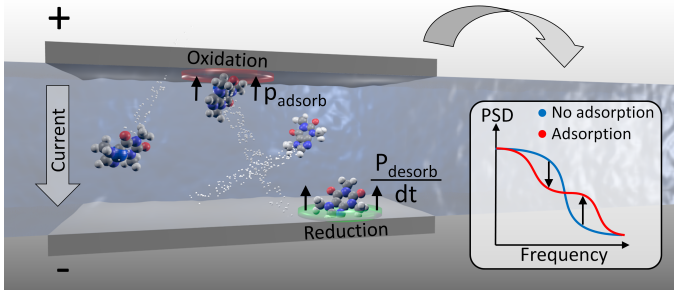

This chapter was reproduced in part from the unpublished work "Enno Kätelhön, Kay J. Krause, Klaus Mathwig, Serge G. Lemay, and Bernhard Wolfrum. Noise phenomena caused by reversible adsorption in nano-scaled electrochemical devices" (in preparation).

7.1 Preamble

This chapter investigates reversible adsorption in electrochemical devices on a molecular level. To this end, a computational framework is introduced, which is based on three-dimensional random walks including probabilities for adsorption and desorption events. It is demonstrated that this approach can be used to investigate adsorption phenomena in electrochemical sensors by analyzing experimental noise spectra of a nanofluidic redox cycling device exposed to ferrocene dimethanol. The evaluation of simulated and experimental results reveals an upper limit for the average adsorption time of the redox-active molecules of 200 μs. The model is applied to predict current noise spectra of further electrochemical experiments based on interdigitated arrays (IDAs) and scanning electrochemical microscopy (SECM). Since the spectra strongly depend on the molecular adsorption characteristics of the detected analyte one can suggest key indicators for revealing adsorption phenomena in noise spectroscopy depending on the geometric aspect of the experimental setup. For this application, sensors can be easily implemented with the presented software.

7.2 Introduction

Adsorption phenomena may impact the performance of electrochemical devices in multiple ways and play a crucial role in the development of nano-scaled sensors. Particularly, the reversible or permanent adsorption of analyte molecules at sensing electrodes turns out to be of increasing importance at small scales, where analyte transport towards the electrode is accelerated through spherical diffusion profiles. The same applies to experiments involving repeated analyte reactions in fast-scan voltammetry [113,114] or redox cycling. In the latter case, similar to nanoelectrode experiments, the analyte mass transfer towards the electrode is enhanced, enabling significantly higher reaction rates at the surface as well as an increased impact of adsorption effects. In redox cycling devices, the ratio between electrode surface and enclosed volume is typically very high ($>10^7$ m^{-1}) representing a good system for the investigation of adsorption phenomena. Such devices can be implemented in a variety of different designs [17, 80], but always comprise two individually biased electrodes that are located in close proximity to each other. In this setup, analyte molecules can diffuse in between the electrodes and participate in repeated redox-reactions while establishing a

current across the gap. Due to the increased reaction rate at the electrodes, this effect leads to a significant amplification of the Faradaic current and represents the central advantage of the redox cycling approach.

Most reported experiments utilize the redox-cycling effect in two types of setups and devices, namely scanning electrochemical microscopes (SECM) and interdigitated electrodes (IDEs). The first group of SECM setups typically comprises arrangements, in which an ultra-microelectrode scans across a sample surface [31]. During this process, electrode and parts of the substrate can be biased to opposing potentials while redox cycling is enabled [115]. Today the method of SECM is an established method and applied in a variety of different fields of research [116–119]. The second group, IDEs, feature two comb-shaped electrodes that arranged in an interdigitated fashion on a substrate surface [34,36,42,120]. Due to their comparably simple fabrication and lab-on-a-chip integration, IDEs are today used in a wide range of applications [39,59,84,121]. Other on-chip approaches include pore-based sensors [47,50,52,122] that are formed through an interpenetrated electrode stack. Furthermore, precisely overlapping electrode faces can be implemented in nanofluidic or nanocavity sensors by removing a sacrificial chromium layer in between two closely-spaced electrodes [19, 57]. Such devices will be addressed first in this chapter.

Even though redox cycling sensors are widely used, there are only few publications that focus on their noise characteristics. Most of these studies investigate the fluctuation of the Faradaic current or the stochastic sensing of single molecules in either SECM experiments [18,123] or nanofluidic devices [54,79,81]. Other studies analyze the origin of different types of noise that can be found in the current response of nanofluidic sensors [23, 55, 110, 124] and will be set in relation to this work below.

In this chapter, the work on the simulation of noise phenomena [124] that was presented in the previous chapter is expanded by investigating the impact of molecular adsorption on the noise spectra of redox cycling sensors. Hereby, it is first shown that the simulation model reproduces theoretical expectations in simple geometries. Then the approach is taken a step further and the spectrum of a nanofluidic electrochemical sensor is simulated. Experimental data is compared with simulated spectra and closely matches its results. The analysis yields an upper boundary for the average adsorption times of redox active molecules. In the last part of this chapter, the model is applied to more complex geometries that cannot be easily solved analytically. Noise spectra of adsorbing

interdigitated arrays as well as of an absorbing scanning electrochemical microscope (SECM) tip nearby a biased conducting surface are predicted. Hereby, the simulations reveal new applications in noise spectroscopy predicting discrete boundaries for observing adsorption times.

7.3 Methods

7.3.1 Simulation framework

This chapter employs an approach that is based on the previously described computational framework [124]. In short, active molecules' Brownian movements are modeled though individual random walks that comply with the diffusion equation, while molecular pathways are mirrored upon collisions at boundaries. Active molecules can further adopt two oxidation states and participate in redox reactions whenever they touch an appropriately biased electrode.

Here, the model is expanded by a model of adsorption: during the random walk, molecules can adsorb in collisions at electrode surfaces with a fixed probability p_a. This definition of p_a does not represent the adsorption probability of a real molecule but is directly linked to it. In an actual experiment, the mean free pathway of a diffusing molecule is much smaller than the maximal resolution employed computers can model in a reasonable time. Therefore, p_a has to be considered as the average molecular adsorption probability within the temporal random walk step width dt, while the respective molecule is located in a cubic space at the electrode that features an edge length dx equaling the one-dimensional step width of the random walk. The resulting adsorption rate k_a is therefore a function of the random walk step width and p_a. Since the random walk resolution is usually limited by the employed computers computational power, pa can be adjusted to match realistic reaction rates. At a given step width p_a can then be calculated from the desired reaction rate k_a

$$k_a = \frac{p_a}{2}\frac{dx}{dt} \tag{7.1}$$

The product $k_a c_{bulk} A$ then provides the rate of the absolute number of adsorbing molecules, where c_{bulk} is the bulk concentration of molecules and A the electrode surface. After each temporal step of the random walk, adsorbed molecules can desorb again with the probability p_d. The distribution of the molecules' residence times then follows the geometrical distribution. The prob-

ability of detachment after the nth step for $n > 1$ is given by $p_{detach}(n) = (1 - pd)n - 1pd$. It features an average residence time τ_a of

$$\tau_a = \frac{dt}{p_d} \tag{7.2}$$

where dt represents the temporal step width of the random walk. This approach resembles the common model of an adsorbed molecule that oscillates due to its thermal energy and hits an energy barrier at the frequency of its oscillations. However, due to the available computing capacity dt has to be chosen to be significantly higher. Therefore, p_d represents the total desorption probability of all desorption attempts a molecule performs within dt, while the resulting desorption rate is again linked to the random walk parameters. In order to derive this reaction rate, we have to consider the discrete nature of the random walk, which does not allow surface concentrations but limits the analysis to volume concentrations. The volume concentration at the electrode surface therefore has to be converted into a surface concentration by division through dx. The rate of desorption is then given by

$$k_d = \frac{1}{\tau_d} = \frac{p_d}{dt} \tag{7.3}$$

Here, the product $k_d c_{surface} A$ provides the rate of the absolute number of molecules being released, where $c_{surface}$ is the surface concentration.

In most redox cycling experiments, the average adsorption and desorption times are unknown. However, If the employed device features two fully overlapping parallel electrodes that are separated by the distance h, this ratio can be calculated from the currents variance [23]. For this reason, the ratio of adsorption and desorption times as a function of the simulation parameters is often helpful. If we combine equation (1) and (3), we obtain

$$\frac{\tau_a}{\tau_d} = \frac{p_a}{p_d} \frac{dx}{h}. \tag{7.4}$$

7.3.2 Simulation parameters

In all simulations, the lateral step width of the random walk is chosen significantly smaller than the smallest design features. Detailed parameters for all simulations can be found in the tabular in Appendix B.

7.3.3 Experimental methods

The fabrication of the devices has been reported in a previous publication [125]. 20 μM 1,1-ferrocene dimethanol was prepared in Milli-Q water using 1 mM KCl as a background electrolyte. Both chemicals were acquired from Sigma-Aldrich. The presented data is an average of ten measurements.

7.4 Theory

In former studies, three origins of current noise have been described for nanofluidic redox cycling sensors. These are namely number fluctuation noise, adsorption noise and, shot-like redox cycling noise. In the following, their nature will be shortly discussed and the introduced adsorption model will be set in relation to the current state of research.

7.4.1 Number fluctuation noise

Number fluctuation noise results from active molecules that diffusively enter and leave the sensor. The change in number of molecules inside the sensor then also leads to fluctuations in the number of molecules that participate in redox-cycling and causes a certain type of noise in the low frequency regime that can be described analytically [20, 55]. For the case of adsorbing electrodes, an effective diffusion constant D_{eff} can be assumed inside the channel that reduces the speed of the fluctuation noise, while spectra's shape is preserved [23, 55]. D_{eff} can hereby be determined either from the variance of a current trace or through a spectral analysis, and turns out to be a convenient measure to determine the ratio between average adsorbed and desorbed times. This idea can also be found in the simulation approach. Due to adsorption at electrodes, the diffusion constant along the nanochannel is effectively lowered, since molecules reversibly adsorb after an average free time while diffusion is halted. The effective diffusion constant in between two electrodes of a nanofluidic sensor is then given by

$$D_{eff} = D\frac{1}{1+\frac{\tau_a}{\tau_d}} \tag{7.5}$$

where τ_d and τ_a represent the average time a molecule diffuses freely and spend adsorbed, respectively [55]. However, in contrast to the above mentioned analytical model, the effective speed of diffusion in the model is not

assumed to be homogeneous but may vary inside the nanochannel. It depends on whether the molecule is enclosed between two electrode, one electrode and a non-conducting surface or two non-conducting surfaces and the device geometry. Our model can therefore be used for arbitrary designs without the need of defining area-specific diffusion constants.

7.4.2 Adsorption noise

In contrast to fluctuation noise, adsorption noise impacts the number of molecules participating in redox-cycling through reversible adsorption at the electrodes. Analytically, this process can be described through a two-state Markov process [55], in which molecules either participate in redox cycling and contribute a certain current to the overall sensor current or they are adsorbed. In the case of an ideal nanofluidic channel, this model is closely resembled by the simulation. Therefore, analytical findings can then be directly transferred to verify the simulation approach.

7.4.3 Shot-like redox cycling noise

Shot-like redox cycling noise is caused by the Brownian motion of active molecules in between the electrodes and depends solely on the average number of free molecules inside the sensor and the inter electrode distance [124]. The here introduced adsorption model, however, does not impact shot-like redox cycling noise since the average number of free molecules at a given bulk concentration is not influenced by the chosen adsorption model.

7.5 Results and discussion

7.5.1 Adsorption noise

In order to first study adsorption noise isolated from number fluctuation noise, the investigations start using a simple redox cycling system that solely consists of two infinite parallel electrodes, see Figure 7.1a. Here, the number of molecules remains constant throughout the experiment. The resulting current is therefore only affected by adsorption noise and shot-like redox cycling noise.

Figure 7.1b presents the simulated power spectral densities in comparison to the analytical solution. In case of adsorbing electrodes, graphs are calculated for different average adsorption times τ_a while the ratio between adsorbed and

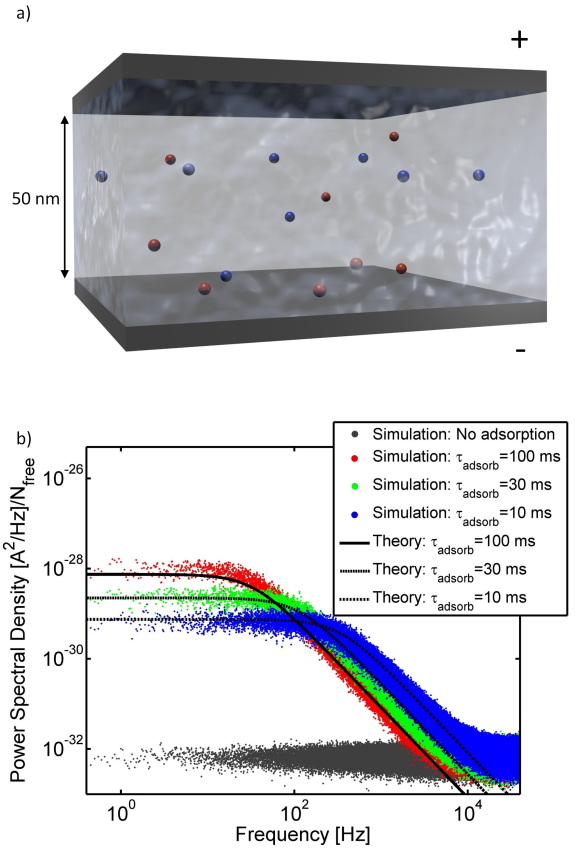

Figure 7.1: Simulations based on a parallel plates model that is used to investigate the adsorption and shot-like redox cycling noise separately from number fluctuation noise. a) Illustration of the model. b) Simulated power spectral densities in comparison to the analytical model. Differently colored graphs represent different average adsorption times. The power spectral density is normalized to a single free molecule. More detailed parameters can be found in Appendix B.

desorbed molecules remains constant. Spectra are further normalized to a single free molecule in between the electrodes. For disabled adsorption, we obtain the expected white spectrum of shot-like redox cycling noise that was previously described [124]. With an increase in τ_a, however, we find a growing plateau in the low frequency regime that spreads up to a transition frequency f_{trans}. This transition frequency decreases with an increase in τ_a. Above f_{trans}, we find a decrease according to $1/f^2$ until a second transition frequency, above which the spectra is dominated by shot-like redox cycling noise. Overall, we find a close agreement between the simulated power spectra and the analytical solution [55].

7.5.2 Modeling nanofluidic redox cycling sensors

In order to validate the simulation model, results are compared to experimental data. In the previous chapter, the simulation did not consider any adsorption effects and had to be analytically compensated for the impact of adsorption

by processing the simulation data according to Singh *et al.* [23]. This required a rescaling of the frequency axis to model the shift in the effective diffusion constant. In contrast to that, the improved simulation framework is capable of modeling the full sensor response solely based on adsorption modeled on the molecular level. This enables the application of the simulation to almost arbitrary designs on the one hand, and the direct modeling of noise effects that result from molecular properties on the other. The latter aspect further allows deriving molecular properties from noise spectra as it is shown below.

For the experiments, a nanofluidic redox cycling device is used. It features a nanofluidic channel of 10 μm length, 5 μm width, and 60 nm height. The channel has access to the bulk reservoir via two 2 x 4 μm wide access channels in the passivation and electrodes overlap in an area of 30 μm^2. Since the sensor exhibits symmetry with respect to the longitudinal cross section, one can model half of the device at doubled analyte concentration to increase computational efficiency, see Figure 7.22a.

Figure 2b presents simulated data for various adsorption times in comparison to experimental data. Similar to data shown in Figure 7.1b, we find that the transition frequency f_{trans} increases with a decrease in the average adsorption time τ_a. Additionally, the height of the plateau that spreads up to f_{trans} decreases with τ_a until adsorption noise is fully dominated by the fluctuation noise of the sensor. In this case of small τ_a, the simulated spectrum closely matches the experimental data, which allows us to draw first conclusions regarding τ_a. Since the adsorption plateau cannot be seen in the experiment, we can find an upper limit for the adsorption time τ_a^{max} that is given at the τ_a, at which the adsorption peak first disappears in the spectrum. The spectrum is then only affected though the impact of adsorption on the fluctuation noise. Accordingly, the average adsorption time in this experiment is smaller than 200 μs.

For this simulation, the ratio between free and adsorbed molecules is calculated from the average current and the standard deviation of the recorded trace [23]. Hereby, the number of free molecules n_{free} in between the electrodes is first computed from the average redox cycling current I_{rc} [19] and used to calculate the average number of adsorbed molecules n_{ads} as follows [23]

$$n_{ads} = \frac{< I_{rc} >^2}{I_{rc,std}^2} - n_{free}. \tag{7.6}$$

The ratio between adsorbed and desorbed molecules then equals the ratio

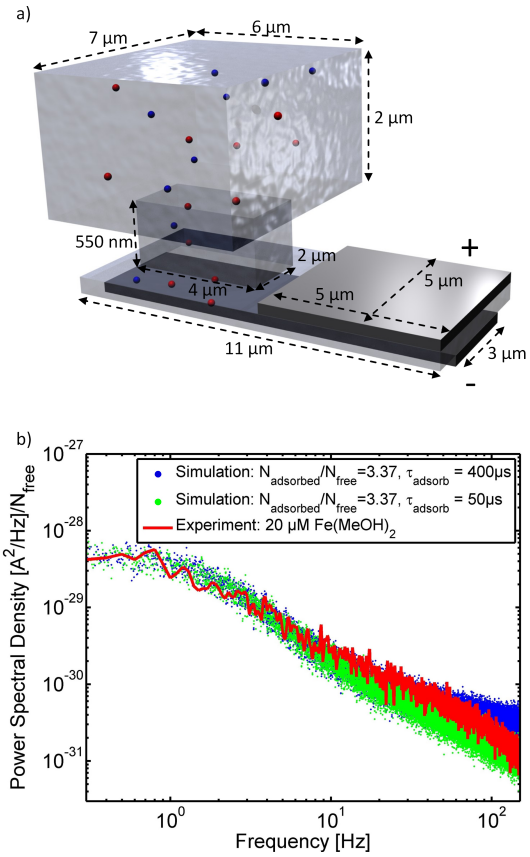

Figure 7.2: Comparison between simulation and experiment. a) Illustration of the simulated design. Attached to the access channel on the upper right, a cubic bulk reservoir is added to mimic a bulk reservoir. Dimensions are not to scale. b) Comparison between experimental data and simulations for different average adsorption times. The ratio between the average adsorbed and desorbed time is held constant to match the experimentally obtained value of 3.37. Detailed simulation parameters are given in Appendix B.

between the average adsorbed and desorbed times. By this means, one can calculate that the ratio τ_a/τ_d was 3.37 during the experiment.

7.5.3 Noise spectra of SECM experiments and IDAs

Having shown that the simulation can reproduce experimental measurements, the model is applied to other sensor designs. Since all effects are implemented on the molecular level and no further postprocessing of the simulated data is required, the simulation framework not limited to certain designs but may predict noise spectra of nano-scaled redox cycling sensors with almost arbitrary geometry. For this chapter, two common designs are chosen: an interdigitated array (IDA) and a scanning electrochemical microscope (SECM) tip above a conducting surface, see Figure 7.3a and b. Hereby, it is shown that both designs are particularly interesting for determination of average adhesion times in the millisecond range.

The noise spectra of a simulated IDA are given in Figure 7.3c, where dif-

ferently colored graphs indicate different average adsorption times. Surprisingly and in contrast to the above discussed nanofluidic sensors, the spectra of the IDA do not exhibit any impact in the high frequency regime above a transition frequency of 10 Hz. However, noise levels at low frequencies significantly depend on the simulated adsorption parameters. In case of no adsorption, one can find a flat plateau that spreads up to 40 Hz. But with increasing adsorption times, the noise below 10 Hz increases with adsorption. Accordingly, this section of the spectra can be used to determine the adsorption characteristics of molecules that typically adsorb longer than 10 ms. Any point in the spectra below 10 Hz hereby serves as a direct measure for the average residence time, while simulated curves allow a calibration of the sensor.

Additionally, the adsorption noise expected in a SECM experiment as shown in Figure 7.3d is simulated. The spectra show an impact in a wide adsorption regime of average residence times between 3 and 300 ms. In comparison to the spectra of an non adsorbing sensor, adsorption here induces an additional plateau between 1 and 300 Hz that shifts to higher frequencies and lower amplitudes with an increase in average residence time. Similar to the above specified spectroscopy method based on an IDA, one can utilize this plateau to identify the adsorption characteristics of the analyte under investigation. Thus, one can predict that adsorption phenomena on this time scale should become apparent in SECM experiments. Potentially, these simulations can be confirmed experimentally by the SECM community in future experiments.

7.6 Conclusions

A computational framework for the modeling of adsorption effects in nanoscaled electrochemical sensors is introduced. Adsorption is hereby implemented through a model based on fixed adsorption and desorption probabilities at electrodes while each analyte molecule is simulated individually. This approach elucidates the impact of specific molecular adsorption phenomena on the resulting sensor response. A distinct advantage over simplifying analytical concepts is further given by the applicability to almost arbitrary designs. In this chapter, it is first demonstrated that the simulations closely match experimentally obtained data sets and first conclusions regarding the analytes' adsorption properties are drawn. Having shown this, adsorption dependent noise spectra of IDEs and SECM tips are predicted. The presented results further suggest certain fea-

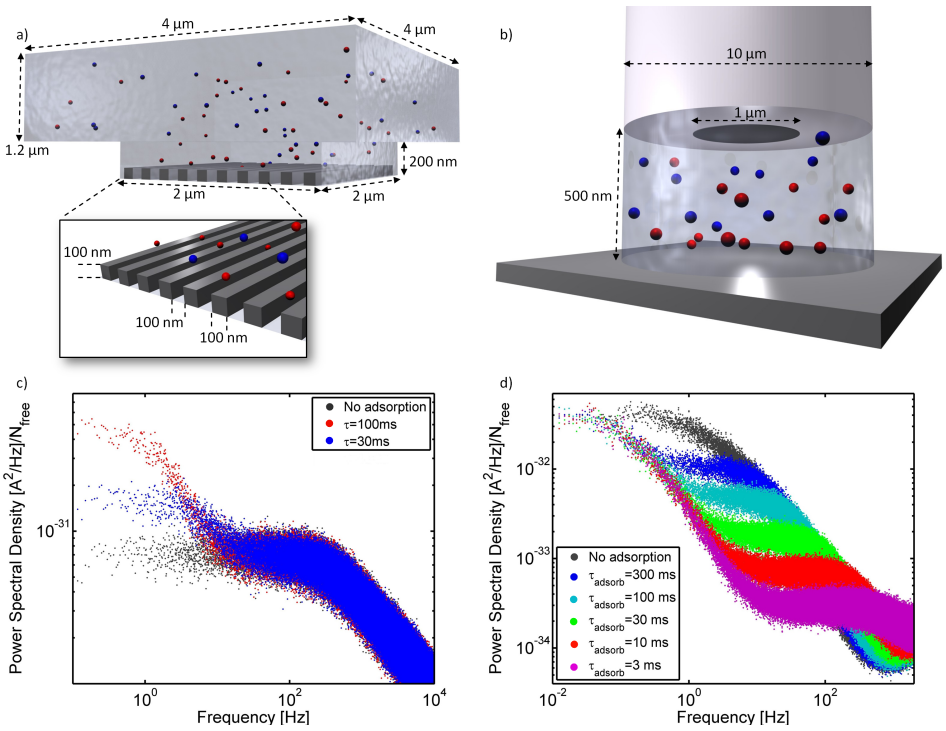

Figure 7.3: Simulations of other designs a) and b) Illustrations of the simulated designs of an IDA and an SECM tip. Dimensions are not to scale. c) Simulated noise spectrum of an IDA for different adsorption times. d) Simulated noise spectrum of a SECM probe for different adsorption times. All spectra are normalized to a single free molecule.

tures in the noise spectra to be used as key indicators in methods of adsorption spectroscopy.

Chapter 8

Conclusions and outlook

The presented work focuses on the utilization of nanoelectrochemical sensors for electrochemical imaging and spectroscopic applications. The results can hereby be classified into two groups: the design, fabrication, and characterization of new devices for on-chip sensing and the development of novel approaches to electrochemical noise spectroscopy, which have been found through methods of computational and theoretical electrochemistry.

Two devices are discussed in detail, a sensor for the spatiotemporal detection chemical gradients in microfluidic environments and a sensor for parallel chemical imaging at high spatial resolution. The first device, which has been fabricated and partly characterized in the framework of my diploma thesis, is optimized for fast response and simple readout. A detailed electrochemical characterization is shown and its response is probed in a microfluidic channel, which exposes the sensor array to rapidly changing analyte concentrations [57, 58]. Obtained results are compared to finite elements simulations and exhibit close agreement, thus, proving the device's fast sensing capabilities. On the basis of the presented design, novel devices for electrophysiological experiments have further been developed and characterized in other studies [126,127]. The second device is optimized for on-chip electrochemical imaging at a spatial resolution that is significantly improved in regard to the first device. By utilizing the amplification of Faradaic currents through redox cycling, the number of feed lines can be reduced drastically: the presented concept can address 256 individual sensors through just 32 feed lines instead of 512. This allows a considerably improved sensor density, since less room on the chip surface is occupied by feed lines. The device is characterized in detail and its capabilities are demonstrated by imaging the dissolution of a hexacyanoferrate crystal above the sensor array.

The second half of the thesis introduces a simulation framework for the modeling of nanoelectrochemical process on the molecular level, which has been used for various studies [81, 110, 124]. Two studies are presented: The first study investigates design-dependent noise characteristics of the Faradaic current by simulating the diffusive mass transport of analyte molecules towards the electrodes [124]. Hereby, the Brownian motion of all analyte molecules is simulated individually, thus, reproducing the current's noise characteristics. By this means, two sources of noise can be identified and characterized in dependency of the sensor geometry. The results suggest a novel sensing approach based on temporary changes in the sensor design, which for example can be caused by the occupation of certain areas through biological macromolecules.

The second study further advances the simulation concept by adding a model for reversible adsorption. By this means, experimental data can be closely reproduced and be compared to different settings of the adsorption parameters. This allows insight into molecular measures like the average adsorption time of an individual molecule. The simulation is further applied to common electrochemical setups like interdigitated arrays and scanning electrochemical microscope systems. Here, it was found that the noise characteristics of both setups strongly depend on the adsorption characteristics of the analyte molecules, which can be easily measured through the presented approach.

During the time of this thesis, two side projects have been initiated. These have not been finished yet, but first results promise new insights into fundamental nanoelectrochemistry and interesting future applications.

The first project focuses on the development of flexible nanocavity redox cycling sensors that I fabricated together with our collaborators in the cleanroom at the SIMIT in Shanghai. These sensors feature a design similar to the sensors that are presented in chapter three, but are build on a thin polyimide substrate and passivated by deposition of a polyimide cover layer. By this means, a foil is formed, which features a thickness of only few microns and comprises an array of nanofluidic redox cycling sensors inside. Once finished, these devices may be implantable and the cavity height can potentially be tuned by the application of an external force. This can possibly be done in a break junction device, see Figure 8, and may enable tunable signal amplification and exhibit new effects in noise spectroscopy.

The second project aims for the development a probe-based redox-cycling sensor for the detection of neurotransmitters in cell culture. In order to accomplish this, a nano electrode is fabricated in a patch-clamp pipette puller and subsequently covered by a thin platinum layer. In the next step, the device's tip is cut off in a focused ion beam machine, thus, separating the electrode and the platinum cover of the device. A scanning electrochemical micrograph of the device can be found in Figure 8.2. The device exhibits good performance in the detection of hexacyanoferrate. However, experiments in cell culture have not been performed yet, even though obtained results promise good applicability. This work was conducted in corporation with the former bachelor student Thomas Stefan Bronder.

In conclusion, this thesis demonstrates that nanofluidic redox cycling sensors are a versatile tool for a variety of different applications. Even though discussed

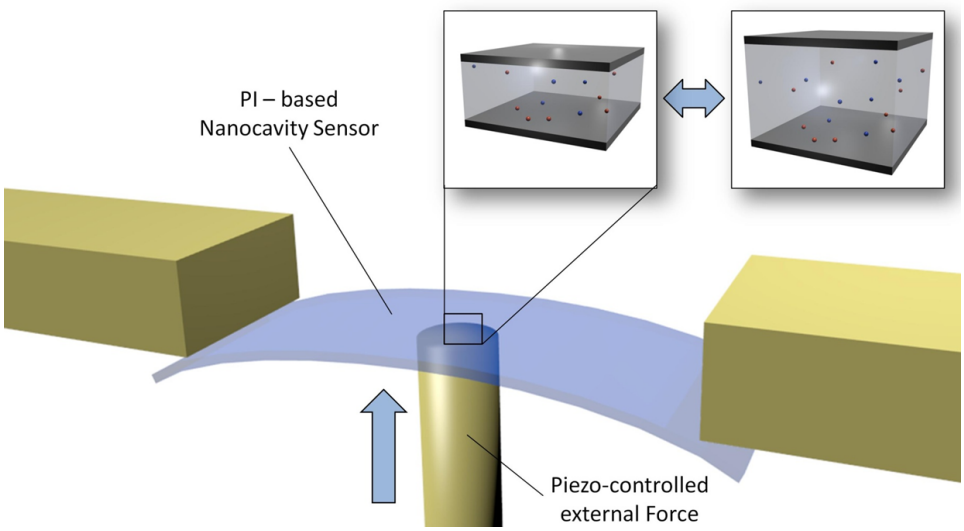

Figure 8.1: Illustration of a flexible nanocavity redox cycling sensor in a break junction machine. The height of the nanocavity is tuned by the application of an external force.

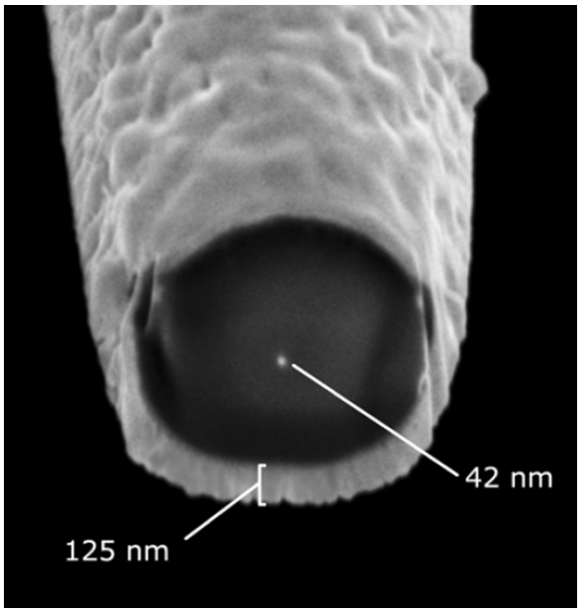

Figure 8.2: Scanning electrochemical micrograph of a probe-based redox cycling sensor. The image was adapted from the bachelor thesis of Thomas Stefan Bronder, "Fabrikation von Nanoelektroden für elektrochemische Detektion".

methods already range from the utilization in electrochemical imaging to different spectroscopic approaches, current research is still at the beginning and many applications remain to be pioneered. I strongly believe that there will be large number of novel approaches evolving during the upcoming years and decades, and look forward to observe nanoelectrochemical devices being used in future applications.

List of Figures

Bibliography

[1] Richard P Feynman. There's plenty of room at the bottom. *Engineering and Science*, 23(5):22–36, 1960.

[2] Torsten Fließbach. *Statistische Physik: Lehrbuch zur Theoretischen Physik IV (German Edition)*. Spektrum Akademischer Verlag, 1999.

[3] Christian Gerthsen and Dieter Meschede. *Gerthsen physik*. Springer DE, 2002.

[4] Allen J. Bard and Larry R. Faulkner. *Electrochemical Methods: Fundamentals and Applications*. Wiley, 2000.

[5] Wolfgang Schmickler and Elizabeth Santos. *Interfacial Electrochemistry*. Springer, 2010.

[6] R. S. Nicholson and Irving. Shain. Theory of stationary electrode polarography. single scan and cyclic methods applied to reversible, irreversible, and kinetic systems. *Analytical Chemistry*, 36(4):706–723, April 1964.

[7] R. S. Nicholson. Theory and application of cyclic voltammetry for measurement of electrode reaction kinetics. *Analytical Chemistry*, 37(11):1351–1355, October 1965.

[8] Jonathon O. Howell and R. Mark Wightman. Ultrafast voltammetry and voltammetry in highly resistive solutions with microvoltammetric electrodes. *Analytical Chemistry*, 56(3):524–529, March 1984.

[9] Christian Amatore, Emmanuel Maisonhaute, and Gerard Simonneau. Ultrafast cyclic voltammetry: performing in the few megavolts per second range without ohmic drop. *Electrochemistry Communications*, 2(2):81–84, February 2000.

[10] Richard B. Keithley, Pavel Takmakov, Elizabeth S. Bucher, Anna M. Belle, Catarina A. Owesson-White, Jinwoo Park, and R. Mark Wightman. Higher sensitivity dopamine measurements with faster-scan cyclic voltammetry. *Analytical Chemistry*, 83(9):3563–3571, May 2011.

[11] B. E. Kumara Swamy and B. Jill Venton. Carbon nanotube-modified microelectrodes for simultaneous detection of dopamine and serotonin in vivo. *The Analyst*, 132(9):876, 2007.

[12] RM Wightman, JA Jankowski, RT Kennedy, KT Kawagoe, TJ Schroeder, DJ Leszczyszyn, JA Near, EJ Diliberto, and OH Viveros. Temporally resolved catecholamine spikes correspond to single vesicle release from individual chromaffin cells. *Proceedings of the National Academy of Sciences*, 88(23):10754–10758, 1991.

[13] R. Mark Wightman. Probing cellular chemistry in biological systems with microelectrodes. *Science*, 311(5767):1570 –1574, March 2006.

[14] Jonathan M Bledsoe, Christopher J Kimble, Daniel P Covey, Charles D Blaha, Filippo Agnesi, Pedram Mohseni, Sidney Whitlock, David M Johnson, April Horne, Kevin E Bennet, et al. Development of the wireless instantaneous neurotransmitter concentration system for intraoperative neurochemical monitoring using fast-scan cyclic voltammetry: Technical note. *Journal of neurosurgery*, 111(4):712, 2009.

[15] J.C. Kraft, G.L. Osterhaus, A.N. Ortiz, P.A. Garris, and M.A. Johnson. In vivo dopamine release and uptake impairments in rats treated with 3-nitropropionic acid. *Neuroscience*, 161(3):940–949, July 2009.

[16] Matthew K. Zachek, Pavel Takmakov, Jinwoo Park, R. Mark Wightman, and Gregory S. McCarty. Simultaneous monitoring of dopamine concentration at spatially different brain locations in vivo. *Biosensors and Bioelectronics*, 25(5):1179–1185, January 2010.

[17] Liza Rassaei, Pradyumna S. Singh, and Serge G. Lemay. Lithography-based nanoelectrochemistry. *Analytical Chemistry*, 83(11):3974–3980, June 2011.

[18] Fu-Ren F. Fan and Allen J. Bard. Electrochemical detection of single molecules. *Science*, 267(5199):871 –874, February 1995.

[19] Bernhard Wolfrum, Marcel Zevenbergen, and Serge Lemay. Nanofluidic redox cycling amplification for the selective detection of catechol. *Analytical Chemistry*, 80(4):972–977, February 2008.

[20] Marcel A. G. Zevenbergen, Diego Krapf, Marc R. Zuiddam, and Serge G. Lemay. Mesoscopic concentration fluctuations in a fluidic nanocavity detected by redox cycling. *Nano Letters*, 7(2):384–388, February 2007.

[21] David Shoup and Attila Szabo. Chronoamperometric current at finite disk electrodes. *Journal of Electroanalytical Chemistry and Interfacial Electrochemistry*, 140(2):237–245, November 1982.

[22] Osamu Niwa, Masao Morita, and Hisao Tabei. Highly selective electrochemical detection of dopamine using interdigitated array electrodes modified with nafion/polyester lonomer layered film. *Electroanalysis*, 6(3):237–243, 1994.

[23] Pradyumna S. Singh, Hui-Shan M. Chan, Shuo Kang, and Serge G. Lemay. Stochastic amperometric fluctuations as a probe for dynamic adsorption in nanofluidic electrochemical systems. *J. Am. Chem. Soc.*, 133(45):18289–18295, 2011.

[24] Allen J. Bard, Joseph A. Crayston, Gregg P. Kittlesen, Theresa Varco Shea, and Mark S. Wrighton. Digital simulation of the measured electrochemical response of reversible redox couples at microelectrode arrays: consequences arising from closely spaced ultramicroelectrodes. *Analytical Chemistry*, 58(11):2321–2331, 1986.

[25] Osamu. Niwa, Masao. Morita, and Hisao. Tabei. Electrochemical behavior of reversible redox species at interdigitated array electrodes with different geometries: consideration of redox cycling and collection efficiency. *Analytical Chemistry*, 62(5):447–452, March 1990.

[26] D. M. Oglesby, S. H. Omang, and C. N. Reilley. Thin layer electrochemical studies using controlled potential or controlled current. *Analytical Chemistry*, 37(11):1312–1316, October 1965.

[27] Larry B. Anderson and Charles N. Reilley. Thin-layer electrochemistry: steady-state methods of studying rate processes. *Journal of Electroanalytical Chemistry*, 10(4):295–305, October 1965.

[28] Royce C. Engstrom, Michael Weber, Daniel J. Wunder, Robert Burgess, and Sharon Winquist. Measurements within the diffusion layer using a microelectrode probe. *Analytical Chemistry*, 58(4):844–848, April 1986.

[29] Hsue Yang. Liu, Fu Ren F. Fan, Charles W. Lin, and Allen J. Bard. Scanning electrochemical and tunneling ultramicroelectrode microscope for high-resolution examination of electrode surfaces in solution. *Journal of the American Chemical Society*, 108(13):3838–3839, June 1986.

[30] Royce C. Engstrom, Trevor Meaney, Ray Tople, and R. Mark Wightman. Spatiotemporal description of the diffusion layer with a microelectrode probe. *Analytical Chemistry*, 59(15):2005–2010, 1987.

[31] Allen J. Bard, Fu Ren F. Fan, Juhyoun Kwak, and Ovadia Lev. Scanning electrochemical microscopy. introduction and principles. *Analytical Chemistry*, 61(2):132–138, January 1989.

[32] Anna L. Barker, Marylou Gonsalves, Julie V. Macpherson, Christopher J. Slevin, and Patrick R. Unwin. Scanning electrochemical microscopy: beyond the solid/liquid interface. *Analytica Chimica Acta*, 385(1-3):223–240, April 1999.

[33] Michael V. Mirkin and Benjamin R. Horrocks. Electroanalytical measurements using the scanning electrochemical microscope. *Analytica Chimica Acta*, 406(2):119–146, February 2000.

[34] Douglas G. Sanderson and Larry B. Anderson. Filar electrodes: steady-state currents and spectroelectrochemistry at twin interdigitated electrodes. *Analytical Chemistry*, 57(12):2388–2393, October 1985.

[35] B. J. Feldman and Royce W. Murray. Measurement of electron diffusion coefficients through prussian blue electroactive films electrodeposited on interdigitated array platinum electrodes. *Analytical Chemistry*, 58(13):2844–2847, November 1986.

[36] Christopher E. Chidsey, B. J. Feldman, C. Lundgren, and Royce W. Murray. Micrometer-spaced platinum interdigitated array electrode: fabrication, theory, and initial use. *Analytical Chemistry*, 58(3):601–607, March 1986.

[37] Koichi Aoki, Masao Morita, Osamu Niwa, and Hisao Tabei. Quantitative analysis of reversible diffusion-controlled currents of redox soluble species at interdigitated array electrodes under steady-state conditions. *Journal of Electroanalytical Chemistry*, 256(2):269–282, December 1988.

[38] Kosei Ueno, Masayuki Hayashida, Jia-Yu Ye, and Hiroaki Misawa. Fabrication and electrochemical characterization of interdigitated nanoelectrode arrays. *Electrochemistry Communications*, 7(2):161–165, February 2005.

[39] Edgar Goluch, Bernhard Wolfrum, Pradyumna Singh, Marcel Zevenbergen, and Serge Lemay. Redox cycling in nanofluidic channels using interdigitated electrodes. *Analytical and Bioanalytical Chemistry*, 394(2):447–456, May 2009.

[40] N. Honda, K. Emi, T. Katagiri, T. Irita, S. Shoji, H. Sato, T. Homma, T. Osaka, M. Saito, J. Mizuno, and Y. Wada. 3-d comb electrodes for amperometric immuno sensors. In *TRANSDUCERS, Solid-State Sensors, Actuators and Microsystems, 12th International Conference on, 2003*, volume 2, pages 1132– 1135 vol.2. IEEE, June 2003.

[41] Sang Kyung Kim, Peter J. Hesketh, Changming Li, Jennifer H. Thomas, H. Brian Halsall, and William R. Heineman. Fabrication of comb interdigitated electrodes array (IDA) for a microbead-based electrochemical assay system. *Biosensors and Bioelectronics*, 20(4):887–894, November 2004.

[42] V. A. T. Dam, W. Olthuis, and A. van den Berg. Redox cycling with facing interdigitated array electrodes as a method for selective detection of redox species. *The Analyst*, 132(4):365–370, 2007.

[43] Gregory S. McCarty, Benjamin Moody, and Matthew K. Zachek. Enhancing electrochemical detection by scaling solid state nanogaps. *Journal of Electroanalytical Chemistry*, 643(1-2):9–14, May 2010.

[44] Xiaoshan Zhu and C. H Ahn. On-chip electrochemical analysis system using nanoelectrodes and bioelectronic CMOS chip. *IEEE Sensors Journal*, 6(5):1280–1286, October 2006.

[45] Feng-Lin Chan, Wen-Ying Chang, Li-Min Kuo, Chih-Heng Lin, Shi-Wei Wang, Yuh-Shyong Yang, and Michael SC Lu. An electrochemical dopamine sensor with a cmos detection circuit. *Journal of Micromechanics and Microengineering*, 18(7):075028, 2008.

[46] Chang-Wen Huang and Michael S.-C. Lu. Electrochemical detection of the neurotransmitter dopamine by nanoimprinted sub- microelectrodes and CMOS circuitry with near 100% collection efficiency. *Procedia Engineering*, 5:1196–1199, 2010.

[47] Charles S. Henry and Ingrid Fritsch. Microcavities containing individually addressable recessed microdisk and tubular nanoband electrodes. *Journal of The Electrochemical Society*, 146(9):3367–3373, 1999.

[48] Charles S. Henry and Ingrid Fritsch. Microfabricated recessed microdisk electrodes: Characterization in static and convective solutions. *Analytical Chemistry*, 71(3):550–556, February 1999.

[49] Walter R. Vandaveer, Donald J. Woodward, and Ingrid Fritsch. Redox cycling measurements of a model compound and dopamine in ultrasmall volumes with a self-contained microcavity device. *Electrochimica Acta*, 48(20-22):3341–3348, September 2003.

[50] Sebastian Neugebauer, Ulrich Müller, Theobald Lohmüller, Joachim P Spatz, Martin Stelzle, and Wolfgang Schuhmann. Characterization of nanopore electrode structures as basis for amplified electrochemical assays. *Electroanalysis*, 18(19-20):1929–1936, 2006.

[51] Sebastian Neugebauer, Leonard Stoica, Dmitrii Guschin, and Wolfgang Schuhmann. Redox-amplified biosensors based on selective modification of nanopore electrode structures with enzymes entrapped within electrodeposition paints. *Microchimica Acta*, 163(1-2):33–40, 2008.

[52] Theobald Lohmüller, Ulrich Müller, Stefanie Breisch, Wilfried Nisch, Ralf Rudorf, Wolfgang Schuhmann, Sebastian Neugebauer, Markus Kaczor, Stephan Linke, Sebastian Lechner, Joachim Spatz, and Martin Stelzle. Nano-porous electrode systems by colloidal lithography for sensitive electrochemical detection: fabrication technology and properties. *Journal of Micromechanics and Microengineering*, 18(11):115011, November 2008.

[53] Martin Hüske and Bernhard Wolfrum. Fabrication of a nanoporous dual-electrode system for electrochemical redox cycling. *physica status solidi (a)*, 208(6):1265–1269, 2011.

[54] Marcel A. G. Zevenbergen, Pradyumna S. Singh, Edgar D. Goluch, Bernhard L. Wolfrum, and Serge G. Lemay. Stochastic sensing of single molecules in a nanofluidic electrochemical device. *Nano Letters*, 11(7):2881–2886, July 2011.

[55] Marcel A. G. Zevenbergen, Pradyumna S. Singh, Edgar D. Goluch, Bernhard L. Wolfrum, and Serge G. Lemay. Electrochemical correlation spectroscopy in nanofluidic cavities. *Analytical Chemistry*, 81(19):8203–8212, October 2009.

[56] Marcel A. G. Zevenbergen, Bernhard L. Wolfrum, Edgar D. Goluch, Pradyumna S. Singh, and Serge G. Lemay. Fast electron-transfer kinetics probed in nanofluidic channels. *Journal of the American Chemical Society*, 131(32):11471–11477, 2009.

[57] Enno Kätelhön, Boris Hofmann, Serge G. Lemay, Marcel A. G. Zevenbergen, Andreas Offenhäusser, and Bernhard Wolfrum. Nanocavity redox cycling sensors for the detection of dopamine fluctuations in microfluidic gradients. *Analytical Chemistry*, 82(20):8502–8509, October 2010.

[58] E. Kätelhön, B. Hofmann, M. Banzet, A. Offenhäusser, and B. Wolfrum. Time-resolved mapping of neurotransmitter fluctuations by arrays of nanocavity redox-cycling sensors. *Procedia Engineering*, 5:956–958, 2010.

[59] Atsushi Aoki, Tomokazu Matsue, and Isamu Uchida. Electrochemical response at microarray electrodes in flowing streams and determination of catecholamines. *Analytical Chemistry*, 62(20):2206–2210, October 1990.

[60] Katsuyoshi Hayashi, Yuzuru Iwasaki, Tsutomu Horiuchi, Kenji Sunagawa, and Akiyuki Tate. Selective detection of a catecholamine against electroactive interferents using an interdigitated heteroarray electrode consisting of a metal oxide electrode and a metal band electrode. *Analytical Chemistry*, 77(16):5236–5242, 2005.

[61] Penny M. Lewis, Leah Bullard Sheridan, Robert E. Gawley, and Ingrid Fritsch. Signal amplification in a microchannel from redox cycling with varied electroactive configurations of an individually addressable microband electrode array. *Analytical Chemistry*, 82(5):1659–1668, March 2010.

[62] Zhenyu Lin, Yasufumi Takahashi, Yuusuke Kitagawa, Taizo Umemura, Hitoshi Shiku, and Tomokazu Matsue. An addressable microelectrode array for electrochemical detection. *Analytical Chemistry*, 80(17):6830–6833, 2008.

[63] R. Scott Martin, Andrew J. Gawron, Susan M. Lunte, and Charles S. Henry. Dual-electrode electrochemical detection for poly(dimethylsiloxane)-fabricated capillary electrophoresis microchips. *Analytical Chemistry*, 72(14):3196–3202, July 2000.

[64] Eric Nebling, Thomas Grunwald, Jörg Albers, Peter Schäfer, and Rainer Hintsche. Electrical detection of viral DNA using ultramicroelectrode arrays. *Analytical Chemistry*, 76(3):689–696, February 2004.

[65] Osamu Niwa, Ryoji Kurita, Zhiming Liu, Tsutomu Horiuchi, and Keiichi Torimitsu. Subnanoliter volume wall-jet cells combined with interdigitated microarray electrode and enzyme modified planar microelectrode. *Analytical Chemistry*, 72(5):949–955, March 2000.

[66] M. Odijk, W. Olthuis, T.V.A. Dam, and A. van den Berg. Simulation of redox-cycling phenomena at interdigitated array (IDA) electrodes: Amplification and selectivity. *Electroanalysis*, 20(5):463–468, 2008.

[67] Huseyin Bekir Yildiz, Jaime Castillo, Dmitrii A. Guschin, Levent Toppare, and Wolfgang Schuhmann. Phenol biosensor based on electrochemically controlled integration of tyrosinase in a redox polymer. *Microchimica Acta*, 159(1-2):27–34, May 2007.

[68] Jennifer H. Thomas, Sang Kyung Kim, Peter J. Hesketh, H. Brian Halsall, and William R. Heineman. Bead-based electrochemical immunoassay for bacteriophage MS2. *Analytical Chemistry*, 76(10):2700–2707, May 2004.

[69] Hargsoon Yoon, Phillip T Hankins, Vijay K Varadan, and Robert E Harbaugh. Dual electrode ensembles with core and shell nanoelectrodes for dopamine sensing applications. *Electroanalysis*, 20(10):1147–1150, 2008.

[70] Xiaohui Chen, Yuanfang Gao, Maruf Hossain, Shubhra Gangopadhyay, and Kevin D. Gillis. Controlled on-chip stimulation of quantal catecholamine release from chromaffin cells using photolysis of caged ca2+ on transparent indium-tin-oxide microchip electrodes. *Lab on a Chip*, 8(1):161, 2008.

[71] Yuzuru Iwasaki, Osamu Niwa, Masao Morita, Hisao Tabei, and Peter T. Kissinger. Selective electrochemical detection using a split disk array electrode in a thin-layer radial flow system. *Analytical Chemistry*, 68(21):3797–3800, January 1996.

[72] Donita L. Robinson, B. Jill Venton, Michael L.A.V. Heien, and R. Mark Wightman. Detecting subsecond dopamine release with fast-scan cyclic voltammetry in vivo. *Clin Chem*, 49(10):1763–1773, October 2003.

[73] Albert Schulte and Wolfgang Schuhmann. Single-cell microelectrochemistry. *Angewandte Chemie International Edition*, 46(46):8760–8777, 2007.

[74] P. Tyagi, D. Postetter, D. L. Saragnese, C. L. Randall, M. A. Mirski, and D. H. Gracias. Patternable nanowire sensors for electrochemical recording of dopamine. *Analytical Chemistry*, 81(24):9979–9984, December 2009.

[75] Fengjun Shang, Lin Zhou, Khaled A Mahmoud, Sabahudin Hrapovic, Yali Liu, Humphrey A Moynihan, Jeremy D Glennon, and John HT Luong. Selective nanomolar detection of dopamine using a boron-doped diamond electrode modified with an electropolymerized sulfobutylether-β-cyclodextrin-doped poly (n-acetyltyramine) and polypyrrole composite film. *Analytical chemistry*, 81(10):4089–4098, 2009.

[76] Christer Spégel, Arto Heiskanen, Jenny Acklid, Anders Wolff, Rafael Taboryski, Jenny Emnéus, and Tautgirdas Ruzgas. On-chip determination of dopamine exocytosis using mercaptopropionic acid modified microelectrodes. *Electroanalysis*, 19(2-3):263–271, 2007.

[77] Osamu Niwa. Electroanalysis with interdigitated array microelectrodes. *Electroanalysis*, 7(7):606–613, 1995.

[78] Anupama Aggarwal, Mengjia Hu, and Ingrid Fritsch. Detection of dopamine in the presence of excess ascorbic acid at physiological concentrations through redox cycling at an unmodified microelectrode array. *Analytical and bioanalytical chemistry*, pages 1–11, 2013.

[79] Serge G. Lemay, Shuo Kang, Klaus Mathwig, and Pradyumna S. Singh. Single-molecule electrochemistry: Present status and outlook. *Accounts of Chemical Research*, December 2012.

[80] Enno Kätelhön and Bernhard Wolfrum. On-chip redox cycling techniques for electrochemical detection. *Reviews in Analytical Chemistry*, 31(1):7–14, March 2012.

[81] Pradyumna S. Singh, Enno Kätelhön, Klaus Mathwig, Bernhard Wolfrum, and Serge G. Lemay. Stochasticity in single-molecule nanoelectrochemistry: Origins, consequences, and solutions. *ACS Nano*, 6(11):9662–9671, November 2012.

[82] Zhenyu Lin, Yasufumi Takahashi, Tatsuya Murata, Michiaki Takeda, Kosuke Ino, Hitoshi Shiku, and Tomokazu Matsue. Electrochemical gene-function analysis for single cells with addressable microelectrode/microwell arrays. *Angewandte Chemie International Edition*, 48(11):2044–2046, 2009.

[83] Michiaki Takeda, Hitoshi Shiku, Kosuke Ino, and Tomokazu Matsue. Electrochemical chip integrating scalable ring–ring electrode array to detect secreted alkaline phosphatase. *Analyst*, 136(23):4991–4996, 2011.

[84] Kosuke Ino, Wataru Saito, Masahiro Koide, Taizo Umemura, Hitoshi Shiku, and Tomokazu Matsue. Addressable electrode array device with IDA electrodes for high-throughput detection. *Lab on a Chip*, 11(3):385, 2011.

[85] Zhenyu Lin, Kosuke Ino, Hitoshi Shiku, Tomokazu Matsue, and Guonan Chen. Addressable electrochemiluminescence detection system based on redox-cycling of ru(bpy)32+. *Chemical Communications*, 46(2):243–245, December 2009.

[86] Zhenyu Lin, Kosuke Ino, Hitoshi Shiku, and Tomokazu Matsue. Electrochemical topography of a cell monolayer with an addressable microelectrode array. *Chemical Communications*, 46(4):559–561, January 2010.

[87] Xi Zhu, Kosuke Ino, Zhenyu Lin, Hitoshi Shiku, Guonan Chen, and Tomokazu Matsue. Amperometric detection of dna hybridization using

a multi-point, addressable electrochemical device. *Sensors and Actuators B: Chemical*, 160(1):923–928, 2011.

[88] Kosuke Ino, Taku Nishijo, Toshiharu Arai, Yusuke Kanno, Yasufumi Takahashi, Hitoshi Shiku, and Tomokazu Matsue. Local redox-cycling-based electrochemical chip device with deep microwells for evaluation of embryoid bodies. *Angewandte Chemie International Edition*, 51(27):6648–6652, 2012.

[89] Alexey Yakushenko, Enno Kätelhön, and Bernhard Wolfrum. Parallel on-chip analysis of single vesicle neurotransmitter release. *Analytical chemistry*, 2013.

[90] Khajak Berberian, Kassandra Kisler, Qinghua Fang, and Manfred Lindau. Improved surface-patterned platinum microelectrodes for the study of exocytotic events. *Analytical chemistry*, 81(21):8734–8740, 2009.

[91] Xin Liu, Syed Barizuddin, Wonchul Shin, Cherian J Mathai, Shubhra Gangopadhyay, and Kevin D Gillis. Microwell device for targeting single cells to electrochemical microelectrodes for high-throughput amperometric detection of quantal exocytosis. *Analytical chemistry*, 83(7):2445–2451, 2011.

[92] Yuqing Lin, Raphae l Trouillon, Maria I Svensson, Jacqueline D Keighron, Ann-Sofie Cans, and Andrew G Ewing. Carbon-ring microelectrode arrays for electrochemical imaging of single cell exocytosis: fabrication and characterization. *Analytical chemistry*, 84(6):2949–2954, 2012.

[93] Albert Schulte, Michaela Nebel, and Wolfgang Schuhmann. Single live cell topography and activity imaging with the shear-force-based constant-distance scanning electrochemical microscope. *Imaging and Spectroscopic Analysis of Living Cells: Optical and Spectroscopic Techniques*, 504:237, 2012.

[94] Brian Namghi Kim, Adam D Herbst, Sung June Kim, Bradley A Minch, and Manfred Lindau. Parallel recording of neurotransmitters release from chromaffin cells using a $10\times$ 10 cmos ic potentiostat array with on-chip working electrodes. *Biosensors and Bioelectronics*, 2012.

[95] A Paul Alivisatos, Anne M Andrews, Edward S Boyden, Miyoung Chun, George M Church, Karl Deisseroth, John P Donoghue, Scott E Fraser,

Jennifer Lippincott-Schwartz, Loren L Looger, et al. Nanotools for neuroscience and brain activity mapping. *ACS nano*, 2013.

[96] Yasufumi Takahashi, Andrew I Shevchuk, Pavel Novak, Babak Babakinejad, Julie Macpherson, Patrick R Unwin, Hitoshi Shiku, Julia Gorelik, David Klenerman, Yuri E Korchev, et al. Topographical and electrochemical nanoscale imaging of living cells using voltage-switching mode scanning electrochemical microscopy. *Proceedings of the National Academy of Sciences*, 109(29):11540–11545, 2012.

[97] Christopher Batchelor-McAuley, Edmund J. F. Dickinson, Neil V. Rees, Kathryn E. Toghill, and Richard G. Compton. New electrochemical methods. *Anal. Chem.*, 84(2):669–684, 2011.

[98] Kosuke Ino, Yusuke Kanno, Taku Nishijo, Takehito Goto, Toshiharu Arai, Yasufumi Takahashi, Hitoshi Shiku, and Tomokazu Matsue. Electrochemical detection for dynamic analyses of a redox component in droplets using a local redox cycling-based electrochemical (LRC-EC) chip device. *Chemical communications (Cambridge, England)*, 48(68):8505–8507, September 2012. PMID: 22810361.

[99] M. G. Straver, M. Odijk, W. Olthuis, and A. van den Berg. A simple method to fabricate electrochemical sensor systems with predictable high-redox cycling amplification. *Lab on a Chip*, 12(8):1548–1553, April 2012.

[100] R.J. White and H.S. White. A random walk through electron-transfer kinetics. *Analytical chemistry*, 77(11):214–220, 2005.

[101] Gabor Nagy, Yoshiharu Sugimoto, and Guy Denuault. Three-dimensional random walk simulations of diffusion controlled electrode processes: (i) a hemisphere, disc and growing hemisphere. *Journal of Electroanalytical Chemistry*, 433(1-2):167–173, August 1997.

[102] Gabor Nagy and Guy Denuault. Three-dimensional random walk simulation of diffusion controlled electrode processes: (II) arrays of growing hemispheres. *Journal of Electroanalytical Chemistry*, 433(1-2):175–180, August 1997.

[103] Shuai Liang, Qijing Guo, and Xiandui Dong. The time delay in electrochemical measurements of a finite-volume system. *Journal of Electroanalytical Chemistry*, 633(1):235–239, August 2009.

[104] Ian J. Cutress, Edmund J.F. Dickinson, and Richard G. Compton. Electrochemical random-walk theory: Probing voltammetry with small numbers of molecules: Stochastic versus statistical (fickian) diffusion. *Journal of Electroanalytical Chemistry*, 655(1):1–8, May 2011.

[105] Shuai Liang and Xiandui Dong. Theoretical investigation of electrochemical signal from nanoscale systems. *Electroanalysis*, 23(6):1447–1453, June 2011.

[106] Stuart Licht, Vince Cammarata, and Mark S Wrighton. Time and spatial dependence of the concentration of less than 105 microelectrode-generated molecules. *Science*, 243(4895):1176–1178, 1989.

[107] Stuart. Licht, Vince. Cammarata, and Mark S. Wrighton. Direct measurements of the physical diffusion of redox active species: microelectrochemical experiments and their simulation. *The Journal of Physical Chemistry*, 94(15):6133–6140, July 1990.

[108] John E. Baur and Perry N. Motsegood. Diffusional interactions at dual disk microelectrodes: comparison of experiment with three-dimensional random walk simulations. *Journal of Electroanalytical Chemistry*, 572(1):29–40, October 2004.

[109] Ryan J. White and Henry S. White. Electrochemistry in nanometer-wide electrochemical cells. *Langmuir*, 24(6):2850–2855, March 2008.

[110] Enno Kätelhön and Bernhard Wolfrum. Simulation-based investigations on noise characteristics of redox-cycling sensors. *physica status solidi (a)*, 209(5):881–884, 2012.

[111] Makoto Matsumoto and Takuji Nishimura. Mersenne twister: a 623-dimensionally equidistributed uniform pseudo-random number generator. *ACM Trans. Model. Comput. Simul.*, 8(1):3–30, January 1998.

[112] Gang Liu, Chunfeng Sun, Di Li, Shiping Song, Bingwei Mao, Chunhai Fan, and Zhongqun Tian. Gating of redox currents at gold nanoelectrodes via DNA hybridization. *Advanced Materials*, 22(19):2148–2150, 2010.

[113] John J Watkins, Jinyuan Chen, Henry S White, Héctor D Abruña, Emmanuel Maisonhaute, and Christian Amatore. Zeptomole voltammetric

detection and electron-transfer rate measurements using platinum electrodes of nanometer dimensions. *Analytical chemistry*, 75(16):3962–3971, 2003.

[114] Paul EM Phillips, Garret D Stuber, Michael LAV Heien, R Mark Wightman, and Regina M Carelli. Subsecond dopamine release promotes cocaine seeking. *Nature*, 422(6932):614–618, 2003.

[115] Juhyoun Kwak and Allen J Bard. Scanning electrochemical microscopy. theory of the feedback mode. *Analytical Chemistry*, 61(11):1221–1227, 1989.

[116] Yuanhua Shao, Michael V Mirkin, Galina Fish, Sofia Kokotov, Daniel Palanker, and Aaron Lewis. Nanometer-sized electrochemical sensors. *Analytical Chemistry*, 69(8):1627–1634, 1997.

[117] Gunther Wittstock and Wolfgang Schuhmann. Formation and imaging of microscopic enzymatically active spots on an alkanethiolate-covered gold electrode by scanning electrochemical microscopy. *Analytical Chemistry*, 69(24):5059–5066, 1997.

[118] Julie V Macpherson and Patrick R Unwin. Combined scanning electrochemical-atomic force microscopy. *Analytical chemistry*, 72(2):276–285, 2000.

[119] José L Fernández, Darren A Walsh, and Allen J Bard. Thermodynamic guidelines for the design of bimetallic catalysts for oxygen electroreduction and rapid screening by scanning electrochemical microscopy. m-co (m: Pd, ag, au). *Journal of the American Chemical Society*, 127(1):357–365, 2005.

[120] Masao Morita, Osamu Niwa, and Tsutomu Horiuchi. Interdigitated array microelectrodes as electrochemical sensors. *Electrochimica acta*, 42(20):3177–3183, 1997.

[121] Osamu Niwa, Yan Xu, H Brian Halsall, and William R Heineman. Small-volume voltammetric detection of 4-aminophenol with interdigitated array electrodes and its application to electrochemical enzyme immunoassay. *Analytical chemistry*, 65(11):1559–1563, 1993.

[122] Sean P Branagan, Nicholas M Contento, and Paul W Bohn. Enhanced mass transport of electroactive species to annular nanoband electrodes embedded in nanocapillary array membranes. *Journal of the American Chemical Society*, 134(20):8617–8624, 2012.

[123] Fu-Ren F Fan and Allen J Bard. An electrochemical coulomb staircase: Detection of single electron-transfer events at nanometer electrodes. *Science*, 277(5333):1791–1793, 1997.

[124] Enno Kätelhön, Kay J Krause, Pradyumna S Singh, Serge G Lemay, and Bernhard Wolfrum. Noise characteristics of nano-scaled redox-cycling sensors: Investigations based on random walks. *Journal of the American Chemical Society*, 2013.

[125] Klaus Mathwig and Serge G Lemay. Pushing the limits of electrical detection of ultralow flows in nanofluidic channels. *Micromachines*, 4(2):138–148, 2013.

[126] Boris Hofmann, Enno Kätelhön, Manuel Schottdorf, Andreas Offenhäusser, and Bernhard Wolfrum. Nanocavity electrode array for recording from electrogenic cells. *Lab on a Chip*, 2011.

[127] Manuel Schottdorf, Boris Hofmann, Enno Kätelhön, Andreas Offenhäusser, and Bernhard Wolfrum. Frequency-dependent signal transfer at the interface between electrogenic cells and nanocavity electrodes. *Physical Review E*, 85(3):031917, 2012.

Appendices

Appendix A: Data processing for Figure 6.2b

After conditioning the sensor for 200 s, the experimentally obtained current trace still exhibits a slow drift that we attribute to the evaporation of solvent from the bulk reservoir. This drift was later removed by subtracting a linear fit from the recorded trace, see Figure 8.3.

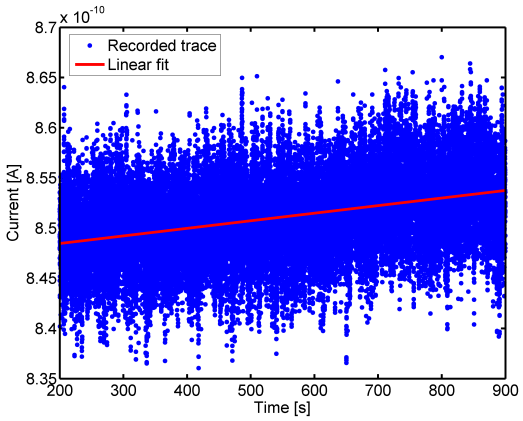

Figure 8.3: Processing of the experimentally obtained data. A linear fit (red) was subtracted from the recorded trace (blue).

Appendix B: Simulation parameters in chapter 7

Figure 7.1b

Number of active molecules = 250
Spatial stepwidth = 5 nm
Diffusion constant = 10^{-9}
Temporal stepwidth = 12.5 ns
Number of iterations = 16*10^{8}
Simulated time interval = 20 s
Sum over iterations = 800
Sampling frequency = 100 kHz
Ratio between the average adsorbed and desorbed time $\eta = 20$

Figure 7.2b

Number of active molecules = 200
Spatial stepwidth = 5 nm
Diffusion constant = 6.7*10^{-10}
Temporal stepwidth = 18.66 ns
Number of iterations = 107.2*10^{8}
Simulated time interval = 200 s
Sum over iterations = 5360
Sampling frequency = 10 kHz
Ratio between the average adsorbed and desorbed time $\eta = 3.37$

Figure 7.3c

Number of active molecules = 500
Spatial stepwidth = 10 nm
Diffusion constant = 10^{-9}
Temporal stepwidth = 50 ns
Number of iterations = 12*10^{8}
Simulated time interval = 60 s
Sum over iterations = 600
Sampling frequency = 33.3 kHz

Ratio between the average adsorbed and desorbed time $\eta = 20$

Figure 7.3d

Number of active molecules = 500
Spatial stepwidth = 50 nm
Diffusion constant = 10^{-9}
Temporal stepwidth = 1.25 μs
Number of iterations = 3.2*10^{8}
Simulated time interval = 400 s
Sum over iterations = 160
Sampling frequency = 5 kHz
Ratio between the average adsorbed and desorbed time $\eta = 20$

Author's list of publications

Journal publications

1. Kätelhön, E. ; Krause, K. J. ; Singh, P. S. ; Lemay, S. G. ; Wolfrum, B. "Noise characteristics of nano-scaled redox-cycling sensors: Investigations based on random walks." **Journal of the American chemical society** 135, 8874 - 8881 (2013).

2. Yakushenko, A. ; Kätelhön, E. ; Wolfrum B. "Parallel on-chip analysis of single vesicle neurotransmitter release." **Analytical chemistry** 85, 5483 - 5490 (2013).

3. Singh, P. S. ; Kätelhön, E. ; Mathwig, K. ; Wolfrum, B. ; Lemay, S. G. "Stochasticity in single-molecule nanoelectrochemistry: origins, consequences, and solutions." **ACS Nano** 6, 9662 - 9671 (2012).

4. Kätelhön, E. ; Wolfrum, B. "Simulation-based investigations on noise characteristics of redox-cycling sensors." **Physica status solidi A** 209, 881 - 884 (2012).

5. Schottdorf, M. ; Hofmann, B. ; Kätelhön, E. ; Offenhäusser, A. ; Wolfrum, B. "Frequency-dependent signal transfer at the interface between electrogenic cells and nanocavity electrodes." **Physical review E** 85, 031917 (2012).

6. Kätelhön, E. ; Wolfrum, B. "On-chip redox cycling techniques for electrochemical detection." **Reviews in analytical chemistry** 31, 7 - 14 (2012).

7. Hofmann, B. ; Kätelhön, E. ; Schottdorf, M. ; Offenhäusser, A. ; Wolfrum, B. "Nanocavity electrode array for recording from electrogenic cells." **Lab on a chip** 11, 1054-1058 (2011).

8. Kätelhön, E. ; Hofmann, B. ; Banzet, M. ; Offenhäusser, A. ; Wolfrum, B. "Time-resolved mapping of neurotransmitter fluctuations by arrays of nanocavity redox-cycling sensors." **Procedia engineering** 5, 956 - 958 (2010).

9. Kätelhön, E. ; Hofmann, B. ; Lemay, S. G. ; Zevenbergen, M. A. G. ; Offenhäusser, A. ; Wolfrum, B. "Nanocavity redox cycling sensors for the detection of dopamine fluctuations in microfluidic gradients." **Analytical chemistry** 82, 8502 - 8509 (2010).

Unpublished work / in preparation

1. Kätelhön, E. ; Mayer, D. ; Banzet, M. ; Offenhäusser, A. ; Wolfrum, B. "Nanocavity cross-bar arrays for high-density electrochemical imaging".

2. Kätelhön, E. ; Krause, K. J. ; Mathwig, K. ; Lemay, S. G. ; Wolfrum, B. "Noise phenomena caused by reversible adsorption in nano-scaled electrochemical devices".

Patent applications

1. Kätelhön, E. ; Banzet, M. ; Hofmann, B. ; ; Mayer, D. ; Offenhäusser, A. ; Wolfrum, B. "Method for producing a device for detecting an analyte and device and use thereof." WO 2012107014 A1.

2. Wolfrum, B. ; Offenhäusser, A. ; Hofmann, B. ; Kätelhön, E. ; Banzet, M. "Device for deriving electrophysiological signals from cells." EP2550526 A2.

Acknowledgements

I would like to thank everybody, who supported me during the time of my PhD-thesis. Especially, I would like to thank:

- **Bernhard Wolfrum** für die exzellente Betreuung und die tolle Unterstützung während meiner gesamten Zeit in Jülich. Ich habe unglaublich viel von Dir gelernt und die Arbeit in Deiner Gruppe hat mir viel Spaß gemacht. Ganz besonders bedanke ich mich für Deinen Enthusiasmus, Dein Vertrauen und die Freiheit in der Forschung auch nach links und rechts schauen zu dürfen. Ich hoffe, daß wir auch weiter zusammenarbeiten können, wenn ich in Oxford bin.

- **Jörg Fitter** für die Zweitkorrektur meiner Arbeit. Ich bedanke mich ganz herzlich für Ihr Interesse, Ihre Zeit und Ihre Vorschläge und Korrekturen.

- **Andreas Offenhäusser** für die Labore und die weitere Infrastruktur. Ich habe immer sehr gerne in Ihrem Institut gearbeitet und hoffe auch in Zukunft weiter eng mit Ihnen in Kontakt bleiben zu können.

- **Kay Johannes Krause** und **Thomas Bronder** für Eure tollen Master- und Bachelorarbeiten. Die Zusammenarbeit mit Euch hat mir viel Spaß gemacht und ich bedanke mich ganz herzlich für Eure Unterstützung.

- **Marko Banzet** für die hervorragende Zusammenarbeit im Reinraum. Vielen Dank für die gute Einführung in die Reinraumarbeit und die vielen Proben, die Du hergestellt hast. Ich habe viel von Dir gelernt.

- **Serge Lemay**, **Pradyumna Singh**, and **Klaus Mathwig** for our excellent and fruitful cooperation. It was great to work with you and I hope that we can continue our collaboration in the future.

- **Jin Qinghui** for his great hospitality and the invitation to work in his laboratories at SIMIT.

- **Zhang Feng** for the excellent support in the labs at SIMIT and for introducing me to daily life in Shanghai.

- **Alexey Yakuschenko**, **Boris Hofmann** und **Martin Hüske** für die tolle Zusammenarbeit im Labor und viele wissenschaftliche Diskussionen, die mir immer sehr geholfen haben.

- **Li Pinggui**, **Cony Herreras**, and **Nabeel Aslam** for being great office mates. It was always a lot of fun to share the office with you.

- **Rita Fricke** und **Tina Breuer** für die tolle Unterstützung in den Biolaboren.

- **Dieter Strobl** und den Kollegen der mechanischen Werkstatt für die gute Zusammenarbeit beim Aufbau meines Messtandes.

- **Norbert Wolters**, **Dieter Lomparski** und den Kollegen der elektronischen Werkstatt für die Entwicklung toller Messgeräte.

- **Susanne Bippus** für die gute Unterstützung bei allen administrativen Aufgaben.

- Nicht zuletzt bedanke ich mich bei meinen Eltern **Karin** und **Jan Kätelhön** und meinem Bruder **Arne Kätelhön**. Von Herzen vielen Dank für all Eure Hilfe und Unterstützung.